Dissertation
submitted to the
Combined Faculties for the Natural Sciences and for Mathematics
of the Ruperto-Carola University of Heidelberg, Germany
for the degree of
Doctor of Natural Sciences

Put forward by
Diplom-Physiker Martin Fast
Born in Bergisch Gladbach, Germany
Oral examination: 10/7/2013

New Methods for Motion Management During Radiation Therapy

Referees: **Prof. Dr. Uwe Oelfke**
Prof. Dr. Wolfgang Schlegel

Abstract

In this thesis, a number of new image-based techniques for the management of *intra-fractional* motion during radiation therapy are presented. Intra-fractional motion describes all kinds of anatomy changes - most prominently respiration - that occur during a single treatment session. Spatially confining the radiation dose to the tumour tissue and thus sparing surrounding healthy tissue is assumed to be crucial for a successful treatment with limited side effects. Unfortunately, the delivery of dose distributions that are sharply confined to the tumour is greatly complicated by patient motion. If not accounted for, this motion will lead to a smearing out of the original dose distribution and will facilitate the redistribution of dose from tumour to healthy tissue. Possible technical solutions for this issue include the interruption of the radiation delivery if the tumour leaves a predefined spatial 'window', and the reshaping of the treatment field 'on-the-fly' to follow the tumour. Regardless of which delivery techniques is selected, the patient motion needs to be reliably detected in real-time to allow for an adaptation of the treatment delivery. First, we present experimental results for a novel x-ray imaging system that is attached to the treatment delivery device and enables us to continuously monitor the tumour motion during treatment delivery with sub-mm accuracy, a latency better than 90 ms, and a 7 Hz update rate. Second, we present a Monte Carlo simulation for an improved amorphous-silicon flat-panel detector that reduced treatment beam filtration by 60% and long-range MV-scatter by 80%. We conclude this thesis by presenting results of an experimental demonstration of a novel dose-saving actively-triggered 4d cone-beam computed tomography device.

Zusammenfassung

In dieser Arbeit werden eine Reihe von neuartigen bildgestützten Techniken zur Handhabung von *intrafraktioneller* Bewegung während der Strahlentherapie vorgestellt. Unter intrafraktioneller Bewegung versteht man alle Änderungen der Anatomie, die während einer einzelnen Strahlentherapie-Sitzung auftreten. Die zyklische Atembewegung ist das wohl prominenteste Beispiel. Es wird davon ausgegangen, dass der langfristige Erfolg einer Strahlentherapie-Behandlung davon abhängt, mit welcher räumlichen Genauigkeit die Strahlendosis auf den Tumor beschränkt bleibt. Durch Veränderungen der Position des Tumors relativ zum Strahlenfeld verschmiert sich die Dosisverteilung, und die Dosis wird effektiv vom Tumor ins gesunde benachbarte Gewebe umverteilt. Es gibt mehrere Bestrahlungstechniken, die diesem Prozess entgegenwirken, u.a. kann die Dosisapplikation unterbrochen werden, falls der Tumor einen vordefinierten Bereich verlässt oder das Bestrahlungsfeld kann dynamisch angepasst werden und somit die Tumorbewegung nachverfolgt werden. Unabhängig davon, welche Bestrahlungstechnik eingesetzt wird, ist es von entscheidender Bedeutung, die Tumorbewegung zuverlässig und in Echtzeit zu detektieren. Zunächst präsentieren wir daher ein Röntgen-basiertes Bildgebungssystem, das in dem Therapie-Gerät integriert ist und die kontinuierliche Überwachung der Tumorposition, mit sub-mm Genauigkeit und einer Latenzzeit unter 90 ms (Bildfrequenz: 7 Hz), während der Strahlentherapie erlaubt. Dann stellen wir die Ergebnisse einer Monte-Carlo-Simulationsstudie vor, in der ein verbesserter Röntgendetektor für die intrafraktionelle Bildgebung untersucht wird. Abschließend wird ein neuartiges aktiv-gesteuertes Verfahren für die 4D-Kegelstrahl-Computertomographie vorgestellt mit dem sich die Bildgebungsdosis deutlich reduzieren lässt.

Contents

Chapter 1

Introduction

The aim of radiation therapy - also referred to as 'radiotherapy' - is to cure cancer by irradiating mostly solid tumours with ionizing radiation. Traditionally, x-ray beams with maximum energies between roughly 6 and 25 MeV are used to irradiate the tumour. For tumour sites close to the patient's surface, x-ray beams of lower energies and also electron beams are used for radiation treatment. In recent years, treatments with protons or heavy ions have become more widespread, though they still present a very small minority of overall treatments due to their relative technical complexity and higher treatment costs (Peeters et al. 2010). Two main mechanisms are responsible for damaging cells (tumour or not): (i) direct transfer of energy to atoms that are part of the DNA, and (ii) the ionization of water, which creates free radicals that can damage the DNA. Fortunately, tumour cells are less efficient at repairing radiation-induced DNA damage than healthy cells. By spreading the total radiation dose over multiple treatment sessions, a strategy known as 'fractionation', it is possible to use this differential healing effect and keep the damage to normal tissue to an acceptable level.

Regardless of the actual treatment modality, the success of treatment is widely believed to depend on the coverage of the tumour with radiation dose, i.e. on the amount of energy absorbed per unit mass, as well as on the sparing of healthy surrounding tissue from radiation dose. Finding the optimal balance between *tumour control probability* (TCP) and *normal tissue complication probability* (NTCP) is not a trivial task since the tumour is usually surrounded by healthy tissue (Verellen et al. 2007). It is intuitively clear that the two extremal solutions - a very high dose to increase TCP or a very low dose to decrease NTCP - are not optimal. To make matters yet more challenging, certain organs like the heart or the spinal cord are very sensitive to radiation and must be spared from radiation dose as much as possible.

Modern treatment schemes, such as *conformal radiation therapy* and *intensity-modulated radiation therapy* (IMRT) seek to minimise the NTCP by shaping the radiation field as closely as possible around the tumour. Frequently, this leads to steep dose gradients between the tumour and neighbouring organs-at-risk. The success of treatment outcome then becomes highly susceptible to motion-induced changes in the anatomy. When disregarding motion, radiation dose is blurred over a larger volume, resulting in decreased tumour coverage and increased toxicity for the normal tissue.

It is common practise to differentiate patient motion occurring between radiation therapy treatment sessions (*inter-fractional* motion) and during a single treatment session (*intra-fractional* motion). The former usually covers changes in the patient's anatomy occurring on the hours-to-days time scale. These changes might be induced by factors relating to the tumour (for example shrinkage or growth) or to the general anatomy (for example the bladder filling, weight changes and the like). Assuming only relative shifts within the anatomy occurred, repositioning the patient on the treatment couch based on 2d or 3d images of the internal anatomy acquired just

prior to treatment is the preferred course of action. Larger or non-linear changes in the anatomy, however, might require adapting the original treatment plan, a strategy named *adaptive radiation therapy* (Yan et al. 1997). Intra-fractional motion, which is addressed in this thesis, covers motion events that occur during a single therapy session on the seconds-to-minutes time scale. An even stricter definition of intra-fractional motion only includes motion events happening while the treatment beam is on. The most prominent example of this type of motion is respiration which affects the position of most lung tumours but also liver tumours. Other examples are the heart beat and random motion related to gas pockets in the abdomen. Keall et al. (2006) report in a meta-study that the average lung tumour displacement in superior-inferior direction (i.e. the main motion axes) ranges from 3 to 19 mm. The authors describe even larger respiration-induced displacements for the pancreas, liver, kidney, and diaphragm. For prostate cancer cases, translations (Kotte et al. 2007), rotations, and even deformations (van der Wielen et al. 2008) of the organ are frequently observed. Deutschmann et al. (2012) observed intra-fractional 3d translations of 3.0±3.7 mm (maximum: 10.2 mm) and left-right rotations of 2.5°±2.3° (maximum: 26.9°).

The simplest and most utilized strategy for ensuring local tumour control under motion is to increase the size of the radiation field, i.e. add a motion-related margin to the original treatment field. This strategy ensures that the prescribed tumour dose is administrated (if the tumour motion is as expected), but it comes at the cost of an increase in NTCP. Safety margins are generally an important concept in radiation therapy (van Herk 2004). They account for a wide range of uncertainties that arise in any realistic treatment scenario: this includes among others uncertainty in the definition (ICRU 1993) of the *gross tumour volume* (GTV), the often unknown microscopic sprawl of the tumour which together with the GTV defines the *clinical target volume* (CTV), and patient set-up errors. The famous 'margin recipe' by van Herk et al. (2000) ensures that the margin between CTV and *planning target volume* (PTV) is large enough to guarantee that 90% of the members of a typical patient collective receive at least 95% of the prescribed CTV dose. van Herk et al. (2000) assume that systematic 'treatment preparation' (e.g. delineation) and random 'treatment execution' (e.g. organ motion) errors can be estimated independently. They argue that the systematic errors "lead to a displacement of the dose distribution with respect to the CTV", and that the random errors "lead to a blurring of the dose distribution" (van Herk et al. 2000). The authors further assume that random errors can average out over multiple treatment fraction, whereas systematic errors cannot. This leads them to weigh the (combined) systematic error more strongly then the (combined) random error, when linearly combining the two for their margin recipe.

Outline

Instead of widening the treatment margins to account for intra-fractional organ motion, a better strategy for motion compensation, especially for lung cancer treatments, would be the real-time detection of intra-fractional motion and subsequent adaptation of the treatment procedure on-the-fly. This would allow one to shrink motion-related margins without compromising the TCP. The changes in treatment volume can be quite dramatic even for small margin changes: assuming a spherical lung tumour of 10 mm radius (PTV, isotropic margins), a 1 mm margin reduction corresponds to a 27% volume reduction. Additionally, the assumption that random organ motion averages out over multiple treatment sessions, does not hold true for the increasingly popular *hypo-fractionated* treatments (Brock et al. 2008), i.e. treatments with 3-5 treatment fractions instead of 30-40 for conventional *hyper-fractionated* treatments.

In chapter 2, the different technologies for motion detection currently available and the entire motion management chain are described. A vision of a future fully adaptive radiation treatment regime will be outlined. In this thesis, the focus is on detecting motion using x-ray imaging

modalities integrated with the linear accelerator (linac) used for treatment. Chapter 3 describes target tracking experiments using a linac-mounted intra-fractional x-ray imaging system based on the unique 'in-line' imaging geometry. Next, a Monte Carlo simulation study is described which was conducted to find an x-ray detector better suited for the 'in-line' imaging geometry (chapter 4). Lastly, a new strategy for acquiring 4d cone-beam CT images is presented in chapter 5. 4d CBCT images are frequently used to characterize the intra-fractional motion of lung tumours. A summary of the findings as well as an outlook into possible future research concludes this thesis (chapter 6).

Publications

Chapters 3 and 4 of this thesis have been published - in accordance with the regulations of the Combined Faculties for the Natural Sciences and for Mathematics at the University of Heidelberg - in the following peer-reviewed journal articles:

Fast, M., Krauss, A., Oelfke, U. & Nill, S. (2012). Position detection accuracy of a novel linac-mounted intrafractional x-ray imaging system, *Med. Phys.* **39**: 109–118.

Fast, M., Teymurazyan, A., Pang, G., Oelfke, U. & Rowlands, J. (2013). Finding an improved amorphous-silicon x-ray flat-panel detector configuration for the in-line geometry, *Phys. Med. Biol.* **58**: 2305–2324.

Another publication is currently being prepared based on chapter 5:

Fast, M., Wisotzky, E., Oelfke, U. & Nill, S. (2013). Actively triggered 4d cone-beam CT acquisition, *Med. Phys.* **Submitted**.

A number of peer-reviewed conference submissions were also instrumental in writing this thesis:

Fast, M., Oelfke, U. & Nill, S. (2011). A novel approach to linac-mounted intra-fractional x-ray imaging for motion management, *Radiother. Oncol.* **99**: S93–S94.

Fast, M., Krauss, A., Nill, S. & Oelfke, U. (2011). Tu-c-214-08: Position detection accuracy of a novel linac-mounted intra-fractional x-ray imaging system, *Med. Phys.* **38**: 3757.

Fast, M., Wisotzky, E., Oelfke, U. & Nill, S. (2012). Simultaneous use of an electromagnetic tracking device and a conventional flat-panel x-ray imager, *Radiother. Oncol.* **103**: S334–S335.

Fast, M., Oelfke, U. & Nill, S. (2013). Actively triggered cone-beam CT acquisition based on electromagnetic respiratory motion tracking, *Radiother. Oncol.* **In Press.**

Work presented in this thesis also had an impact on another peer-reviewed journal article:

Krauss, A., Fast, M., Nill, S. & Oelfke, U. (2012). Multileaf collimator tracking integrated with a novel x-ray imaging system and external surrogate monitoring, *Phys. Med. Biol.* **57**(8): 2425–2439.

A student's project, jointly supervised by Prof. Dr. Uwe Oelfke, Dr. Simeon Nill and the author, was based on work presented in this thesis:

Wisotzky, E., Fast, M., Nill, S. & Oelfke, U. (2012). Su-c-213cd-01: Automated marker tracking for intra-fractional image guidance in radiotherapy, *Med. Phys.* **39**(6): 3604.

Chapter 2

State of the Art in Motion Management

2.1 Overview

Managing the motion of a patient during radiation therapy, specifically during a single treatment session, can be split into a multi-step process:

- the patient motion needs to be reliably detected,
- the treatment delivery needs to be adapted accordingly,
- the delivered dose needs to be accounted for.

While this thesis focusses very much on the first link of the motion management chain, a summary of all the steps required for a comprehensive motion management strategy is given in this chapter.

Vision

In an ideal world (figure 2.1), the perfect treatment device would continuously monitor the tumour as well as the surrounding anatomy by acquiring 3d images of the patient in real-time. Feature-detection algorithms would then reliably detect the movement of the tumour and neighbouring organs-at-risk. Based on this anatomical information, the treatment beam would be directed at the tumour while sparing the healthy tissue as much as possible. Crucially, the anatomical information would also be used to keep track of the radiation dose *actually* delivered during a single treatment session. Comparing the *actually* delivered dose with the *prescribed* dose distribution (which is based on a planning CT acquired days-to-weeks before the first treatment session) would then enable on-the-fly adaptation of the treatment plan, a procedure known as *online replanning* or more universally as *adaptive radiation therapy* (Yan et al. 1997).

Real-world technical and computational constraints, however, mean that we are still a long way off from the described treatment scenario. This chapter will nevertheless show that progress is being made in all the described links of the motion management chain.

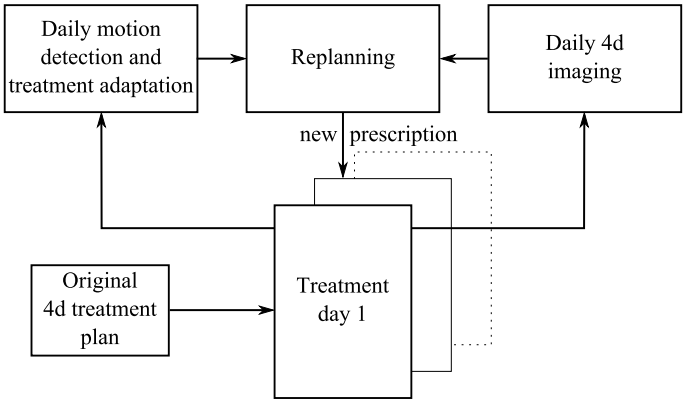

Figure 2.1 Vision of a future *adaptive radiation therapy* (ART) treatment regime. The new treatment plan can be enacted immediately ('online replanning') or during the next treatment session ('offline replanning').

2.2 Detection of patient motion

There are different technologies currently available for detecting the motion of a patient during the treatment session. One can differentiate between technological categories such as image-based vs. non-image-based, ionizing vs. non-ionizing, invasive vs. non-invasive procedures, direct vs. surrogate-based motion monitoring, detection of internal motion vs. external motion etc. The term *image-guided radiation therapy* (IGRT) is frequently used, whenever anatomical images detect the target motion. Generally, technologies that have little impact on the patient (e.g. non-ionizing or non-invasive) and vice versa are preferred. Information about the internal motion trajectory is usually considered more valuable than external motion such as chest-wall displacement during breathing. Other important factors of differentiation are the cost and ease of operating any of these technologies. Also the general device performance in terms of update frequency, latency and accuracy needs to be considered.

Table 2.1 summarizes the currently available and suggested (future) motion detection devices (especially MRI i.e. magnetic resonance imaging) as well as their most striking characteristics.

2.2.1 X-ray imaging

X-ray imaging on linear accelerators (linacs) is performed using either the treatment beam, some modification of the treatment beam, or additional diagnostic x-ray sources. Regardless of how the x-ray imaging beam is generated, it is usually detected by an energy-integrating *flat-panel detector* (FPD, sidebar 2.1) upon exiting the patient. The governing principle for exposing patients to ionizing x-rays is called *ALARA* (Brateman 1999), which means that the additional exposure through imaging must be kept *as low as reasonably achievable* to reduce the secondary cancer risk. Figure 2.2 depicts the different imaging geometries for intra-fractional x-ray imaging:

- *in-line MV*: the megavoltage (MV) treatment beam is used for imaging. The imaging field-of-view is identical to the treatment field size. An *electronic portal imaging device* (EPID, sidebar 2.1) acquires the images.
- *orthogonal kV*: the kilovoltage (kV) x-ray source is mounted on the linac gantry (sidebar 2.2) at 90° or 270° with respect to the treatment beam. An additional FPD is installed opposite to the x-ray source.

Table 2.1 Summary of various motion detection devices.

Device	Characteristics	References
External motion sensors		
Pressure-belt	Chest-wall displacement may not correspond to tumour motion	Li et al. (2006)
Optical sensor, Infra-red sensor	Needs additional cameras and reflective markers on patient	Bert et al. (2005)
Ionizing internal motion sensors		
Monoscopic x-ray, Stereoscopic x-ray, Tomosynthesis	Radiation dose, additional x-ray imager(s) needed, implanted markers beneficial	Section 2.2.1
Non-ionizing internal motion sensors		
Spirometer	Tidal volume correlates to diaphragm not tumour	Hanley et al. (1999)
Ultrasound	Robotic arm needed to ensure acoustic coupling	Hsu et al. (2005)
Electromagnetic	EM transponders need to be implanted	Balter et al. (2005), Shah et al. (2011)
MRI	Integration with linac highly complex; not yet available	Lagendijk et al. (2008), Fallone et al. (2009)

- *in-line kV*: the kV x-ray source is mounted at 180° with respect to the treatment beam. An additional FPD is installed underneath the treatment head. It is not practical to simultaneously deploy an EPID in this geometry. Imaging and treatment fields may overlap on the FPD (chapters 3 & 4).

- *stereoscopic kV*: two kV x-ray sources and two FPDs are needed for dual view imaging. The imaging equipment can be gantry-mounted or room-mounted. In one of the tomosynthesis approaches (section 2.2.2), even more x-ray sources are deployed.

In intra-fractional motion monitoring, one differentiates between target motion orthogonal and parallel to the treatment beam. X-ray beams such as the MV treatment beam show a characteristic depth dose profile (figure 2.3 (b)), which is dominated by the built-up region close to the entrance surface and the exponential dose fall-off with penetration depth. The lateral beam profile, i.e. the profile orthogonal to the penetration depth, is given by the primary field shape (a box function). Some blurring occurs along the field edges because of x-ray and secondary particle scatter (figure 2.3 (a)).

The monoscopic *in-line MV* and *in-line kV* imaging geometries monitor both motion axes orthogonal to the treatment beam. This type of motion is especially important since it can shift the target out of the beam and healthy adjacent organs into the beam by crossing the steep dose gradients of the treatment field edge (figure 2.3 (a)). The monoscopic *orthogonal kV* imaging geometry only detects motion along one of the two critical axes. The second dimension of the detector covers motion parallel to the treatment beam. This parallel motion, however, is less relevant since it follows the shallow dose gradients along the penetration depth of the treatment beam (figure 2.3 (b)). A detailed comparison of the advantages and disadvantages of the various imaging geometries for intra-fractional imaging can be found in Nill et al. (2005) and Suh et al. (2007).

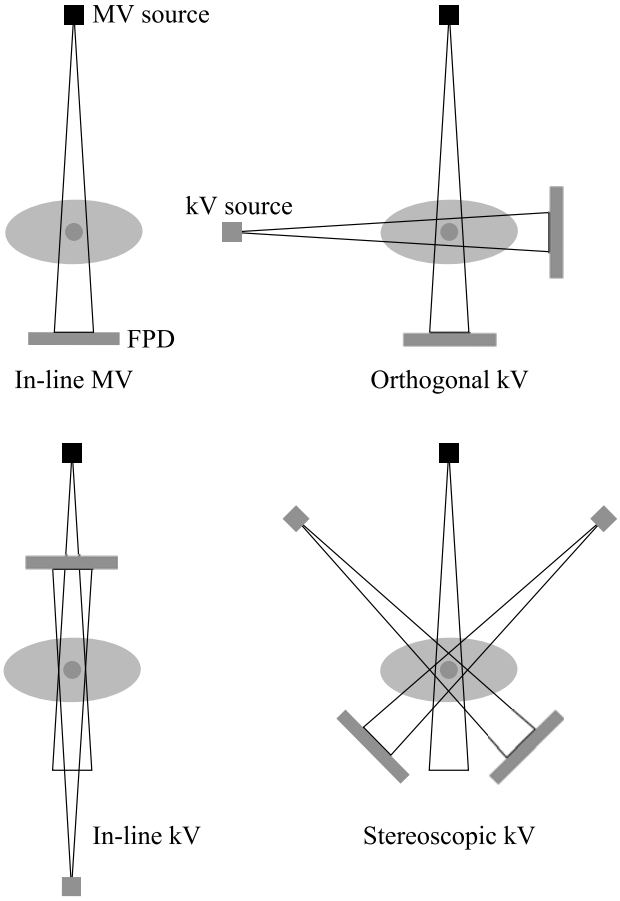

Figure 2.2 Overview of linac-mounted x-ray imaging geometries used for intra-fractional monitoring of motion. Note the relative orientation of imaging and treatment beam.

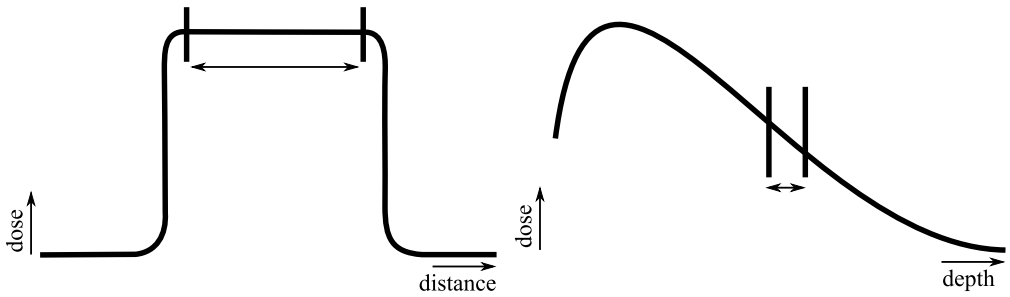

(a) Lateral dose profile. (b) Depth dose profile.

Figure 2.3 Typical dose gradients of an MV treatment beam. The tumour position is indicated by the vertical bars and connecting horizontal arrows.

Treatment beam imaging

The MV treatment beam has been used for a long time to verify the position of the patient just prior to treatment, first with analogue optical systems and later with EPIDs. Inter-fractional shifts of the patient were detected by acquiring two orthogonal projections and shifting the patient according to the bony anatomy (which is clearly resolved in MV images). The introduction of faster EPIDs, with read-out frequencies above 10 Hz, allowed one to think about real-time monitoring of the patient with the treatment beam for the first time. The biggest advantage of intra-fractional MV imaging is that the anatomical information is essentially *free* in terms of

Sidebar 2.1 Flat-panel detector (FPD)

A flat-panel detector (FPD) or flat-panel imager (FPI) is an areal x-ray detector that is used to form an x-ray projection image of the patient's anatomy. In the context of x-ray imaging with the MV treatment beam, the FPD is often referred to as electronic portal imaging device (EPID). Historically, EPIDs were the first digital x-ray detectors in radiotherapy applications to replace the previous generations of analogue imagers (e.g. radiographic films). The typical detection area of an FPD is in the range of 20x20 cm^2 to 41x41 cm^2, with between 256x256 and 2048x2048 pixels. Read-out frequencies range from 1-2 fps for older-generation devices to 15-30 fps for modern units.
Due to relatively high photon fluxes in x-ray imaging ($\sim 10^9$ photons s^{-1} mm^{-2}) (Overdick et al. 2009), all current FPDs are energy-integrating detectors without energy resolution. Future detector generations might be able to differentiate single interaction events which has the potential to greatly improve image quality (Shikhaliev 2008). For the conventional energy-integrating detectors, however, one differentiates between two detection principles:

- *direct* detectors: a semiconductor (i.e. photoconductor) is used to absorb incoming x-rays and convert the transferred energy into electron-hole pairs (EHPs). A bias voltage is then applied across the photoconducter (amorphous selenium is a typical choice of materials (Kasap & Rowlands 2002)), and the EHPs are collected and integrated by the bias electrodes.

- *indirect* detectors: a phosphor screen absorbs incoming x-rays and creates secondary electrons (Antonuk et al. 1992). These secondary electrons in turn facilitate the creation of optical photons by scintillation. Crucially, the number of optical photons is assumed to be correlated to the amount of absorbed energy. The visible light then propagates through the transparent phosphor until it is detected by the adjacent array of hydrogenated amorphous silicon (a-Si:H) photodiodes. These photodiodes then efficiently collect the optical photons and convert their energy into charge. Typical phosphor materials are gadolinium oxysulfide (GOS) and caesium iodide (CSI) (Eijk 2002).

In this thesis, only the indirect detector type was used. The technical realisation of compact FPDs heavily relied on the substantial progress made in semiconductor technology in the 1980s and 1990s (Antonuk et al. 1990, Antonuk et al. 1992). The possibility to fabricate large area thin-film transistors (TFTs) allowed to miniaturise the detector read-out and achieve sub-mm pixels.

additional imaging dose, since the treatment beam is deployed in any case. Most modern linacs are already equipped with an EPID, which also explains the appeal of MV imaging for intrafractional imaging. Numerous studies (Berbeco et al. 2007, Park et al. 2009, Poulsen et al. 2012) have demonstrated the capability of MV imaging for reliably detecting implanted metallic markers (which act as surrogate for the tumour motion). Rottmann et al. (2010) have proposed a multi-region tracking algorithm that selects and follows distinct landmarks from the portal MV images acquired during treatment.

The reason that markerless tracking approaches have not gained more traction, has to do with the physical properties of the MV imaging beam. Polyenergetic x-ray beams traversing through matter interact and the exit intensity I is given by the Lambert-Beer law:

$$I = \int_0^{E_{max}} I_0(E) \exp\left(-\int_0^d \mu(E,x)\,dx\right) dE. \tag{2.1}$$

Here, I_0 denotes the entrance intensity, E_{max} the maximum x-ray energy, and d the penetration depth. The linear attenuation coefficient μ, which depends on the x-ray energy E, the location x, the atomic number Z, the mass number A, the Avogadro constant N_A, the electron density ρ, and the interaction cross-section σ is defined as:

$$\mu = \sigma(E,Z,x) \cdot \rho(x) \cdot \frac{N_A Z}{A}. \tag{2.2}$$

Figure 2.4 (a) shows the density-independent mass absorption coefficient $\frac{\mu}{\rho}$ of water. In the energy range relevant for x-ray imaging and therapy (10 keV to 20 MeV), the main interactions are the photo-electric effect, Compton scattering (i.e. incoherent scattering), and nuclear pair production. Figure 2.4 (b) demonstrates that MeV x-rays, which mainly interact via Compton scattering, cannot differentiate between soft tissue and cortical bone based on the mass absorption coefficient alone. Fortunately, differences in electron density still allow one to differentiate between soft tissues and bone. Due to the relatively small differences in electron density between different soft tissues (e.g. muscle, fat, brain tissue, etc.), MV imaging cannot distinguish between these tissues (Johns & Cunningham 1983). For x-ray energies well below 100 keV, however, photo-electric absorption is the dominating interaction. The strong Z-dependence of the photo-electric effect results in excellent differentiation between soft tissues for kV imaging.

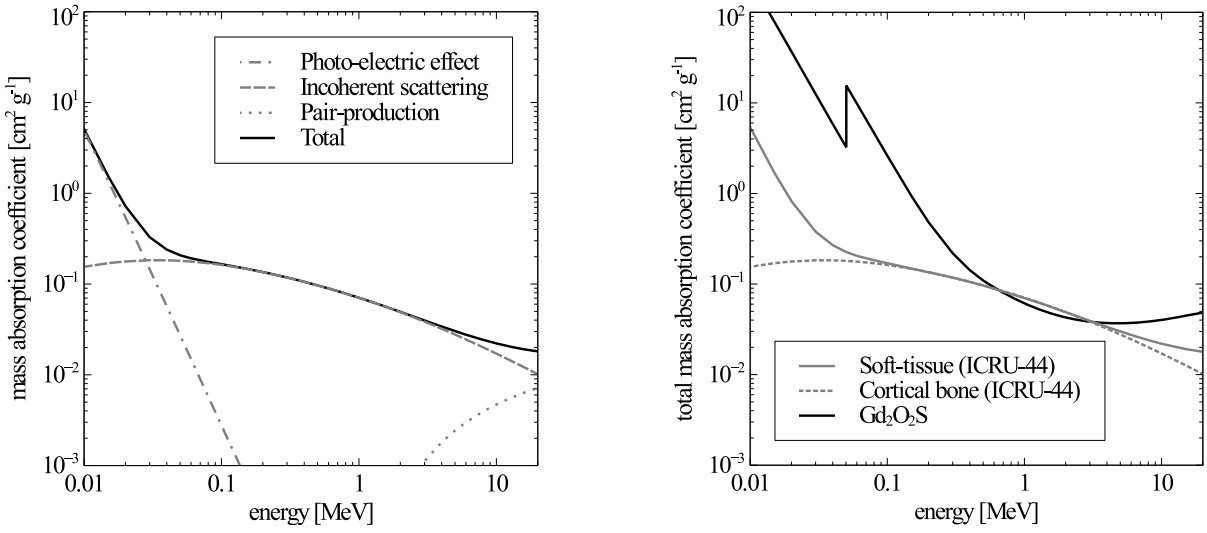

(a) H_2O. (b) Various compounds.

Figure 2.4 Mass absorption coefficients were retrieved from the *National Institute of Standards* (NIST) homepage (*XCOM* 2013). (a) Different x-ray absorption effects for water. Coherent scattering and electronic pair production are not shown. (b) Total absorption for different anatomical tissues and gadolinium oxysulfide (a typical scintiallator used for x-ray imaging).

Conventional EPIDs are highly inefficient at absorbing MV x-rays despite their use of Copper built-up plates to increase the number of secondary particles that interact in the scintillating layer (Jaffray et al. 1995, Groh et al. 2002). Figure 2.4 (b) exemplifies the mass absorption capabilities of gadolinium oxysulfide (Gd_2O_2S) which is a typical scintillator used in FPDs. Clearly, the scintillator absorbs much more at keV energies due to its high effective Z. At MeV energies, the x-ray absorption of the scintillator is up to two orders of magnitude smaller than for keV energies.

A number of alternative scintillator materials and technologies have been suggested for improving the detector's sensitivity for MV x-rays and thus increasing the dose utilisation: e.g. thick and segmented CsI and BGO scintillators (El-Mohri et al. 2011), $CdWO_4$ (Kirvan et al. 2010), and UFC (Maltz et al. 2009 b). Recently, Teymurazyan & Pang (2013) have suggested a scatter-rejecting *Cerenkov electronic portal imaging device* (CPID) which is based on a matrix of optical fibres aligned with the treatment beam. None of these technologies, however, are currently available for clinical practise.

Another principle limitation of treatment beam imaging is the shape of the treatment field, since it also dictates the imaging field-of-view. Especially in IMRT treatments, single treatment fields do not necessarily cover the entire tumour or even the surrogate markers. Using the treatment beam in such situations to detect the tumour motion therefore renders tracking applications more complicated and gating applications close to impossible.

Enhanced megavoltage (MV) imaging

The physical limitations of treatment beam imaging, detailed in the previous section, have led to a number of developments that try to achieve better quality images with a modified treatment beam. A common theme behind these approaches is to reduce the electron energy to 3-4 MeV to create 'softer' bremsstrahlung spectra. Additionally, the conventional tungsten (Z=74) target is replaced by lower-Z materials to reduce the self-absorption of keV x-rays within the target itself. The following target materials were utilized: aluminium (Robar et al. 2009), copper (Tsechanski et al. 1998), carbon/graphite (Faddegon et al. 2008, Faddegon et al. 2010), and sintered diamond (Sawkey et al. 2010). All studies showed a marked improvement in image quality and/or dose savings due to the softer x-ray spectrum.

Recently, Roberts et al. (2012) were able to reduce the electron energy even further to 1.4 MeV. Combined with a very thin target (consisting of the stainless steel exit window of the accelerator, a 5 mm Carbon absorber, and a 2.5 mm Aluminium filter), the reduced electron energy resulted in great image quality increases compared to previous generations of low-Z/low-E systems. Roberts et al. (2012) quantify the cone-beam (CB) CT imaging dose as 12 times higher than for a kV CBCT system, but 140 times lower than a MV CBCT system, and 6 times lower than a low-Z (4-5 MeV) CBCT system.

Unfortunately, switching between targets and electron energies takes of the order of 1-5 seconds with today's system. Truly intra-fractional imaging is therefore not possible with low-Z and low-energy MV beams since the interruption of the treatment beam would be too long.

Kilovoltage (kV) imaging

The easiest solution for acquiring diagnostic-quality x-ray images is to mount an additional kilovoltage (kV) x-ray tube on the linac gantry. This x-ray tube allows to use a 80-140 kVp x-ray beam for intra-fractional kV imaging, resulting in an x-ray spectrum comparable to diagnostic CT scanners. Most previous publications have focussed on the orthogonal kV geometry as shown in figure 2.2 (Poulsen et al. 2010, Poulsen et al. 2010 b, Poulsen et al. 2010 d). In this thesis the focus will be on the in-line kV geometry (chapters 3 & 4).

Orthogonal kV imaging has also been combined with MV imaging to achieve 3d resolution (Wiersma et al. 2008, Cho et al. 2009, Cho et al. 2011, Yan et al. 2012). Cho et al. (2011) showed that the kV imaging frequency can be safely reduced to 1 Hz, when a correlation model is used to connect external motion with internal motion.

Stereoscopic kV systems require more imaging dose but also provide 3d information. Berbeco et al. (2004) demonstrated a high accuracy of such a system for intra-fractional 3d marker tracking.

Stereoscopic kV imaging is also included in the new VERO^{TM} treatment device (section 2.3.4). Commercially available room-mounted stereoscopic imaging systems are included in Accuray's CyberKnife^{TM} (Fu & Kuduvalli 2008, Kilby et al. 2010) and BrainLab's ExacTrac^{TM} (Jin et al. 2008, Vinci et al. 2008). The latter can be used in combination with conventional linacs. Room-mounted systems have the disadvantages of increased air scatter due to the relatively large source-to-detector distance and small field-of-views for the same reason. For certain gantry angles and positions, the view of one of the imagers can be obscured by the gantry.

2.2.2 Tomosynthesis

Tomosynthesis, sometimes referred to as 2.5d imaging in the context of radiation therapy, is a limited-angle CT reconstruction technique (Grant 1972). The original idea was to move the x-ray source and/or the imaging detector in two parallel planes (or in a short arc segment) and acquire a series of projection images. These images can then be used to reconstruct a quasi-3d rendering of the anatomy. Due to the missing information along the beam direction compared to a CT acquisition, the spatial resolution is rather poor in that direction (hence 2.5d). Using the conventional imaging equipment (Godfrey et al. 2006, Pang et al. 2008), tomosynthesis is not a viable option for real-time intra-fractional imaging due to the relatively long acquisition times. Recently, Maltz et al. (2009) have presented a compact multi-source array with 52 individual x-ray sources (driven by carbon nanotube cathodes) which can be mounted on the linac gantry. The authors argue that their system can in principle be used to acquire multiple x-ray projections (from slightly different angles) at once. Should such a system become clinically available, the benefit of having increased spatial information still needs to be weighed against the increased x-ray exposure through multiple projections.

2.2.3 Cone-beam computed tomography (CBCT)

Jaffray & Siewerdsen (2000) were the first to popularize the use of linac-integrated diagnostic x-ray equipment for computed tomograph (CT) applications. Later, MV CBCT was successfully demonstrated as well (Pouliot et al. 2005). Contrary to fan-beam CT scanners, a cone-shaped x-ray beam is used to acquire a 3d rendering of the internal anatomy in a single (or even partial) rotation of the linac gantry (figure 2.5). The CT images are usually reconstructed using the *Feldkamp-Davis-Kress* (FDK) algorithm (Feldkamp et al. 1984), which can be regarded as an extension of the filtered back-projection reconstruction algorithm developed for fan-beam CT. A detailed step-by-step guide to (CB)CT reconstruction is given by Kak & Slaney (1988).

CBCT imaging is not a truly intra-fractional modality[1] due to the minimum gantry rotation time of 1 min, but the CBCT scans are acquired immediately prior to treatment and are thus assumed to reflect the anatomy during treatment.

A recent enhancement of CBCT is respiratory-sorted 4d CBCT (Sonke et al. 2005) in which a video-like sequence of 3d CBCTs is reconstructed using information about the respiratory phase at the time of image acquisition. This technique will be introduced in greater detail in chapter 5.

2.3 Adaptation of treatment delivery

In this thesis, the focus is on radiation treatments performed on medical linear accelerators (linacs, see sidebar 2.2). These *external beam* deliveries present the bulk of all radiation treatments. On

[1] One notable exception is the work of van Herk et al. (2011) described in more detail in sidebar 3.1 which has demonstrated parallel rotational treatment and CBCT image acquisition.

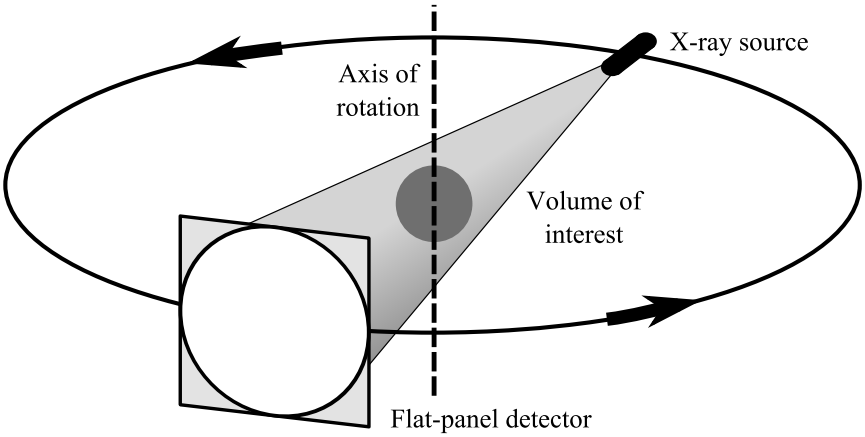

Figure 2.5 Schematic view of the cone-beam CT imaging geometry. Full (360°) or partial (200°) rotations provide the projection information necessary for a 3d reconstruction of the scanned volume of interest.

modern linacs there are a number of technologies available to adapt the treatment delivery to a moving target. In order of increasing technological complexity these are: (i) gating, (ii) couch tracking, (iii) MLC-tracking, and (iv) robotic tracking.

2.3.1 Gating

In gated radiation deliveries (Kubo & Hill 1996), a certain window (i.e. range) of acceptable tumour motion is defined prior to treatment. Irradiation is then allowed to proceed, whenever the tumour is within the predefined window. No radiation is administered as long as the tumour is outside this window. Switching radiation beams on or off can be done almost instantaneously and the shape of the radiation field does not need to be adapted, hence the ease of implementing this technology on any linac.

2.3.2 Couch Tracking

The idea behind couch tracking is to adapt the position of the treatment couch (sidebar 2.2), and hence the patient, continuously during treatment. Conventional treatment couches usually have four degrees of freedom: three translational axes for vertical, lateral and longitudinal shifts, and a rotational axes about the isocentre. Some couches also feature an additional vertical rotation axis, parallel to the isocenter axis. These degrees of freedom have long been used in clinical practise to compensate for inter-fractional changes in the patient's anatomy. Many modern robotic couches also allow slight rotations about the longitudinal and lateral axes ('roll' and 'pitch').

Equipping all or at least the most relevant motion axes of the couch with remotely controlled motors, makes it possible to dynamically counter the patient motion during therapy without changes to the beam delivery. Several research groups have demonstrated couch tracking (D'Souza & McAvoy 2006, Wilbert et al. 2008, Menten et al. 2012), but no commercial systems are available as of today. An issue often raised in the context of couch tracking is the patient comfort under couch accelerations and rotations.

2.3.3 MLC-Tracking

The idea behind this type of tracking is to continuously adapt the shape of the treatment field with the aid of a *multi-leaf collimator* (MLC) to effectively follow the tumour during irradiation. The

Sidebar 2.2 Medical linear accelerator (linac)

First of all it should be clarified that the term *linear accelerator* or linac is used to describe both the central component of each radiation treatment device (which is used to accelerate electrons to megavoltage energies) and the entire treatment device. This sloppiness in terminology might be confusing at first, but it has been widely adopted in the literature.
The photo[a] below shows the Siemens Artiste^{TM} research linac and the treatment couch used for most experiments in this thesis.

The central components of any linac are the electron injector, the (linear) accelerating waveguide which brings the electrons up to megavoltage (MV) energies, and the bremsstrahlung target which slows down the electrons and produces the x-ray beam used for treatment (and sometimes imaging). Other ancillary components such as the radio-frequency (RF) power generator which drives the accelerating waveguides and the electron transport system which guides the electrons from the waveguide to the bremsstrahlung target are of equal importance. The entire set-up is mounted on a moveable gantry and can usually rotate 360° around the treatment isocenter.
The reader is referred to Karzmark & Morton (1989) and Podgorsak et al. (2005), chapter 5.5 for comprehensive overviews on the principal components of modern linacs.

[a] Courtesy of Eric Wisotzky.

MLC is an add-on device that is positioned between the bremsstrahlung target of the linac and the patient. MLCs usually consist of two opposing banks of thick high-Z (e.g. tungsten) blades/leaves and were originally conceived to create non-quadratic treatment fields without the need for a separate collimator for each new field shape. They then became very useful in creating the complex field shapes used for *intensity-modulated radiation therapy* (IMRT). First suggested by Keall et al. (2001), the concept of 'breathing leaves' which follow the treatment target during the course of a therapy session has now been demonstrated in combination with prediction algorithms that compensate for the system's latency by many other research groups (McQuaid & Webb 2006, Tacke et al. 2007, Sawant et al. 2008).

2.3.4 Robotic Tracking

All robotic tracking approaches require to install the linear accelerator on a dedicated mounting with additional degrees of freedom compared to the traditional linacs.

CyberKnife

The CyberKnife™ (Accuray Inc., USA) treatment device features a compact 6 MV X-band linac which is mounted on an industrial robot. Schweikard et al. (2004) were the first to demonstrate lung tumour tracking on a modified CyberKnife system. Currently, it is the only widely used system for dynamic tumour tracking.

VERO system

The VERO™ system (BrainLAB AG, Germany & Mitsubishi Heavy Industries, Japan) is a new treatment device especially developed for tumour tracking applications (Kamino et al. 2006). It features a 6 MV C-band linac mounted on a ring gantry (not unlike the design of a CT scanner). The entire acceleration waveguide together with an MLC is gimbal-mounted, meaning that it can perform pan and tilt rotations resulting in ±4.2 cm swings of the MV beam at the isocenter (Takayama et al. 2009). Depuydt et al. (2011) were able to show the high sub-mm tracking accuracy of the VERO system and measure its relatively short latency of only ∼50 ms. First patient studies of dynamic tumour tracking with the VERO system have been reported (Hiraoka et al. 2012).

2.4 Confirmation of delivered dose

The final link of the motion management chain is the verification of the *actually* delivered dose during a single treatment fraction. One approach involves small localised dosimeters that are either attached to the patient surface or implanted into the patient for *in vivo* dosimetry (Mijnheer 2008). The issue with this method is that it often does not allow one to monitor the dose in real-time. It is also questionable to what extent a number of localised dose measurements correspond to the total delivered dose, especially for highly complex IMRT treatments.

To develop a *portal dosimeter* (Mijnheer 2008) that operates in real-time and is suitable for IMRT treatments, a lot of research has been carried out on using the FPD/EPID to continuously monitor the exit fluence during treatment (similar to the MV imaging approach discussed in section 2.2.1). It is debatable whether this type of dose measurement really constitutes an *in vivo* ('within the living') measurement[2], since it is technically a measurement of photons that do *not* deposit dose in the patient. Additionally, the imaging detector does not simply measure the x-ray spectrum. Instead, it effectively convolutes its energy-specific response function with the incident x-ray spectrum. Since the detector is not made of water-equivalent materials, the measured signal cannot simply be interpreted as a water-equivalent dose (Greer & Popescu 2003). Two different approaches have been reported in the literature to implement transmission dosimetry:

- *forward-projection*: The portal image of any treatment beam can be predicted from the planning CT (Pasma et al. 1998, Nijsten et al. 2004). The issue with this approach is that the EPID can only measure the dose accumulated along the beam direction (or rather the beam fraction *not* absorbed in the patient), but this does not necessarily reflect the dose distribution within the patient.

[2] A lively discussion on the merits of *portal dosimetry* has been witnessed by the author at the EPI2k12 conference in Sydney, Australia (March 2012).

- *back-projection*: In this approach, the transmission dose is corrected for any scatter contribution to extract the primary beam signal and then back-projected into the patient (Boellaard et al. 1998, Partridge et al. 2002, Wendling et al. 2006). Back-projecting a 2d dose distribution as measured at the detector plane into a 3d dose deposition within the patient requires a few additional steps: modelling of the beam built-up at the patient surface, scattering within the patient, and beam hardening (Wendling et al. 2009).

2.4.1 Outlook

In future, the MRI-linac concept (Lagendijk et al. 2008) will hopefully allow the acquisition of 3d images during irradiation in parallel to the exit fluence dosimetry. Unfortunately, the MR images do not correspond to the electron density distributions required for treatment planning. It will therefore be necessary to map the 3d MR images onto 3d planning CT images using non-rigid registration methods (with all the accompanying uncertainties) to calculate pseudo-CT images on-the-fly. It should then be possible to forward-project the treatment beam onto the EPID *and* back-project the EPID measurement into the 3d patient volume at the time of irradiation. Based on this information, the treatment plan could be adapted on-the-fly or for the next treatment session as outlined in section 2.1.

Chapter 3

A Novel Method for Intra-Fractional Motion Management

3.1 Overview

We have developed a system that monitors intra-fractional target motion perpendicular to the treatment beam with the aid of radioopaque markers by means of separating kV image and MV treatment field on a single flat-panel detector.

For the experiments presented in this chapter, we equipped a research linac with a 41x41 cm^2 a-Si flat-panel detector mounted underneath the treatment head. Our unique 'in-line' geometry allows kV (imaging) and MV (treatment) beams to share closely aligned beam axes. The kV source, usually mounted directly across from the flat-panel imager, was retracted towards the gantry by 13 cm to intentionally misalign kV and MV beams. This resulted in a geometric separation of MV treatment field and kV image on the detector. Two consecutive images, acquired within 140 ms (the first with MV-only and the second with kV and MV signal), were subtracted to generate a kV-only image. The images were then analysed 'online' with an automated threshold-based marker detection algorithm. We employed a 3d and a 4d phantom equipped with either a single radioopaque marker or three Calypso® (Varian Medical Systems, Inc.) beacons to mimic respiratory motion. Measured room positions were either cross-referenced with a phantom voltage signal (single marker) or the Calypso system. The accuracy of our back-projection (from detected marker positions into room coordinates) was verified by a simulation study.

Based on the evaluated motion patterns and MV field size, the positional accuracy and system latency indicate that this system is suitable for real-time adaptive applications.

Publication

This chapter has been published in Fast et al. (2012). Parts of the results have been presented at international conferences (Fast et al. 2011, Fast et al. 2011 b). Methods described in appendix 3.A were presented by the author at the *Electronic Patient Imaging 2012* conference (EPI2k12) in Sydney, Australia (March 2012).

Acknowledgement

The authors would like to thank Frank Verhaegen (MAASTRO, McGill University) for suggesting to shift the x-ray source towards the gantry.

3.2 Introduction

In modern image-guided radiation therapy (IGRT) treatments, a number of imaging techniques such as cone-beam computed tomography (CBCT) have helped to reduce the impact of inter-fractional organ motion on dosimetric accuracy. Today, highly conformal tumour dose distributions are routinely used to irradiate patients. When applying margin strategies, the effect of intra-fractional motion is accounted for at the cost of healthy tissue irradiation. In order to manage intra-fractional motion efficiently and reduce margins accordingly, we have developed a linear accelerator integrated x-ray imaging framework which can monitor the target location in respect to the treatment field over the course of a treatment fraction either continuously or on demand. Due to the unique in-line geometry of our x-ray imaging equipment, this system is capable of tracking most tumour and organ motion perpendicular to the treatment beam, the direction that usually features steep dose gradients (section 2.2.1). Orthogonal x-ray geometries on the other hand are limited to motion parallel to the treatment beam where dose gradients are lower, and a single axis perpendicular to the treatment beam. The advantages and disadvantages of in-line and orthogonal geometry have been discussed by several authors (Nill et al. 2005, Suh et al. 2007).

Based on real-time information about the target location, several attempts of motion compensation such as gating (Kubo et al. 2000, Shirato et al. 2000, Korreman et al. 2008), table tracking (D'Souza & McAvoy 2006, Wilbert et al. 2008, Buzurovic et al. 2011), robotic arm tracking (Schweikard et al. 2004) or MLC tracking (Keall et al. 2001, Tacke et al. 2010) have been evaluated. We have demonstrated a dynamic tumour tracking control system capable of adapting the aperture of a Siemens 160 MLC^{TM} (multi-leaf collimator) in real-time to the target position (Tacke et al. 2010, Krauss et al. 2011 b). Using electromagnetic target localization, multiple authors have reported considerable improvements in dosimetric accuracy for conformal radiotherapy and IMRT treatment fields (Tacke et al. 2010, Krauss et al. 2011 b, Smith et al. 2009, Keall et al. 2011).

Intra-fractional imaging was either approached by utilizing megavoltage (MV) images (Poulsen et al. 2012), kilovoltage (kV) images (Poulsen et al. 2010 d, Poulsen et al. 2010, Poulsen et al. 2010 b) (acquired orthogonally to the treatment beam), a combination (Wiersma et al. 2008, Cho et al. 2009) of both approaches, or room-mounted stereoscopic imaging systems such as Accuray's CyberKnife^{TM} (Fu & Kuduvalli 2008, Kilby et al. 2010) and BrainLab's ExacTrac^{TM} (Jin et al. 2008, Vinci et al. 2008). Images were also combined with external motion surrogates (Cho et al. 2010, Cho et al. 2011). While stereoscopic imaging systems offer superior 3d resolution (Berbeco et al. 2004), monoscopic systems can be enhanced with a probability-based estimation of 3d positions from 2d projections (Poulsen et al. 2010 d, Poulsen et al. 2008, Li et al. 2011). Markerless approaches using MV cine images have been demonstrated for lung tumour tracking (Rottmann et al. 2010). All MV imaging approaches monitor the same target motion as our kV system. The inherent poor contrast resolution of MV imaging, however, limits its use to high-contrast objects such as lung tumours and implanted radioopaque markers. An optimal tracking performance with MV images is achieved for conformal fields, whereas IMRT-like field segments reduce the MV field-of-view (FOV).

The aim of this study was to utilize x-ray images to compensate for the dosimetric effect of intra-fractional motion. In contrast to other approaches, we aimed at monitoring target motion perpendicular to the treatment beam with kilovoltage image quality. We developed a new imaging framework that handles image acquisition, automated marker detection and communication to the DKFZ tracking tool to allow for dynamic treatment adaption. In order to verify the feasibility of our imaging system for detecting target positions, we have performed simulations as well as phantom experiments.

3.3 Materials and methods

The experimental set-up (figure 3.1) at a Siemens Artiste^{TM} research linear accelerator employed an additional 41x41 cm^2 amorphous silicon (a-Si) flat-panel detector (FPD) mounted underneath the treatment head. The in-line geometry, previously presented by Oelfke et al. (2006), allows kV (imaging) and MV (treatment) beams to share two identical or closely aligned beam axes. The Siemens Optitop 150/40/80 HC-100 diagnostic x-ray tube, usually mounted directly across from the flat-panel imager, was retracted towards the gantry by approximately 13 cm (+y direction) to intentionally misalign kV and MV beams by 5.4°, resulting in a geometric separation of the MV treatment field and the kV image on the detector. We used a conventional XRD 1640 AN9-ES FPD (PerkinElmer Inc, MA, USA) without its 1 mm Cu build-up plate for our experiments. All coordinates used in this chapter are given as specified in figure 3.1 according to IEC convention (IEC 1996). The source-to-detector distance (SDD) in this experiment was 136.5 cm, i.e. 10x10 cm^2 isocentric MV fields are seen as 6.4x6.4 cm^2 fields on the detector. The source-to-isocenter distance was 100 cm. The +y side of the x-ray source aperture was positioned in such a way that panel read-out electronics was not exposed to primary kV radiation. On the other hand, the -y side of the aperture was opened to allow for a maximum field size in that direction.

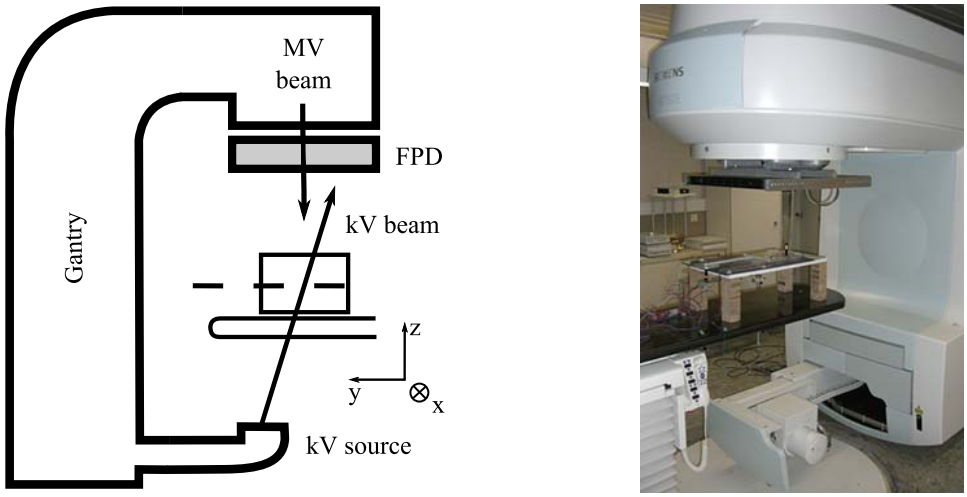

Figure 3.1 Principle experimental set-up (side views). The lateral axis (x), longitudinal axis (y), and vertical axis (z) are specified.

3.3.1 Image acquisition

Because of the comparatively high photon fluxes (at a dose rate of 300 MU/min) and the detector's close proximity to the MV radiation source, it was necessary to select the lowest detector gain setting (8 pF) and the fastest read-out time (66.6 ms). To avoid detector saturation due to high levels of MV radiation, panel read-out was triggered every 70 ms (allowing for a few milliseconds of contingency between each panel trigger). This resulted in a frame rate of 14.3 Hz. A detector gain setting of 8 pF would usually not be chosen in kV imaging and comes at a cost of decreased image quality. For gain settings of 4 pF and lower, detector saturation was observed at the maximum read-out frequency of 15 Hz.

The geometric separation mentioned above was necessary in order to maximize the quality of the kV image information. Because the MV signal outnumbers the kV signal by a factor of >50 for the central region of the detector, two consecutive frames (the first with MV-only and the

second with kV and MV signals) were subtracted to generate a kV-only image (sidebar 3.1). By triggering an x-ray pulse and the detector simultaneously within a sub-ms tolerance using an in-house developed *X-ray controller* (sidebar 3.2), it was possible to maximize the kV-to-MV signal ratio. Since two subsequent frames are acquired within 140 ms, the deduced kV image is inherently offset-corrected and almost free of (MV) ghosting artefacts.

Sidebar 3.1 MV subtraction method

The figure below demonstrates how the subtraction of an MV-only frame (centre) from a subsequent kV-and-MV frame (left) greatly increases the visibility of the marker (right). It also becomes clear that the primary MV region of the image is still not usable after subtraction due too the high noise level. The characteristic synchronization 'stripe' artefacts (explained in sidebar 3.3) occur in the MV-only frame and the kV-and-MV frame. The absolute position of the stripes is shifted between those two frames, leading to white and dark stripes in the subtracted frame.

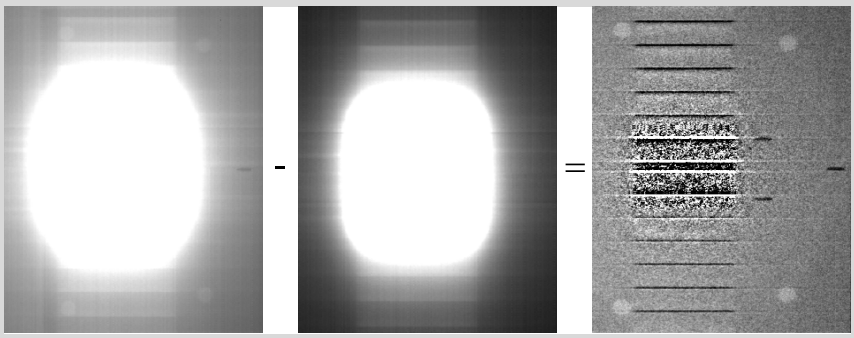

A conceptually similar correction strategy for MV scatter during kV CBCT acquisitions in the orthogonal imaging geometry was developed by van Herk et al. (2011). In their application, a kV CBCT is acquired during a continuous rotational irradiation of the patient. They estimated the MV scatter onto the imaging detector from kV-off frames and also accounted for kV detector lag (i.e. ghosting). Importantly, the MV-to-kV signal ratio is substantially lower in their application which makes corrections easier.

X-ray source trigger pattern

Conventionally, x-ray source and FPD are triggered sequentially (figure 3.2 (a)). For our system this approach would limit the effective panel read-out frequency to approx. 12.5 Hz (assuming an x-ray emission time of 13.4 ms) and thus lead to a decreased kV-to-MV signal ratio. Triggering x-ray source and FPD at the same time (figure 3.2 (b)), does however come at the cost of a reduced FOV. The FPD is divided into two subpanels with 512 rows of 1024 pixels each. Image acquisition starts by reading the outer (opposing) rows of each subpanel in parallel and finishes by reading the inner (adjacent) rows of the subpanels. Again, assuming 13.4 ms of x-ray emission time and a detector read-out time of 0.13 ms per row, this leaves approx. 100 rows on each side exposed to only a fraction of the kV signal and thus reduces the FOV in read-out direction to 22.7 cm at the isocenter (given a typical SDD of 145 cm). While this would not be tolerated in applications such as CBCT, it is not a relevant limitation for our system due to the central location of the region-of-interest (ROI).

Sidebar 3.2 The X-Ray controller

The *X-ray controller* is an in-house developed tool that combines hardware and software components to control the acquisition of x-ray images and offset images with the linac-integrated imaging equipment without using the vendor-supplied control software. Developing our own equipment was crucial for realising the kind of experiments described in this chapter and also in chapter 5. The first iteration of the *X-ray controller* was developed by the author during his diploma thesis (Steinke 2010). At that time, the controller was mostly used as a stand-alone utility. It was then extensively overhauled for use in this thesis: (i) a two-way communication between the *X-ray controller* and the imaging framework (section 3.3.3) or the *4d CBCT tool* (section 5.3.2) was established; and (ii) the simultaneous triggering of x-ray pulses and detector read-out (section 3.3.1) was implemented. The latter change required hardware as well as software modifications.

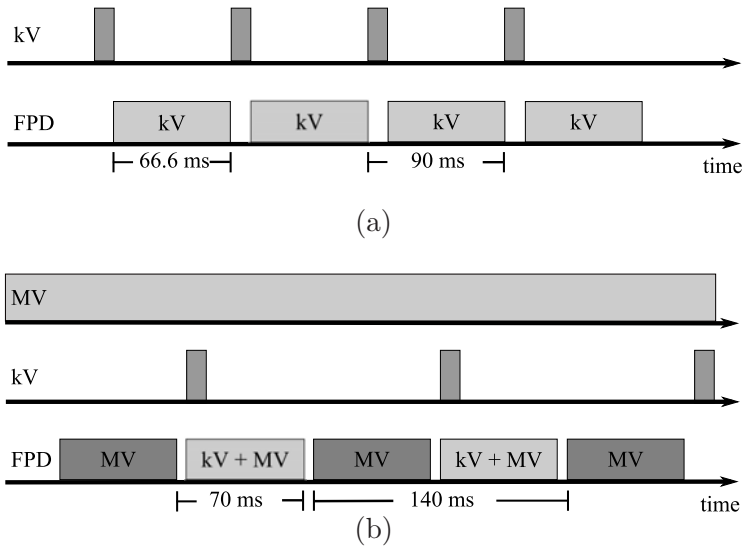

Figure 3.2 Trigger pulse pattern for conventional applications (a) such as CBCT and for our intra-fractional imaging system (b). The image content is kV, MV or kV and MV.

3.3.2 Image artefacts

Although we attempted to create kV-only images by means of subtraction, the image quality was still substantially degraded by an increased level of background noise and synchronization 'stripe' artefacts (sidebar 3.3 & figure 3.3). If the MV field shape is continuously adjusted by means of MLC tracking, an additional error occurs due to the difference in MV content of the two subtracted frames. Because MV exposure is much higher than kV exposure, we assume that MV-induced Poisson and electronic noise outweighs its kV counterpart. Naturally, our subtraction method cannot compensate for these random noise components.

3.3.3 Real-time image processing workflow

We developed an imaging framework (figure 3.4) that handles image acquisition, image post-processing as well as marker detection. The entire framework is coded in C++ with the exception of the marker detection algorithm which was implemented in Matlab® R2010b (The MathWorks,

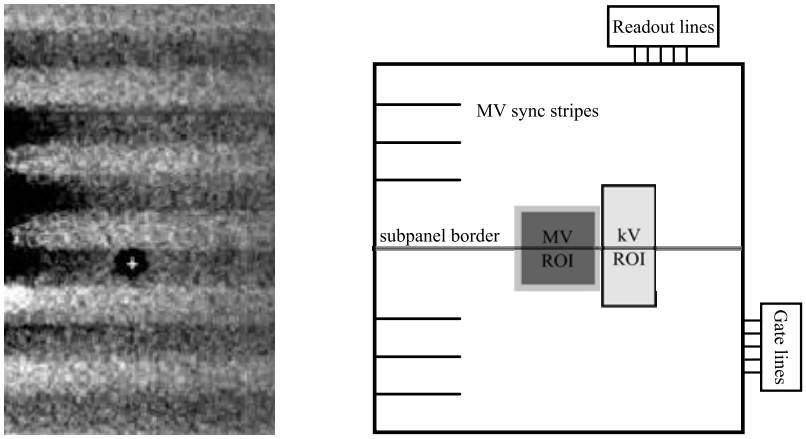

Figure 3.3 (a) Sample kV image with marker (marked by a cross) distorted from MV radiation. (b) Orientation of the stripes with respect to the MV and kV ROIs. Note that the sync stripes are simplified and really stretch across the entire detector (sidebar 3.3).

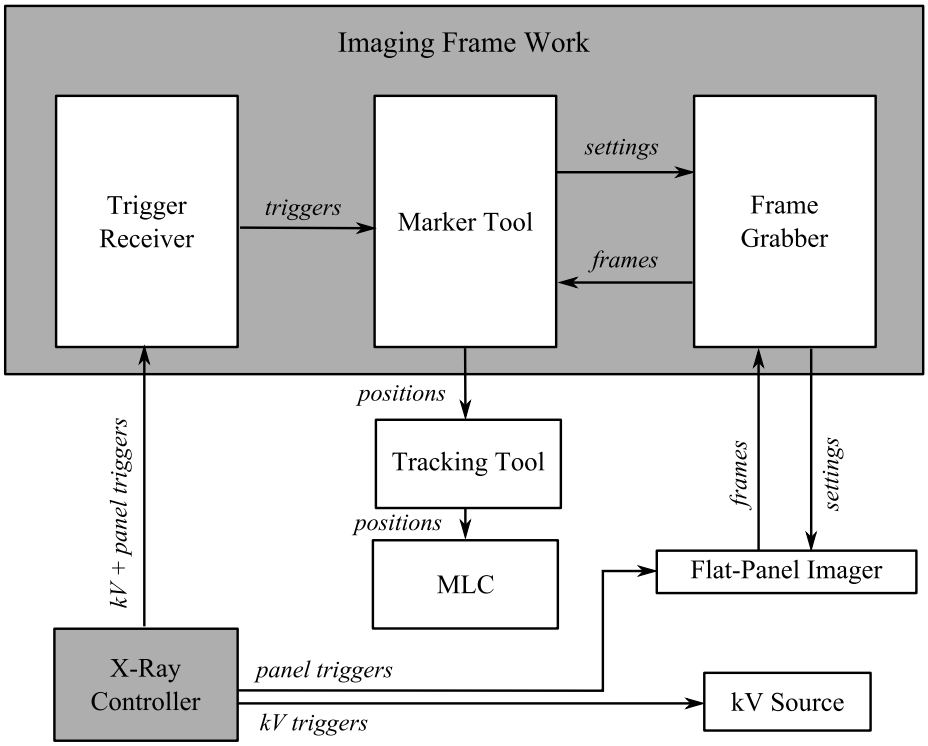

Figure 3.4 Schematics of the imaging framework and the *X-ray controller*. The imaging framework receives the trigger pulses through its trigger receiver and labels acquired flat-panel images according to its image content (kV, MV or kV+MV).

Inc.) and accessed through C++. The workflow as handled by the *MarkerTool* component of the imaging framework is as follows:

1. acquire kV+MV flat-panel image $N + 1$,
2. subtract MV-only image N for ROI,
3. perform image corrections,

Sidebar 3.3 MV synchronization 'stripe' artefact

For our linear accelerator, the distance between single dose pulses is roughly 4.25 ms at a dose rate of 300 MU/min. The detector read-out on the other hand takes 66.6 ms or longer. The detector rows that are read while the MV beam is emitted display a systematically higher count level known as synchronization stripe artefacts. Since detector read-out and MV pulses are not synchronized, the position of these stripes varies between frames. Recently, Mooslechner et al. (2013) have characterized the phenomena in greater detail. They propose a stripe correction strategy and demonstrate the efficient removal of stripe artefacts for traditional MV imaging.

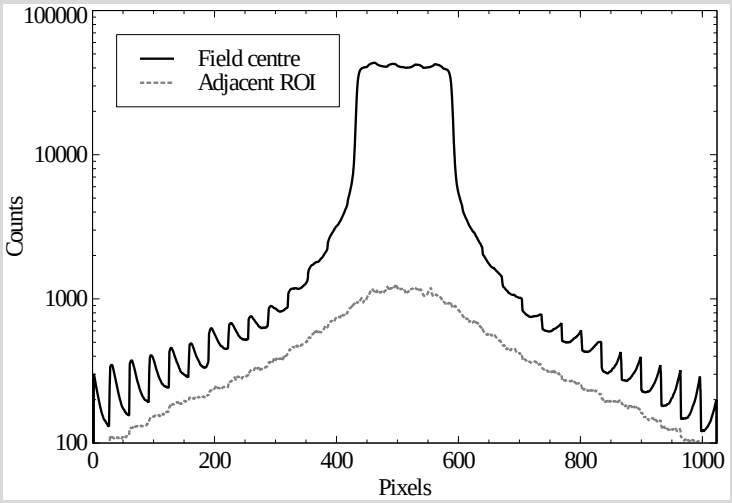

The figure above exemplifies the extent of the stripe artefacts for a 10x10 cm^2 MV field. The (median) line profiles are orientated orthogonal to the stripes on the detector. For the line profile across the MV field centre, the stripes are much more pronounced than for an adjacent 100x1024 ROI. It is also noteworthy how the increased count level extends far beyond the primary MV ROI.

4. perform marker search,

5. back-project marker positions,

6. send marker positions to DKFZ tracking tool.

Image corrections include a gain correction based on a kV flat field and a dead pixel correction. As mentioned in section 3.3.1, no additional offset correction is required. The kV images were analysed with an automated threshold-based marker detection algorithm (Rau et al. 2008). The algorithm initially transforms the input images into binary images based on a dose-dependant threshold. As a second step, connected areas of pixels, i.e. potential marker locations are catalogued. Finally, the candidate locations are fitted with ellipses and further refined according to criteria such as area, major axis length, minor axis length and eccentricity. After successful marker detection, the retrieved marker position on the panel is converted to a 3d position (section 3.3.4) and then the position information is sent to an in-house developed tracking tool (necessary to eventually adapt the MLC shapes). The transfer of position information between MarkerTool and tracking tool was organized as xml-stream over an Ethernet connection.

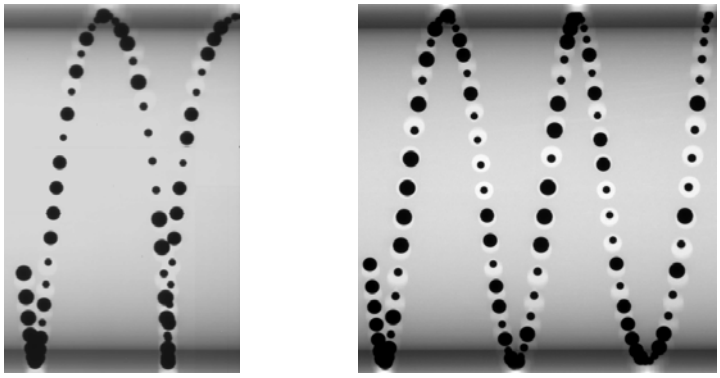

(a) (b)

Figure 3.5 Projection of the helix phantom at gantry angle 0° using (a) our geometry or (b) the standard CBCT geometry. Because the x-ray source is retracted towards the gantry by 13 cm and because the FOV in -y direction is limited by the x-ray source aperture, only parts of the helix are visible.

3.3.4 Geometric cone beam calibration

For conventional CBCT geometries, the use of 'helix' phantoms in geometric calibration has been successfully demonstrated (Pouliot et al. 2005, Gayou & Miften 2007). Helix phantoms are x-ray transparent cylinders with embedded x-ray-opaque ball bearings (BB). Our experimental set-up however, features a kV cone beam that is not centred on the isocenter in longitudinal direction. It was thus necessary to adjust the standard geometric calibration to account for the large number of overlapping projections (figure 3.5) of BBs. The problem also differs from *extended* FOV acquisition, which is not centred on the isocenter in lateral direction. Because the helix phantom is oriented along the longitudinal axis, *e*FOV does not pose a problem for the standard calibration procedure.

As part of the imaging framework described in Section 3.3.3, we have implemented an algorithm that detects projected BBs on the flat-panel image and cross-references these detector positions to the known room-coordinates. This creates a 3x4 projection matrix $\mathbf{P}$ that maps objects from three-dimensional room positions $(x, y, z, 1)$ to two-dimensional detector space $(u_1, u_2, 1)$:

$$\lambda\,(u_1, u_2, 1)^T = \mathbf{P}\;(x, y, z, 1)^T \tag{3.1}$$

Details on the computation of $\mathbf{P}$ are found in Navab et al. (1996). For convenience, the projection matrix was normalized by λ_{iso}, such that $u_1 = p_{14}$ and $u_2 = p_{24}$ for a projection of the isocenter $(0, 0, 0, 1)$. It should be noted that the *quality* of $\mathbf{P}$ depends on the spatial distribution and number of detected BBs. The algorithm requires eight subsequent BBs and its size (large or small) to correctly match the detected BBs with the helix pattern. Due to the overlap of the projections of BBs, it is important to detect at least two unconnected sub-strands of the helix in order to achieve sufficient geometric accuracy in all directions. The x-ray source position $(x_{src}, y_{src}, z_{src})$ can be directly calculated from the projection matrix $\mathbf{P}$ through solving the given set of linear equations (Wiesent et al. 2000):

$$\begin{pmatrix} p_{11} & p_{12} & p_{13} \\ p_{21} & p_{22} & p_{23} \\ p_{31} & p_{32} & p_{33} \end{pmatrix} \begin{pmatrix} x_{src} \\ y_{src} \\ z_{src} \end{pmatrix} = \begin{pmatrix} -p_{14} \\ -p_{24} \\ -p_{34} \end{pmatrix} \tag{3.2}$$

A unique solution exists if the the left sub-matrix of $\mathbf{P}$ has full rank. Comparing the extracted and the true x-ray source position yields a good approximation for the validity of $\mathbf{P}$, especially because it is correlated to the number of detected BBs.

The room positions of markers were then derived by back projecting marker positions from the FPD into three-dimensional space. Naturally, a 2d-to-3d projection can only approximate true 3d data. For the purpose of our study, we have always back projected into isocentric planes parallel to the detector.

3.3.5 Geometric simulation

In order to verify the applicability of a helix-based geometry calibration for our unique in-line geometry, we have simulated a virtual phantom in Matlab. A tabulated list of BB coordinates provided by the helix manufacturer was used to forward-project BBs from a virtual x-ray source located at $x_S = (0, 13.0, -100.0)$ cm onto a virtual flat-panel detector centred around $x_{FPD} = (0, 0, +36.5)$ cm. A point-like x-ray source, point-like BBs, and infinitely small detector elements were assumed to create an *ideal* projection matrix P_{id}. Subsequently, uniformly distributed noise was added to the x-ray source position to account for its finite size. Here, we assumed a maximum source diameter of 0.5 mm. Phantom fabrication imprecisions (Ford et al. 2011) were simulated by adding Gaussian noise to the BB positions. The Gaussian distribution was characterized by a standard deviation of $\sigma = 0.05$ mm and truncated at $3\,\sigma$. We also simulated the effect of a 0.4 mm pixel pitch in our FPD. The simulated BB coordinates and positions on the detector were then combined as described in section 3.3.4 to calculate a simulated projection matrix P_{err} including a combination of all error sources.

In order to quantify the error occurring when detecting 3d positions with a 2d detector, we derived the position of sets of three Calypso® (Varian Medical Systems, Inc.) beacons from planning CT scans for two prostate patients. Using the ideal projection matrix P_{id}, we forward-projected and back-projected the markers individually and then compared the center of gravities. In order to create a larger sample of possible prostate marker positions, we rotated the initial marker coordinates about the longitudinal axis and compared errors. By comparing the length of the centre-of-gravity vector before and after projection, the 3d error was estimated. For the initial marker geometry of patient 1, we simulated the effect of translation on the detection accuracy.

3.3.6 Experimental studies

The main goal of our experimental studies was to characterize the performance of our imaging system in terms of *imaging latency* and *position detection accuracy* with the aid of two motorized motion platforms. Initially, we compared a set of subsequently acquired projection matrices with and without phantom repositioning to estimate the numeric stability of our calibration algorithm and user-induced accuracy errors.

We define the imaging latency Δt as time between the beginning of kV x-ray exposure t_{xray} and the time of arrival of marker position information at the tracking tool $t_{arrival}$:

$$\Delta t = t_{arrival} - t_{xray} \tag{3.3}$$

Using this definition implies that the minimum imaging latency is given by the image acquisition time of 66.6 ms. From the tracking tool point of view, an *effective* latency Δt_{eff} needs to consider not only the lag time of each individual marker position, but also the update frequency f (compare with equation 3 from Poulsen et al. (2010 c):

$$\Delta t_{eff} = \Delta t + \frac{1}{2\,f} \tag{3.4}$$

In this study, measured imaging latencies are presented in terms of equation 3.3. The position detection accuracy Δx_i of each axis i is measured as the difference between the reported marker position and the true, i.e. independently verified marker position:

$$\Delta x_i = x_i^{reported} - x_i^{true} \tag{3.5}$$

In this study, 1D errors are reported unless otherwise noted. For dynamic measurements, the root-mean-square (RMS) detection error $\langle \Delta x_i^{rms} \rangle$ is combined with the phantom error Δx^{ph}, i.e. the estimated error of the true marker position:

$$\langle \Delta x_i \rangle = \sqrt{\langle \Delta x_i^{rms} \rangle^2 + \left(\Delta x^{ph}\right)^2} \tag{3.6}$$

For all experiments, the independently verified marker positions are measured with respect to the isocenter and thus the room laser system. Due to the finite width of the laser beam, this incorporates an error of approx. 0.5 mm.

3.3.6.1 3d phantom

To mimic respiratory marker motion, we employed a 3d motion platform, capable of reproducing sinusoidal trajectories along the longitudinal and/or lateral axis. The platform was placed on top of the linac's patient couch. The motion platform was mounted with a plate of water-equivalent material holding either a single radioopaque steel marker of 3.5 mm diameter or three Calypso (Calypso Medical Technologies, Seattle, WA, USA) beacons (1.8 mm diameter, 8 mm length). The Calypso localization system (Balter et al. 2005) is based on monitoring three radio-frequency transponders (Calypso beacons). Our research version of the Calypso system provides centre-of-gravity position information at a 25 Hz frequency to a sub-mm accuracy.

For all dynamic measurements, the phantom trajectory was limited to the isocentric plane parallel to the detector. For static measurements without phantom motion, vertical positions were also sampled. The phantom provided us with a continuous voltage signal acting as position surrogate, which was sampled every 2.5 ms and used to cross-reference the detected marker positions for all dynamic measurements (accurate to approx. ± 0.2 mm). Static positions were verified with the Calypso system when the three Calypso beacons were used. The Calypso beacons were back-projected individually before the centre of gravity was calculated.

3.3.6.2 4d phantom

A programmable 4d motion platform was used to reproduce a measured patient motion pattern with high precision. It consists of three orthogonally mounted axes which can be controlled individually using inhouse-developed software. A plastic arm supporting the phantom with a spherical radioopaque marker of 3.5 mm diameter reaches to the isocenter. Every 15 ms, the platform provided us with a digital log entry of the actual phantom position (accurate to approx. ± 0.1 mm). The patient motion pattern was of an average amplitude of 8.77 mm, maximum amplitude of 9.61 mm and minimum amplitude of 6.66 mm. The average breathing cycle was 3.37 sec.

3.3.7 Dose measurements

Generally speaking, the higher the imaging dose and subsequent signal-to-noise ratio, the easier it is to correctly identify the marker positions. As with any kV imaging protocol, however, additional doses to the patient need to be considered. We measured the kV imaging dose using a 20 cm RW3 phantom and a PTW Semiflex 0.125 cm^2 ionization chamber. To estimate the dosimetric implications of our system we measured doses for a 2 mAs (121 kVp, 20 ms, 100 mA) and a 0.8 mAs (121 kVp, 20 ms, 40 mA) protocol. The source-to-surface distance was 90 cm. Surface doses were measured at 2 cm depth, central doses at 10 cm depth.

3.4 Results

3.4.1 Projection matrix accuracy

We first measured the stability of the projection matrix by repeatingly acquiring scans of the geometry calibration phantom without moving the phantom or any of the imaging equipment in-between scans. The average x-ray source location as defined in section 3.3.5 was $x_S = (-0.17 \pm 0.03, 12.86 \pm 0.03, -96.81 \pm 0.15)$ cm. When back-projecting the projected isocenter position u_{iso} from one scan using any of the other projection matrices, we observed deviations of $\Delta x \leq 0.05$ mm and $\Delta y \leq 0.04$ mm. Similarly, we measured the user-variability of the projection matrix by having different people position the helix phantom. The average x-ray source location was $x_S = (-0.24 \pm 0.08, 12.86 \pm 0.04, -97.05 \pm 0.20)$ cm. Here, the back-projection error at the isocenter was $\Delta x \leq 0.06\ mm$ and $\Delta y \leq 0.32$ mm.

We then simulated an ideal projection matrix and added artificial error sources as described in section 3.3.5. For the ideal projection matrix P_{id}, equation 3.2 accurately reproduces the source position $x_S^{id} = (0.0, 13.0, -100.00)$ cm. The projection of the isocenter onto the FPD was $u_{iso}^{id} = (0.0, -47.45)$ mm. When adding the three different error sources, P_{err} projects the isocenter onto $u_{iso}^{err} = (-0.01, -47.47)$ mm. The calculation of the source position from P_{err} yields $x_S^{err} = (-0.02, 12.87, -99.05)$ cm. Back-projecting u_{iso}^{id} with P_{err} results in errors of $\Delta x = -0.008$ mm and $\Delta y = 0.013$ mm at the isocenter.

3.4.2 Static accuracy

The accuracy (as defined in equation 3.5) of detecting the centre of gravity for the three Calypso beacons is summarized in table 3.1. During this investigation the phantom remained static with respect to the patient table, and position shifts were achieved by moving the patient table itself. We observed that the electromagnetic pulses emitted by the Calypso system strongly interfere with the flat-panel imager read-out electronics (Rau et al. 2008). Simultaneous position detection with both systems was thus not possible and we decided to perform sequential detection.

For positions within the isocentric plane parallel to the detector (rows 1-4 in table 3.1), the accuracy is better than $\Delta x \leq 0.3$ mm and $\Delta y \leq 0.3$ mm. Because kV and MV beams are not perfectly aligned, motion orthogonal to the detector (i.e. along the vertical axis) leads to deviations in the longitudinal position accuracy (rows 5-6 in table 3.1). We further investigated this loss of 3d information through 2d projection by means of simulations (section 3.4.4).

3.4.3 Dynamic accuracy and latency

The dynamic position accuracy (as defined in equation 3.6) for a longitudinal motion of 19 mm amplitude and approx. 4.5 sec period, performed by the 3d motion platform was measured to be

Table 3.1 Static measurements of the centre of gravity position for three Calypso beacons. Axes are given as specified in figure 3.1. Gantry angle: 0°.

Table position			Calypso			kV images		
x [mm]	x [mm]	z [mm]	x [mm]	y [mm]	z [mm]	x [mm]	y [mm]	z [mm]
0.0	0.0	0.0	0.0	0.0	0.0	-0.02	0.25	0.0
10.0	0.0	0.0	10.0	-0.5	0.0	9.89	-0.19	0.0
0.0	10.0	0.0	0.0	9.5	0.0	-0.01	9.70	0.0
10.0	10.0	0.0	10.5	9.5	0.0	10.26	10.01	0.0
0.0	0.0	20.0	0.0	-0.5	20.5	-0.08	2.38	0.0
0.0	0.0	-10.0	0.0	-0.5	-10.5	0.09	-1.5	0.0

0.20 mm (maximum: 0.30 mm) without MV radiation and 0.23 mm (maximum: 0.32 mm) with a static circular MV field of 5 cm diameter and a dose rate of 300 mu/min. The deviation between measured and true marker positions is shown in figure 3.6 (a).

The imaging latency was measured to be 86.9±1.0 ms for dynamic single marker detection in the absence of MV radiation. In the presence of a circular MV field, the latency was 87.1±0.9 ms. The main contributors to imaging latency were the image acquisition time (66.6 ms), the marker detection algorithm (approx. 6-9 ms) and image post-processing steps such as gain and dead pixel corrections (approx. 5-6 ms). The time for marker search and post-processing does strongly depend on the ROI size. While the marker search for the first frame was performed in a 200x150 pixel ROI, it was then restricted to a 40x40 pixel ROI (depending on previously found marker positions) which saved approx. 5 ms in imaging latency.

When tracking the marker motion with the circular MV field described above, we measured a position detection accuracy of 0.27 mm (maximum: 0.34 mm; figure 3.6 (b)). The imaging latency was measured to be 87.1±0.8 ms. The total system latency (imaging latency + MLC latency) was compensated by using a support vector regression predictor (Krauss et al. 2011). While the distance between marker(s) and field-centre, as measured on our FPD, varies for static MV fields and moving marker(s), it is approximately constant for dynamic MLC tracking.

For the real patient respiratory motion (figure 3.7) performed by our 4d platform we observed a latency of 87.1±0.7 ms and a position accuracy of 0.36 mm (maximum: 0.44 mm).

3.4.4 The loss of 3d information

We derived two sets of marker positions for prostate tumours from real patient data (table 3.2). A simulated rotation of the marker positions about the y-axis (figure 3.8) highlights the interdependence of x, y and z errors. As noted in section 3.4.2, the z coordinate of the marker (for gantry angle 0°) influences the detection accuracy of the x and y axes. For patient 1 this effect results in a detection errors of $\langle \Delta x \rangle = 0.45$ mm (maximum: 0.98 mm) and $\langle \Delta y \rangle = 1.50$ mm (2.66 mm), averaged over all angles of rotation. The average 3d error is 5.04 mm (maximum: 12.22 mm, minimum: 0.53 mm). For patient 2, the centre of gravity of the three markers almost coincides with the isocenter. Here, the rotational errors are $\langle \Delta x \rangle = 0.23$ mm (maximum: 0.41 mm) and $\langle \Delta y \rangle = 0.35$ mm (0.44 mm).

Looking at the effect of translation, we shifted patient 1 by +2.47 mm (x), -6.8 mm (y) and +14.7 mm (z) such that the centre of gravity of the three markers would coincide with the isocenter . In doing so, we observed a reduction from $\Delta y = 2.61$ mm to $\Delta y = 0.02$ mm and small increases from $\Delta x = 0.20$ mm to $\Delta x = 0.34$ mm.

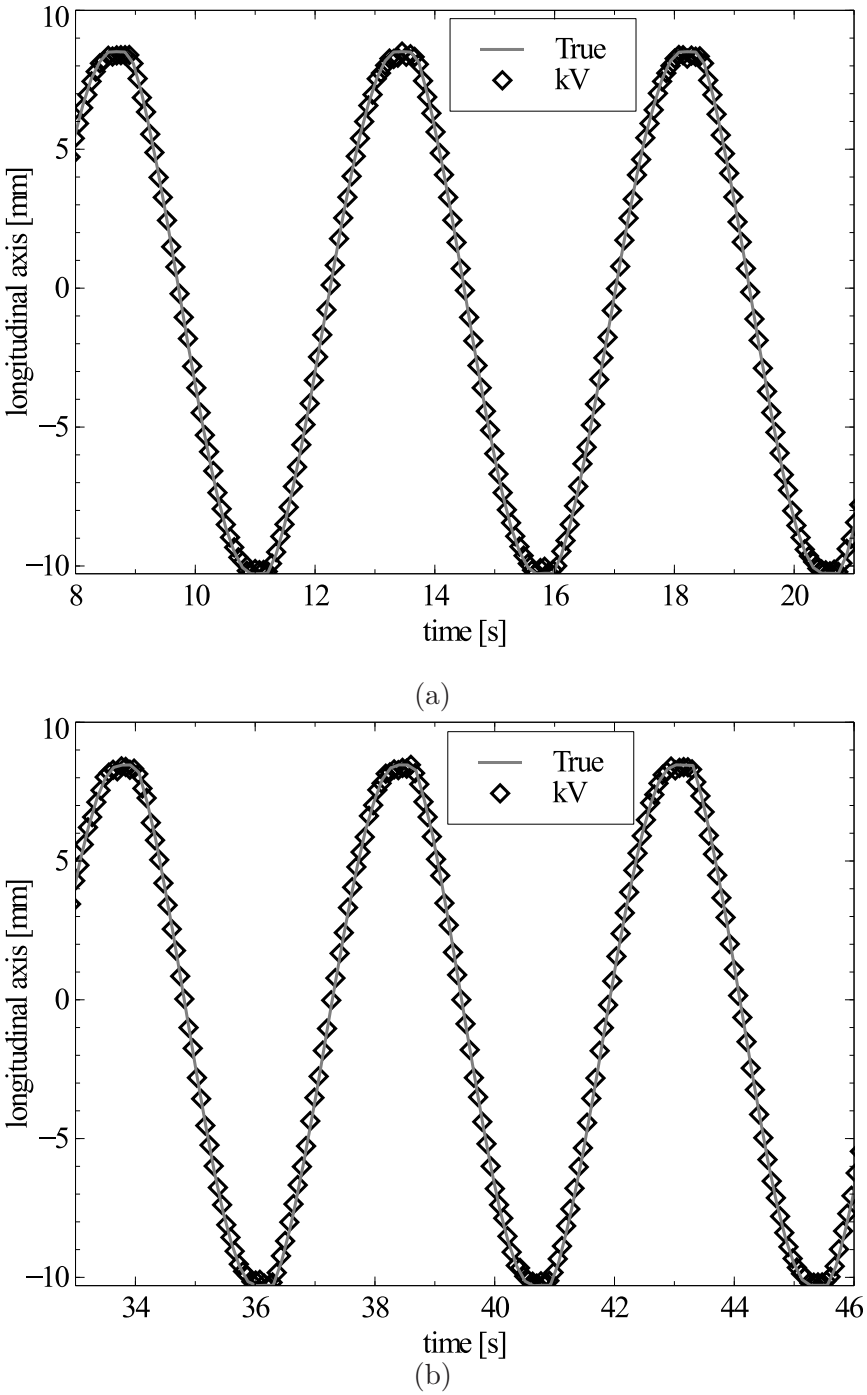

Figure 3.6 Marker positions extracted from kV images versus true marker positions for a sinusoidal motion in longitudinal direction. A static (a) or tracked (b) circular MV field of 5 cm diameter and a dose rate of 300 MU/min was present.

3.4.5 Dose measurements

We measured average dose values of <0.1 mGy per projection for 2 mAs kV images and surface doses below <0.2 mGy. For a low dose 0.8 mAs protocol, average and surface doses amounted to <0.04 mGy and <0.07 mGy respectively. If the system was operated at its theoretical maximum imaging frequency of 7.5 Hz using a high-dose protocol, the average imaging dose would reach 1 Gy after approx. 22 mins.

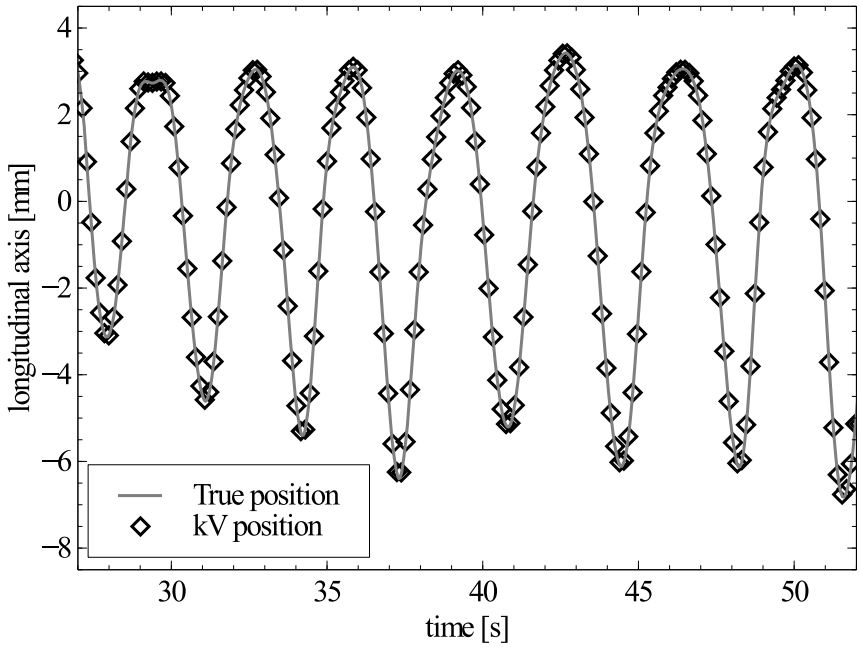

Figure 3.7 Real patient breathing pattern performed on 4d phantom. In order to eliminate any systematic error from the geometric calibration and to highlight the random marker position error (section 3.4.1), we have shifted the detected marker positions by 0.36 mm in -y direction for this dataset.

Table 3.2 Marker positions (M1-M3) derived from real patient data. The positions are absolute positions in the reference frame specified in figure 3.1. The centre-of-gravity is abbreviated as *Cog*.

	Patient 1				Patient 2			
	M1	M2	M3	Cog	M1	M2	M3	Cog
Coordinates	[mm]	[mm]	[mm]	[mm]	[mm]	[mm]	[mm]	[mm]
x	-6.9	8.6	-9.1	-2.47	2.4	9.7	-12.2	-0.03
y	0.8	10.8	8.8	6.8	-10.3	9.7	0.6	0.0
z	-8.0	-17.9	-18.2	-14.7	9.4	-4.0	-5.5	-0.03

3.5 Discussion

Our geometry calibration measurements have demonstrated that user-induced errors such as rotations and translations of the calibration phantom are the main reason for projection matrix inaccuracies. Simulations of other potential error sources of the geometry calibration such as the finite x-ray source size, the position imperfections of the ball bearings, and the detector sampling effect have only minor contributions. The previously introduced helix-based geometry calibration (Pouliot et al. 2005, Gayou & Miften 2007) is thus applicable to our geometry. Further error sources related to the FPD (e.g. roll or reproducibility of panel position from calibration to experiment) have not been simulated. Because only a fraction of the calibration phantom is visible in the FOV, the projection matrix is only valid for that particular region of the FPD. We also observed that the calculation of the source position from the projection matrix can only approximate the true source position due to the limited number of BBs in the FOV.

Due to the short kV pulse time of less than 15 ms, no marker smearing was observed and thus there was no difference between dynamic and static positional accuracy. Between the three cases

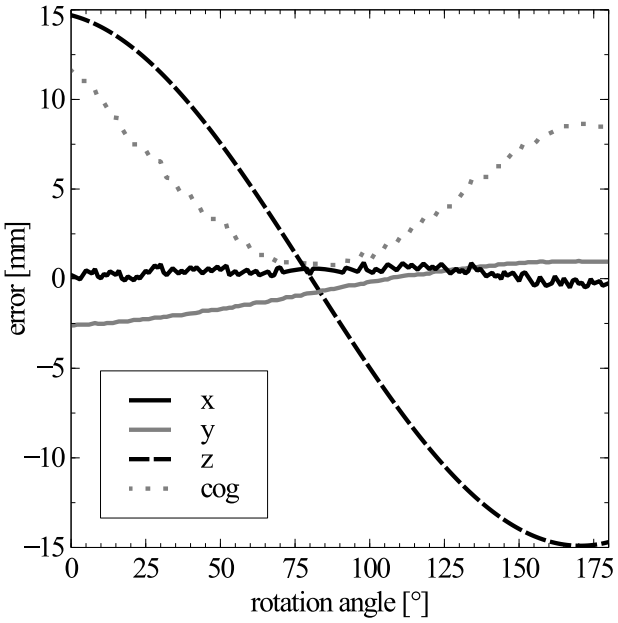

Figure 3.8 Absolute detection errors for the centre-of-gravity ('cog') of three Calypso beacons for prostate patient 1 (table 3.2) assuming different rotation angles of the marker configuration about the y-axis. The 3d or centre-of-gravity error is smaller than the z error for most angles.

of (i) no MV radiation, (ii) a circular and static MV field of 5 cm diameter, and (iii) a circular and tracked MV field of 5 cm diameter, no significant difference in terms of imaging latency or positional accuracy was detected. Neither was any significant difference in the detection of simple sinusoidal motion trajectories or real respiratory motion observed. In any case, imaging latency was better than 88 ms and the RMS longitudinal accuracy better than 0.5 mm for trajectories embedded in the isocentric plane. Imaging latency is a critical factor regarding applications in tracking, gating or any other interventional approach. The reported accuracy errors do not account for possible calibration errors of the room laser system. This can easily add another 0.5 mm to the total inaccuracy.

We observed that the subtraction method described in section 3.3.1 works best for static MV fields, where the MV content can be assumed to be constant. For dynamic tracking fields, the differences in MV content between adjacent frames resulted in a slightly higher noise level.

Naturally, monoscopic 2d projection methods are limited in their ability to achieve 3d positional accuracy. While linac-mounted (Berbeco et al. 2004) or room-mounted (Kilby et al. 2010, Fu & Kuduvalli 2008, Jin et al. 2008, Vinci et al. 2008) stereoscopic imaging systems do not suffer from this limitation, they potentially double the imaging dose and come at the cost of increased technological complexity compared to monoscopic systems. Because of our unique in-line geometry, we monitor the x and y axes (assuming a gantry position of 0°) which are most critical in terms of dose gradients (Nill et al. 2005, Suh et al. 2007). Our measurements have shown that detected marker positions in longitudinal direction depend on their vertical position if the markers are not embedded in an isocentric plane. For a single marker, this effect can amount to a 2.4 mm deviation in longitudinal direction for a 2 cm shift in vertical direction. Our simulations of real patient marker positions show that this negative effect can be compensated for multiple markers by aligning the centre of gravity of the markers with the isocenter. In principle, more accurate 3d positions can be derived from 2d projection by means of probability-based estimation (Poulsen et al. 2010 d, Poulsen et al. 2008, Li et al. 2011).

Measured imaging doses and previously reported dose values (Shirato et al. 2004, Murphy et al. 2007) indicate that overly-frequent x-ray imaging should be avoided to reduce patient exposure. Instead, the system should be used in combination with external markers (e.g. optical or infra-red) to update models that correlate external and internal motion (Cho et al. 2010, Cho et al. 2011).

3.6 Conclusions

We have developed a system that monitors intra-fractional target motion perpendicular to the treatment beam with the aid of radioopaque markers. Our phantom study has demonstrated that the imaging framework is capable of automatically detecting the position of the markers and sending this information to the DKFZ tracking tool at an update rate of 7.14 Hz. Reported positional accuracy and imaging latency indicate that the presented system is suitable for real-time interventional or even adaptive applications.

From our initial experience, further improvements in kV image quality could be achieved by increasing the kV-to-MV signal ratio or enhancing the MV subtraction method. In that context it seems especially interesting to investigate the possible advantage of utilizing a 30 Hz flat-panel detector. With such a device the inherent imaging latency could be reduced by 33.3 ms, thus dramatically increasing the kV-to-MV signal ratio. First experimental results, collected after the completion of this chapter, have suggested that shifting the x-ray source further towards the gantry and rotating the FPD by 90° improves the image quality considerable and lessens the impact of the MV stripe artefact (appendix 3.A).

3.A Further improvements for the in-line geometry

After completion of the experiments described in this chapter, we concluded that a further separation of MV and kV fields on the detector would be desirable to reduce the MV-induced degrading of kV image quality.[1] To achieve this, the kV source was retracted towards the gantry by 36.5 cm (previously 13 cm) and rotated about the x-axis by 15° (previously 0°). The latter step was crucial to achieve the ∼12 cm separation of MV and kV field centres on the FPD (figure 3.9). It required changes to the kV source mounting, as rotations about the x-axis were not feasible with the original hardware.

Having separated the MV and kV fields on the detector in the described manner, we noticed that the MV sync stripes (sidebar 3.3) in the kV ROI are greatly reduced when MV and kV fields are spatially confined to different subpanels of the detector (figure 3.9 (b)). We implemented this by first rotating the FPD 90° about the MV beam axis, and then shifting the FPD in -y direction by 7.5 cm. Our FPD is divided into two subpanels with eight read-out groups of 128x512 pixels. Each read-out group is driven by a single amplifier chip and the two subpanels are electronically independent. This explains why the MV sync stripes, which occur along the gate-line direction, do not cross the subpanel border. Figure 3.10 exemplifies the stripe profiles in a subtracted frame created from two subsequent MV frames (no kV beam was present). As before, the MV stripes are most intense for the primary MV region and show a much reduced intensity (though still very substantial) outside the primary MV field. Importantly, the stripes do not 'propagate' across the subpanel border i.e. into the kV ROI as much as they used to (cf. sidebar 3.3), which lead to further improvements in diagnostic image quality.

[1] The methods described in this section were conceived by the author, and then experimentally realized and tested together with Mr. Eric Wisotzky.

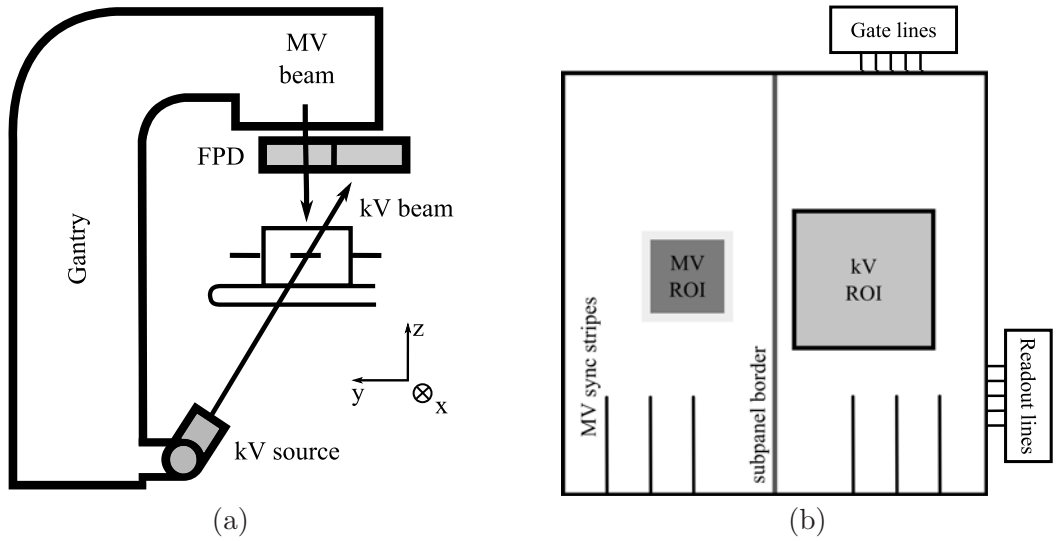

Figure 3.9 (a) Side view for modified experimental set-up. (b) Orientation of ROIs and MV sync stripes in FPD. Compare with figures 3.1 & 3.3.

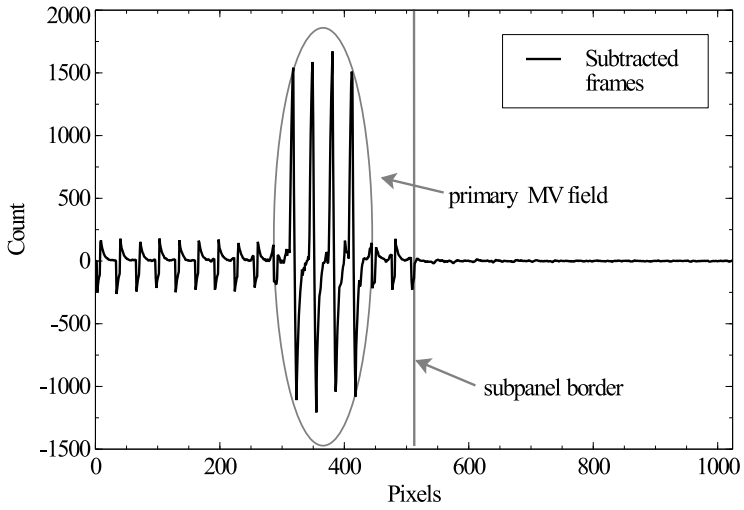

Figure 3.10 Line profile across a subtracted kV-only image. The 10x10 cm^2 MV field is contained in one detector subpanel.

Chapter 4

A Monte Carlo Study of an Improved X-Ray Detector

4.1 Overview

In chapter 3, we have investigated the use of a conventional amorphous-silicon flat-panel detector (FPD) for intra-fractional image guidance in the in-line geometry. In this configuration, the FPD is mounted between the patient and the treatment head, with the front of the FPD facing towards the patient (cf. figure 3.1). By geometrically separating signals from the diagnostic (kV) and treatment (MV) beams, it is possible to monitor the patient and treatment beam at the same time.

In this chapter, we propose an FPD design based on existing technology with a 70% reduced up-stream areal density that is more suited to this new application. We have investigated our FPD model by means of a validated Monte Carlo simulation. Experimentally, simple rectangular fields were used to irradiate through the detector and observe the impact of removing detector components such as the support structure or the phosphor screen on the measured signal. The proposed FPD performs better than the conventional FPD: i) attenuation of the MV beam is decreased by 60%; ii) the MV signal is reduced by 20% for the primary MV field region which can avoid saturation of the FPD; and iii) long range scatter from the MV into the kV region of the detector is greatly reduced.

Publication

This chapter has been published in Fast et al. (2013). Results from this chapter have been presented by the author at the *International Conference on the Use of Computers in Radiation Therapy* (ICCR) in Melbourne, Australia (May 2013).

Acknowledgement

The author would like to thank Giovanni De Crescenzo (TBRRI) for helping with the experiments and the detector modifications. Further thanks to Drs. Peter McGhee and Patrick Rapley (Thunder Bay Regional Health Science Centre) for kindly allowing me to use their AL7 detector and Primus linac, and to Dr. Oleg Rubel (TBRRI) for helpful discussions and supporting the use of his computer cluster.

4.2 Introduction

In modern radiotherapy practise, the precision of treatment delivery has been improved to such an extent, that not only inter-fractional but also intra-fractional organ motion is considered to be vital to the outcome of treatment. This new focus on intra-fractional organ motion requires the use of systems that are able to monitor the internal motion of the patient. Surface-based monitoring systems such as optical or IR cameras are usually cost effective and inherently free of x-ray exposure, but a number of studies have also shown that there can be a differential effect between the internal target and the external surface motion (e.g. Korreman et al. (2008)).

X-ray based imaging systems are able to address this shortcoming. For linear accelerator (linac)-mounted x-ray imaging systems, a number of different imaging geometries are in use or were proposed for intra-fractional imaging: a) megavoltage (MV) imaging using a portal imaging device (Rottmann et al. 2010, Poulsen et al. 2012), b) a set of kilovoltage (kV) x-ray tube and flat-panel detector (FPD) mounted orthogonally to the MV beam (e.g. Poulsen et al. (2010 b)), c) a stereoscopic kV x-ray system mounted symmetrically with respect to the MV beam (Berbeco et al. 2004), and d) the in-line geometry in which the kV x-ray tube is mounted opposite to the treatment head and where the FPD is mounted between treatment head and patient (chapter 3). We would like to refer the reader to section 2.2.1 for a more comprehensive analysis of the advantages and disadvantages of in-line and orthogonal imaging geometry. Most importantly, only the MV and the in-line systems are capable of tracking tumour and organ motion along both axes perpendicular to the treatment beam, the directions that usually feature steep dose gradients. Orthogonal x-ray geometries are limited to a single axis perpendicular to the treatment beam, and to motion parallel to the treatment beam where dose gradients are usually significantly lower. While MV systems have the advantage of being readily deployable (no additional x-ray tube is needed; a portal imager is installed on most modern linacs) and of causing no additional imaging dose, they also suffer from poor image contrast and potentially insufficient field sizes (e.g. small field segments in IMRT treatments). The in-line geometry on the other hand promises diagnostic image quality, while observing both relevant axes of motion. In principle, it is also possible to monitor the entrance fluence and field shape of the treatment beam. This is especially interesting for tracking applications, in which the field aperture can change continuously.

When we first implemented the kV in-line geometry for intra-fractional imaging and tracking (Fast et al. 2012, Krauss et al. 2012), we used a conventional PerkinElmer amorphous-silicon XRD 1640 AN9-ES FPD (without its 1 mm Cu build-up plate) for our experiments (section 3.3). By slightly retracting the x-ray tube towards the gantry and tilting the kV beam in respect to the MV beam, we achieved a geometric separation of kV and MV fields on the detector. The high signal level in the MV region made it necessary to acquire images at almost 15 Hz and use the relatively coarse 8 pF gain setting to avoid detector saturation and subsequent damage to the read-out electronics. Additionally, the kV region of the detector was prone to long range scatter from the MV field resulting in an increased level of background signal on top of the diagnostic image. All these factors made it challenging to detect the target motion, especially for thicker phantoms.

A number of design challenges need to be addressed for any detector used for intra-fractional imaging in the in-line geometry: first, the detector needs to be thin (but also mechanically stable) to reduce filtration of the MV treatment beam spectrum; second, the detector needs to be efficient at detecting keV photons from the imaging beam, impinging on one region-of-interest (ROI) of the detector; third, the detector needs to be relatively inefficient for the MV beam, impinging on another ROI of the detector, to avoid detector saturation; finally, scatter from the MV ROI can overwhelm the signal from the kV imaging beam in the kV ROI and therefore needs to be minimized. An ideal detector would thus allow acquisition of diagnostic-quality kV images and it would also be able to monitor the shape and entrance fluence of the treatment beam. For the latter

requirement, a similar concept exists in the form of a multi-wire transmission ionization chamber which is also placed in the accessory holder of the linac treatment head (Poppe et al. 2006). This concept, however, suffers from a relatively low spatial resolution and is of course not suitable for acquiring diagnostic-quality kV images.

In our study, we investigate the impact of the MV beam on the FPD and vice versa, and look at possible modifications to the detector to improve its performance in this new dual-energy application. We establish a baseline by analysing the response of a conventional FPD to MV radiation for the in-line imaging geometry by means of a full Monte Carlo simulation and experiments. Subsequently, we remove 'non-essential' components from the FPD and discuss the impact on the imaging performance. As a last step, we are suggesting a new, thinner FPD design which is based on existing technology, and is designed to overcome most of the limitations previously detailed. This new detector should allow for improved diagnostic image quality, while at the same time continuously monitoring the MV beam.

4.3 Materials and methods

4.3.1 Flat-panel detector

For the Monte Carlo simulation, two types of FPD base models were chosen: first, a model resembling the AN9 detector of our previous study (Fast et al. 2012) with a Lanex Fast-B phosphor screen and without a Cu build-up plate; second, a model closely resembling the AL7 detector, which was available for experiments in this study. The AL7 detector features a Lanex Fine phosphor screen and a 1 mm Cu build-up layer. The only physical difference between the two detectors is the phosphor screen and the Cu build-up plate. The internal composition of the detector models is summarized in table 4.1. Parameters are based on previously published values from Antonuk et al. (1990), Schach von Wittenau et al. (2002), Parent et al. (2006), Pistrui-Maximean et al. (2006), and Cho et al. (2008), as well as on our own estimates. A schematic drawing of the detector and its orientation in respect to the kV and MV beams is given in figure 4.1.

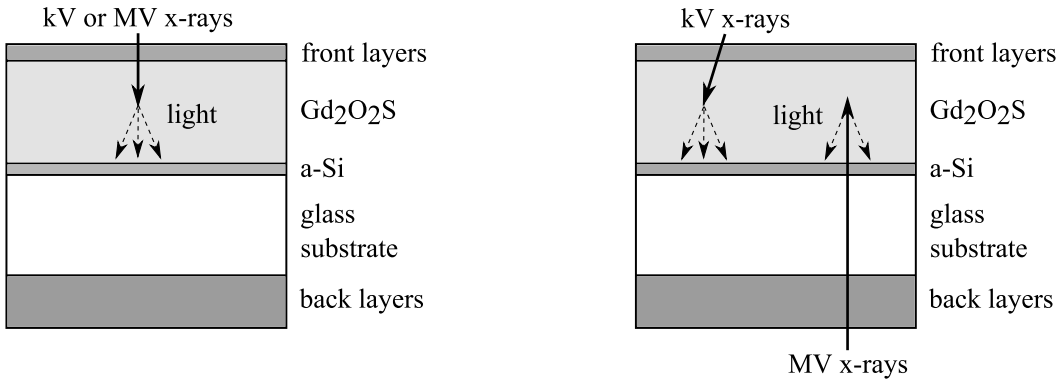

(a) Conventional geometry. (b) In-line geometry.

Figure 4.1 Comparison of (a) conventional x-ray geometry used for kV or MV imaging and (b) the in-line x-ray geometry. For geometry (b) the kV beam is tilted in respect to the MV beam to achieve a geometric separation of kV and MV fields (Fast et al. 2012). Note that the (greatly simplified) detector components are not to scale and that in reality visible light is emitted isotropically. Secondary electrons are not shown.

The Lanex screens are divided into several layers (e.g. Cho et al. (2008)) with the scintillation taking place in a layer of terbium-doped gadolinium oxysulfide $Gd_2O_2S : Tb$. The Tb concentra-

Table 4.1 List of layers in our FPD model and their physical properties. Estimated values for the front and back layers are based on measurements taken of the AL7 detector. Note that our AN9 detector does not have the Cu build-up plate.

Layer	Compounds	Thickness [mm]	Density [$g \cdot cm^{-3}$]
Front plate	Aluminium	0.85	2.7
Gap	Air	5.8	0.001
Build-up	Copper	1.0	8.96
Gap	Air	1.0	0.001
Enclosure	Graphite	0.5	2.2
Lanex Fast-B or Fine screen			
Coating	Acetate	0.01	1.32
Plastic support	Polyethylene	0.178	1.4
Reflective surface	TiO_2	n/a	n/a
Phosphor	$Gd_2O_2S : Tb$	0.36 or 0.09	3.72
Coating	Acetate	0.008	1.32
Sensor	a-Si	0.001	2.33
Glass substrate	Corning1737	1.1	2.54
Supporting material			
Support	Carbon fibre	3.0	1.6
Support	Aluminium	2.0	2.7
Gap	Air	15.1	0.001
Printed-Circuit Board			
Circuits	Copper	0.1	8.96
Substrate	Epoxy, glass	3.5	1.9
Gap	Air	6.8	0.001
Back plate	Aluminium	3.0	2.7

tion is usually smaller than 0.1% and has thus little effect on the x-ray absorption. The phosphor layers have areal densities of 34 $mg \cdot cm^{-2}$ (Lanex Fine) and 133 $mg \cdot cm^{-2}$ (Lanex Fast-B) respectively (El-Mohri et al. 2001). Considering that the phosphor layer is in reality not pure $Gd_2O_2S : Tb$, but a mixture with a polymer binder and air pockets, it is reasonable to assume an effective phosphor packing density of 50% (Liaparinos et al. 2006). This results in a $Gd_2O_2S : Tb$ mass density of 3.72 $g \cdot cm^{-3}$ and a thickness of 90 μm (Lanex Fine) and 360 μm (Lanex Fast-B).

4.3.1.1 Detector configurations.

Starting from our previously described model of the AL7 detector, we have removed selected layers of the FPD to investigate the impact on the imaging performance. Reducing the number of layers and thus the absorption length is the common theme behind most of our derived non-standard detector configurations. Making the detector thinner should not only reduce the absorption of the MV beam, it should also reduce scatter within the panel and scatter onto the patient. The following layer designs were studied:

1. *Standard* AL7 detector: described in detail in table 4.1.
2. *Stripped-down* detector: based on the *standard* detector but without the Al front plate, Al back plate, and Cu build-up plate.
3. *Direct* detector: based on the *standard* detector but without the Al back plate, Lanex screen, Cu build-up plate, and graphite layer.

4. *Notional* detector: based on the *standard* detector but the Al front plate is replaced with carbon fibre, no Al back plate, no printed-circuit board at the back of the detector, slimmed down support structure.

The phosphor screen is removed for the *direct* detector configuration. Consequently, the measured signal only depends on the directly absorbed energy in the a-Si. Because the a-Si layer is only about 1 μm thick, this would usually mean a sharp drop in signal. For the in-line geometry, however, all FPD components that are usually 'down-stream' are now acting as build-up layers for the direct detection. Removing the entire phosphor screen acted as surrogate for removing the phosphor in the MV region only (experimentally this was impossible without damaging the phosphor screen). In a realistic scenario, the phosphor is required in the kV region of the detector in order to obtain good contrast.

The central support structure of the proposed *notional* detector, composed of carbon fibre and aluminium, is reduced to an overall thickness of 2.6 mm. The Al back cover was completely removed. We also assumed that the wires present in the printed circuit-board could in principle be rerouted around the detection area, and removed this layer as well. Additionally, the Al front cover listed in table 4.1 was replaced by carbon fibre. The rationale for choosing the given materials and thicknesses was to minimise x-ray absorption, while at the same time ensuring mechanical stability and protecting the inside of the flat-panel detector from external influences. It should be noted that depending on the detector to MV source distance, only parts of the detection area of the panel would need to be reduced to the given thickness. For example, a distance of 60 cm would require a 'thin' area of approximately 25x25 cm^2.

4.3.2 Monte Carlo simulation

The Monte Carlo simulation was performed using the Geant4 v9.5 toolkit (Agostinelli et al. 2003). Geant4 allows the modelling of primary x-ray interactions, secondary particles such as electrons and positrons, as well as optical photon creation and propagation within one framework. All relevant output parameters of the simulation (e.g. absorbed energy, number of detected optical photons) were scored using the ROOT data analysis framework (Brun & Rademakers 1997). Higher order output parameters such as the modulation transfer function or the detection quantum efficiency were calculated as post-processing steps. The procedure used to validate our Monte Carlo detector model is described in appendix 4.A.

Electromagnetic physics

We used the Livermore electromagnetic physics list and set the minimum range of secondary particles to 0.1 μm (electrons, positrons) and 1 μm (x-rays), effectively establishing a production threshold of 1 keV for all particles in all detector layers. The maximum step length was set to 20-100 μm for the phosphor layer depending on the required precision.

Optical properties

Layers of the detector that were assigned with optical properties are listed in table 4.2. The scintillation spectrum of the terbium-doped gadolinium oxysulfide was taken from Brixner (1987). The spectrum shows distinct peaks at wavelengths of 380 nm, 411 nm, 432 nm, 480 nm, 532 nm (main green peak), and 574 nm, spanning an energy range of 2.06 eV to 3.45 eV. For the Lanex Fast-B screen, we assumed a thin reflective titanium dioxide TiO_2 paint between phosphor layer and plastic support structure. The TiO_2 paint has a reflectivity of approximately 0.88 (Kirkby &

Sloboda 2005). Due to the thinness of the TiO_2 layer, we ignored it for the non-optical part of our simulation. Instead, it was designed as an optical 'ground' surface in Geant4, with angles of reflection following a Lambertian distribution. For the Lanex Fine screen, we omitted the TiO_2 layer (Cho et al. 2008) based on the assumption that optical photons are completely absorbed in the plastic support layer.

For the purpose of this study, we have assumed that optical photons which propagate into the glass substrate are mostly absorbed by the dark carbon fibre layer underneath, and that optical backscatter from the glass substrate can thus be ignored. Consequently, no optical properties were assigned to this layer.

Table 4.2 Optical properties of the different Lanex screen layers and active matrix detector. R denotes the refractive index. The TiO_2 paint was simulated as surface only (zero thickness). Scatter was ignored for the Acetate and a-Si layers.

Layer	R	μ_{abs} [mm]	μ_{sc} [mm]	References
Gd_2O_2S:Tb	2.4‡	0.413†	0.021†	‡Radcliffe et al. (1993),
Acetate	1.48	10	n/a	†Liaparinos et al. (2004),
a-Si	4.6	$\sim$0.0001*	n/a	*Poruba et al. (2004)

4.3.3 Linear accelerator model and x-ray tube spectrum

The 6 MV treatment beam used in our simulation is based on an experimentally validated phase space and a Gaussian-shaped source model which was previously developed for a Primus linac (Siemens) and presented by Tacke et al. (2006). In our study, the broad beam originating from the source model is collimated by means of a virtual collimator by discarding particles that do not lie within the specified field boundaries. Scatter by or leakage through the multi-leaf collimator was not considered. The treatment beam spectrum is sampled into energy bins of 40 keV. A normalized sample spectrum is shown in figure 4.2 (a). The mean primary x-ray energy is 1.668 MeV.

For the simulation of the diagnostic kV beam, we have used a 120 kVp (mean energy: 53 keV) x-ray spectrum previously presented by Boone & Seibert (1997).

4.3.4 Modulation transfer function

The spatial resolution of an x-ray imager is commonly quantified in terms of the modulation transfer function (MTF). Although we are not using the MV treatment beam for patient imaging, the spatial resolution is just as important for us because it describes how accurately the device will be able to monitor the MV beam aperture. Additionally, the MV MTF acts as surrogate parameter for the spatial spreading of absorbed energy from the MV ROI into the kV ROI of the detector.

The system MTF_{sys} of an indirect x-ray detector can be split into several multiplicative components:

$$MTF_{sys}(k) = MTF_{opt}(k) \cdot MTF_{rad}(k) \cdot MTF_{pix}(k). \tag{4.1}$$

Here, k denotes the spatial frequency. $MTF_{rad}(k)$ quantifies the spatial distribution of the secondary radiation in the phosphor layer. The spread of optical photons within the phosphor layer introduces a further source of blurring which is described by $MTF_{opt}(k)$. Later, we will

present results for $\mathrm{MTF}_{\mathrm{sys}}(k)$, which includes the blurring effects of secondary radiation and optical photons. To calculate a *pure* $\mathrm{MTF}_{\mathrm{opt}}(k)$ it would be necessary to simulate the absorption of energy within the phosphor layer along a zero-width beam to compensate for the spatial spread introduced through scatter of x-rays and secondary particles. Finally, $\mathrm{MTF}_{\mathrm{pix}}(k)$ describes the collection of optical photons by a single pixel. For the case of a square pixel aperture, it can be expressed as a function of pixel pitch p and spatial frequency k:

$$MTF_{pix}(k) = sinc(k\,\pi\,p). \tag{4.2}$$

We calculated the MTF based on a method presented by Fujita et al. (1992). However, instead of employing a finite width beam angled with respect to the read-out matrix, we chose to perform the equivalent operation of moving an infinitely narrow pencil beam across the width Δx of a single pixel, starting at the boundary of the pixel. The step size was chosen to be $\Delta x/32$. Individual line spread functions (LSF) were then calculated by collapsing the image along the y axis. By sorting the individual LSFs according to their shift with respect to the pixel boundary, an over-sampled LSF was calculated. Finally, the oversampled LSF was Fourier transformed to determine the MTF.

4.3.5 Detection quantum efficiency

The efficiency with which a phosphor screen transfers input information to output information is commonly described by the detection quantum efficiency (DQE). For our study, the DQE is important for determining how sensitive the different detector configurations will be to the MV spectrum.

As function of the signal-to-noise ratio (SNR), the DQE is defined as:

$$DQE = \left(\frac{SNR_{out}}{SNR_{in}}\right)^2. \tag{4.3}$$

The output $\mathrm{SNR}_{\mathrm{out}}$ may be expressed as function of the pixel area α, the quantum absorption efficiency ϵ of the phosphor screen, the incident x-ray fluence ϕ, and a statistical factor I (Dick & Motz 1981):

$$SNR_{out} = (\alpha\epsilon\phi I)^{1/2}. \tag{4.4}$$

The quantum absorption efficiency ϵ is defined as function of the number of incoming x-rays N_{in}, the number of absorbed x-rays N_{abs}, and the incident x-ray energy E_i:

$$\epsilon(E_i) = \frac{N_{abs}}{N_{in}}(E_i). \tag{4.5}$$

The statistical factor I introduced by Swank (1973) is necessary since x-ray pulses are integrated and not counted on an individual basis. The distribution of detected x-ray pulses is also referred to as pulse-height distribution. Three main components are of significance: first, the incident x-ray energy distribution (XED); second, the absorbed energy distribution (AED); and finally, the optical pulse distribution (OPD). Assuming monoenergetic incident x-rays, the statistical factor can be deduced from AED and OPD alone. The OPD only depends on the phosphor layer (i.e. its optical properties), but not on the other layers in the detector. Since the removal of non-phosphor components of the detector therefore only affects the AED but not the OPD, we have effectively assumed that $\mathrm{I}_{\mathrm{OPD}}$ is constant and limited our calculations to the AED.

The Swank-factor I can be expressed as function of the moments m_j of the pulse-height distribution:

$$I = \frac{m_1^2(E_i)}{m_0(E_i) \cdot m_2(E_i)}. \tag{4.6}$$

For example for the energy-dependent AED(E, E_i), the moments m_j are given as:

$$m_j = \int_0^{E_i} E^j AED(E, E_i) dE. \tag{4.7}$$

Combining the above equations yields the following expression for the detection quantum efficiency (Jaffray et al. 1995):

$$DQE = \epsilon I = \epsilon(E_i) \frac{m_1^2(E_i)}{m_0(E_i) \cdot m_2(E_i)} = \frac{m_1^2(E_i)}{m_2(E_i)}. \tag{4.8}$$

Note that the last step in equation 4.8 is only valid if the AED is normalised to the number of incident x-rays. This allows us to quantify the x-ray absorption noise at a spatial frequency of zero. It therefore ignores the influence of spatial resolution on the DQE and should be seen as the upper limit for the investigated detector model.

4.3.6 Experimental set-up

We used a PerkinElmer XRD 1640 AL7-M flat-panel detector for our experiments. The detector has a minimum integration time of 285 ms resulting in a maximum image acquisition frequency of 3.5 Hz. The detector gain could not be altered and was set to 0.5 pF. Consequently, the linac dose rate had to be reduced to 50 MU/min to avoid detector saturation. The detector was mounted on the treatment head of the linac with a custom-built holder in such a way that the detection area was centred in respect to the MV beam and the front of the detector faced the isocentre. The isocentre to flat-panel front-surface distance was 36.0 cm, meaning that the a-Si detection layer had a distance of ∼63 cm to the MV x-ray source. A Primus linac (Siemens) was used for the experiments. Between 30-75 images were acquired for each detector configuration and field size. The individual images of each series were then offset and dead-pixel corrected. A further correction was necessary to compensate for the synchronization 'stripe' artefacts, which occur when read-out of a row of pixels coincides with a pulse from the linac. A semi-automatic stripe detection was developed to identify the positions of the stripes in the out-of-field regions of the image. Due to the regular nature of the stripes (their occurrence coincides with the pulse rate of the linac), it was possible to then extrapolate stripe positions into the MV field region. Having identified stripe positions in all images, the images were averaged while discarding contributions from the stripes (this is possible because the stripes are in different positions for each image).

4.4 Results

4.4.1 Attenuation of the treatment beam

We have quantified the total attenuation of the treatment beam and the production of secondary particles in the FPD by counting the number of non-interacting primary particles, scattered x-rays, secondary electrons, and secondary positrons in two scoring surfaces located behind the physical

detector. The scoring surfaces were designed to be the same size as the flat-panel detector, and were positioned parallel to the latter at different depths. Results for the *standard*, *stripped-down*, and *notional* detector configurations, as introduced in section 4.3.1.1, are shown in figure 4.2 (b). We assumed a field size of 10x10 cm^2 for all simulations and placed the FPD at a source-to-detector distance of 60 cm.

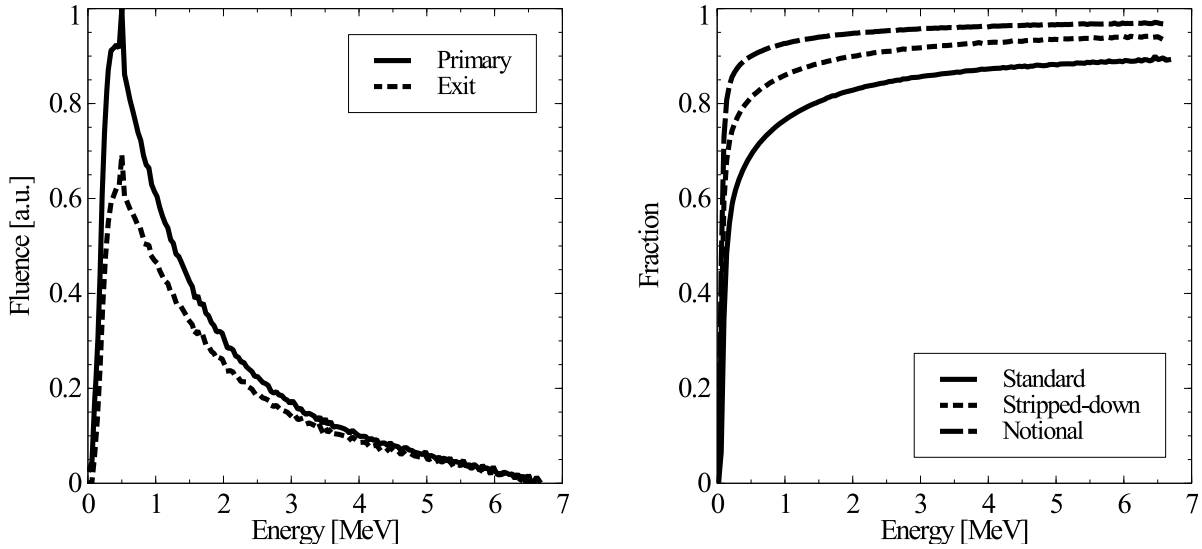

Figure 4.2 (a) Normalised primary fluence of the 6 MV linac spectrum used in this study and the exit spectrum for the *standard* detector. (b) Fraction of non-interacting primary x-rays for the different detector configurations.

The resulting spectra of primary x-rays and secondary particles exiting the FPD are characterized in table 4.3. For the *standard* (AL7) detector configuration, almost a quarter of all primary x-rays interact within the flat-panel detector, leading to a significant hardening of the primary MV beam. Scattered x-rays, and to a lesser degree also secondary electrons, exit the flat-panel in substantial numbers leading to an increased surface dose for the patient and potentially greater dose inhomogeneity. A small number of positrons is also created (less than 0.05% of the number of primary x-rays). When comparing the exit spectrum right behind the flat-panel detector and at a distance of 20 cm (a distance that is assumed to roughly coincide with the surface of the patient), it becomes clear that especially low-energetic secondary particles are scattered away from the patient. The number of secondary x-rays is thus reduced by 40% whereas the number of electrons and positrons is reduced by 20-25%. The AN9 detector used in our previous study (Fast et al. 2012) offers a small improvement over the AL7 detector due to the lack of a Cu build-up plate. For the *stripped-down* and *notional* detector configuration, the number of non-interacting primary x-rays is dramatically boosted, while the number of secondary x-rays falls accordingly. Interestingly, an increase in the number of electrons is observed. This can most likely be explained by the missing Cu build-up and Al front plates, which effectively act as a filter for low-energy electrons.

4.4.2 Imaging performance for the diagnostic kV beam

The quality of the diagnostic kV image acquired with our in-line geometry depends on the superposition of signals originating from (i) keV photons that traversed the patient and interacted in the detector, and (ii) scattered particles from the neighbouring MV ROI that deposit energy in the kV ROI. While the latter effect is discussed in detail in the following sections, we first simu-

Table 4.3 Percentage of primary and secondary particles exiting the different detectors. Each spectrum is additionally characterized by its mean energy ⟨E⟩. The first layer *L0* is adjacent to the FPD, the second layer *L20* is located at a distance of 20 cm from the FPD.

	standard		*AN9*		*stripped-down*		*notional*	
	L0	L20	L0	L20	L0	L20	L0	L20
Non-interacting primary x-rays								
Percentage	76.87	76.76	80.36	80.23	86.11	85.98	92.55	92.41
⟨E⟩ [MeV]	1.80	1.80	1.78	1.78	1.74	1.74	1.71	1.71
Secondary scattered x-rays								
Percentage	14.70	8.883	12.59	7.53	9.352	5.526	5.043	3.026
⟨E⟩ [MeV]	0.73	0.93	0.73	0.93	0.71	0.92	0.71	0.91
Secondary electrons								
Percentage	0.768	0.612	0.833	0.663	0.927	0.744	0.946	0.781
⟨E⟩ [MeV]	1.37	1.45	1.36	1.45	1.33	1.42	1.30	1.39
Secondary positrons								
Percentage	0.036	0.026	0.030	0.022	0.026	0.020	0.024	0.019
⟨E⟩ [MeV]	1.60	1.69	1.57	1.67	1.53	1.64	1.52	1.62

lated the difference in terms of kV image quality between our *notional* detector and the *standard* detector (with its copper build-up plate removed).

For the spatial resolution (Figure 4.3 (a)), we observed a slight increase in MTF for all spatial frequencies for our *notional* detector. Replacing the aluminium front plate of the *standard* detector with carbon fibre yielded MTF curves (data not shown) almost exactly located between the respective MTF_{rad} and MTF_{sys} curves shown in Figure 4.3 (a). This indicates that the difference in front plate material and the difference in back-scatter environment are equally responsible for the increase in the spatial resolution of the *notional* detector.

Figure 4.3 (b) shows the detection quantum efficiency (equation 4.8) for monoenergetic x-ray beams of energies varied in 5 keV steps between 10 keV and 140 keV. Interestingly, the DQE depends solely on the choice of material for the front plate for energies below the K-edge of gadolinium (50.2 keV). Below 30 keV, the reduced absorption of x-rays in the carbon fibre front plate results in dramatically higher DQE-values for the *notional* detector. Above the K-edge energy, the DQE is largely independent from the front plate material and instead depends on the back-scatter from support components of the detector behind the phosphor layer. Due to the reduced down-stream areal density of the *notional* detector compared to the *standard* detector, a slight reduction in DQE in the 60-140 keV energy window can be observed.

4.4.3 Radial dose deposition for a pencil beam

Scatter within the flat-panel detector leads to a spreading of absorbed MV dose. We analysed the radial dose deposition profile in the phosphor layer for our 6 MV pencil beam. Radial profiles are a convenient simplification of point-spread-functions if radial symmetry can be assumed. The beam was centred with respect to a 21x21 cm^2 detector, and the detector was divided into equidistant radial bins of 0.05 mm thickness during data post-processing. All events which were scored at a distance of more than 10 cm from the centre of the detector were discarded. A total of $1.5 \cdot 10^8$ primary particles was used for each detector configuration. Because of the relatively short absorption length of the phosphor screen for optical photons, we assume that optical spread only contributes signal on the sub-mm length scale and therefore focus on the absorbed energy here. The effect of optical photon spread is discussed in section 4.4.4.

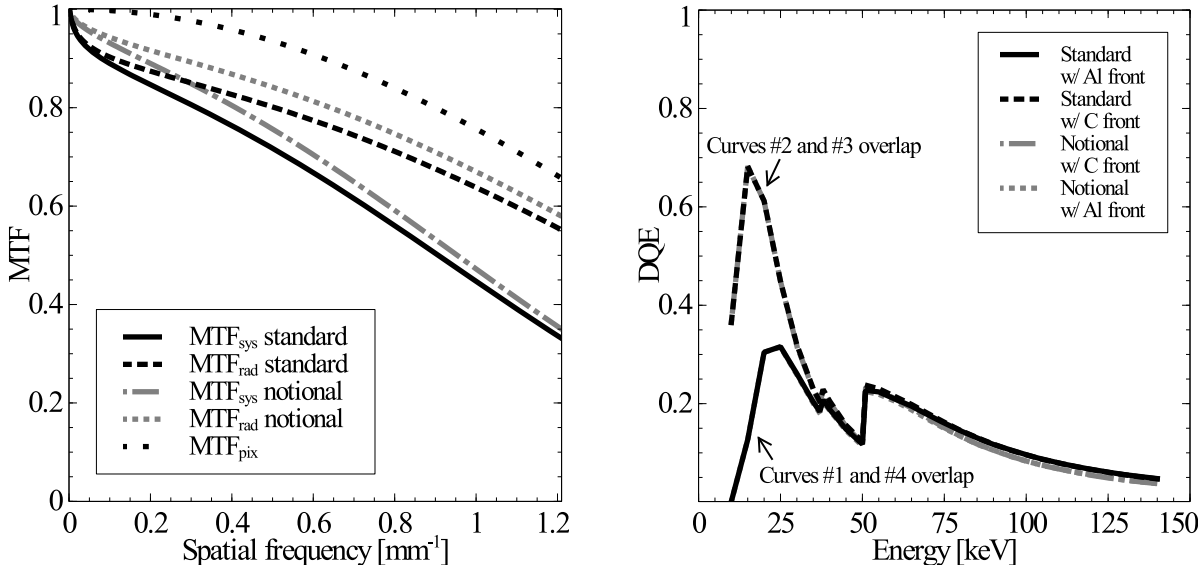

Figure 4.3 Image quality parameters for the kV beam: (a) Modulation transfer functions and (b) detection quantum efficiency. For the DQE, carbon fibre (C) and aluminium (Al) front plates have been simulated for both detectors. Note that the copper build-up plate was removed from the *standard* detector for these simulations.

Figure 4.4 shows the absorbed dose within the phosphor layer as function of the radius for our different detector configurations. The *standard not-rotated (n.r.)* configuration denotes the conventional imaging configuration, in which the front of the flat-panel is facing the MV beam. Interestingly, the total absorbed energy of the *standard (n.r.)* detector is reduced by 2% compared to the *standard* detector, whereas the maximum value (in the central bin) is increased by 5%. This suggests that the twice as high areal density of the up-stream layers leads to a broadening of the dose deposition profile for the *standard* configuration. For both configurations, less than 0.1% of the energy is absorbed outside the 1 cm radius. When comparing figure 4.4 (a) to radial dose profiles for a 9 MeV beam as presented by Schach von Wittenau et al. (2002), it becomes clear that the 'plateau' region produced by the absorption of secondary electrons is much less pronounced for our beam. This is most likely due to the lower CSDA range of the electrons produced by the 6 MeV beam. Figure 4.4 (b) exemplifies the influence of back-scatter on the dose deposition for the *standard (n.r.)* detector. When discarding particles back scattered from down-stream detector layers into the phosphor layer, the total absorbed energy is reduced by a third, and the maximum value by 10%. Most of the relative back-scatter contribution is thus occurring for radial distances higher than 0.5 cm. For the *stripped-down* and *notional* detectors, the areal density of the up-stream panel components is reduced by 30% and 70% respectively, compared to the *standard* detector. Figures 4.4 (c) and (d) show that the radial dose deposition profiles narrow down as expected. The reduced number (and also thickness in the case of the *notional* detector) of up-stream build-up layers, decreases secondary electron production and thus total absorbed energy by 17% and 24% respectively. At the same time, the reduction in radial spread results in an increase of maximum absorbed energy of 2% and 16% respectively.

4.4.4 Modulation transfer function

For the radial dose profiles, we have already observed how the different up-stream layers and areal densities influence the spatial spreading of absorbed dose within the phosphor layer. A further blurring of the effective measured signal of any indirect x-ray detector is introduced through the

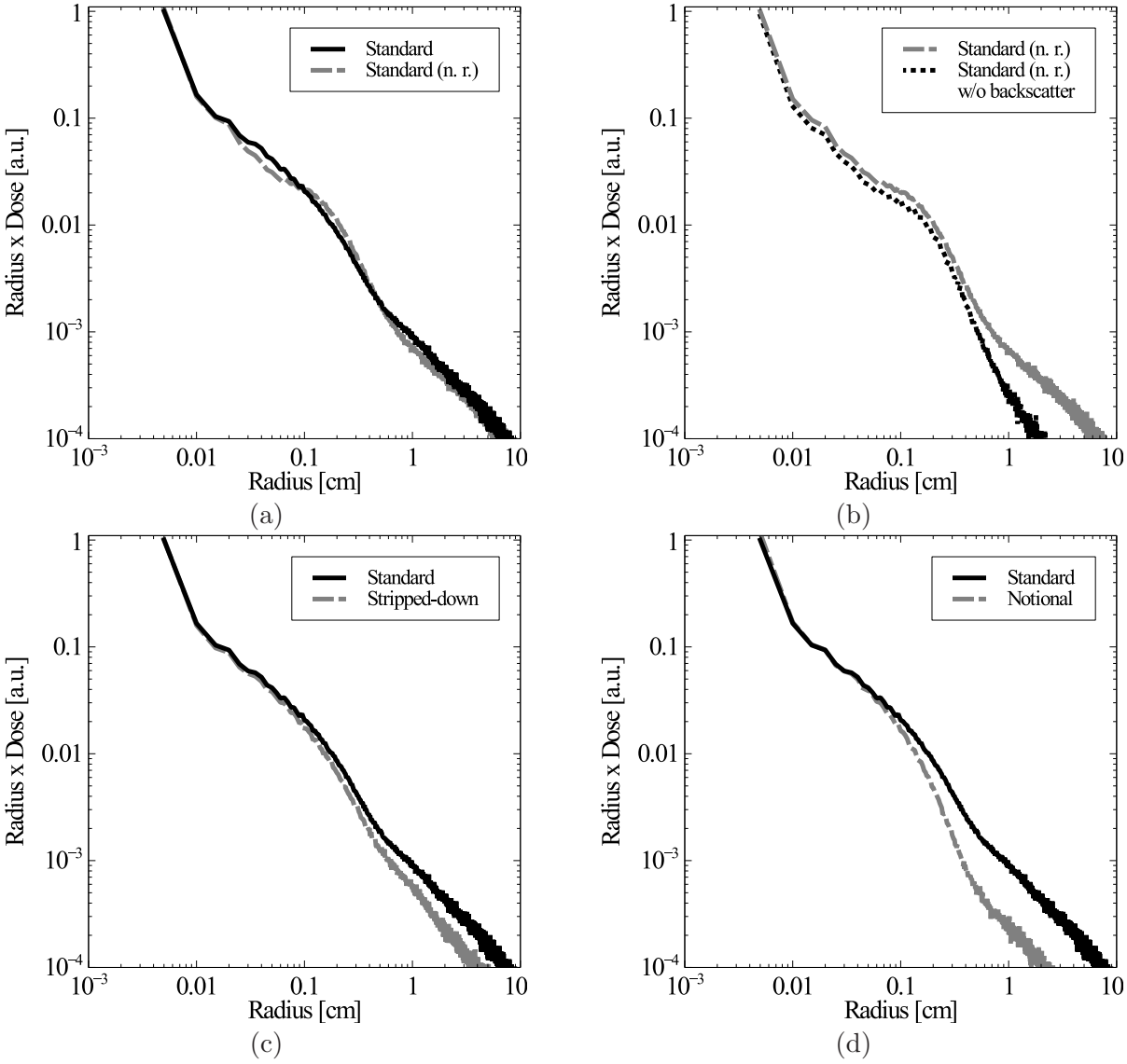

Figure 4.4 Dose deposition as function of radius for a pencil beam normally incident on the centre of the FPD. All curves are normalized to the maximum value of the *standard* configuration. The conventional detector geometry is abbreviated as 'not rotated' (n.r.).

propagation and scattering of optical photons. Optical photons are created at different depth levels in the phosphor which leads to different path lengths depending on the initial depth of interaction. Additionally, the Acetate layer (table 4.2) between the phosphor and a-Si matrix effectively acts as an optical filter.

Our initial analysis of the oversampled line-spread functions (LSF) showed a widening of the full-width at half maximum (FWHM) by approximately 0.5 mm between the secondary radiation LSF_{rad} and the system LSF_{sys}. This additional spread through optical processes is also reflected in the MTF. Figure 4.5 (a) shows the MTF for the *standard* and the *standard not-rotated (n.r.)* detector configuration. The characteristic low-frequency drop is clearly visible and is discussed in more detail in appendix 4.A. Given a pixel pitch of 400 μm, the contribution of MTF_{pix} towards MTF_{sys} becomes more and more important for higher spatial frequencies. Interestingly, the different up-stream detector compositions and the different back-scatter environments cancel each other out and lead to similar MTF_{rad} curves in the phosphor layer. This was to be expected from the similar radial profiles discussed previously. For the *standard* detector, we have removed

back-scatter from the simulation, hence mainly eliminating scatter from the copper layer back into the phosphor, to quantify the effect of back-scatter on the MTF. For the 50% (20%) MTF_{rad} for example, we see a reduction from 0.35 (1.3) mm^{-1} to 0.25 (1.15) mm^{-1} through back-scatter alone.

Figure 4.5 (b) shows that the large reduction of back-scatter as well as the decrease in up-stream areal density leads to a substantial increase in MTF for the *notional* detector compared to the *standard* detector. For the 50% (20%) MTF_{sys}, an increase from 0.175 (0.75) mm^{-1} to 0.405 (1.05) mm^{-1} can be observed.

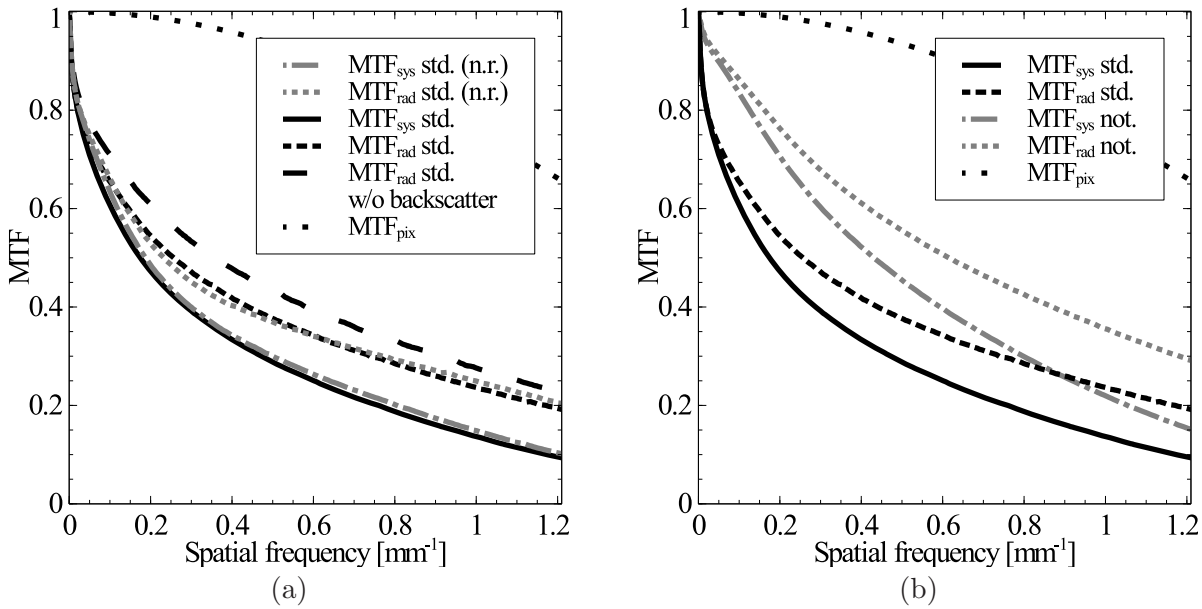

Figure 4.5 Modulation transfer functions. The conventional detector geometry is abbreviated as 'not rotated' (n.r.), the *standard* detector as std., and the notional detector as not. MTF_{pix} (equation 4.2) is identical for all detectors.

4.4.5 Detection quantum efficiency

In order to quantify and characterize the energy response of our different detector configurations, we have analyzed the average deposited energy per incident x-ray, the zero-frequency DQE (equation 4.8), and the statistical factor (equation 4.6) derived from the absorbed energy distribution. We used a monoenergetic pencil beam normally incident on the centre of the detector with 10^6 particles for each energy step. The primary beam energy was varied between 20 keV and 10 MeV.

When comparing the different DQE curves (figure 4.6 (a)), it becomes clear that all detector configurations are relatively inefficient at energies below 100 keV. This is due to the numerous up-stream layers, which filter low-keV primary and secondary particles. As expected, the *standard not-rotated (n.r.)* configuration without the Cu build-up plate comes closest to the performance of a detector optimized for keV energies.

For the in-line detector configurations, it is especially interesting to contrast the behaviour at energies below 100 keV and above 1 MeV. The *notional* detector for example has the smallest up-stream areal density and consequently has a higher DQE below 100 keV due to the comparatively small photoelectric absorption in the up-stream layers. For energies above 1 MeV, Compton forward-scattering and pair production cause a decrease in DQE compared to the other detector configurations. The average deposited energy per incident x-ray (figure 4.6 (b)) shows a similar trend to the DQE and highlights that the *standard* detector is much more efficient at absorbing

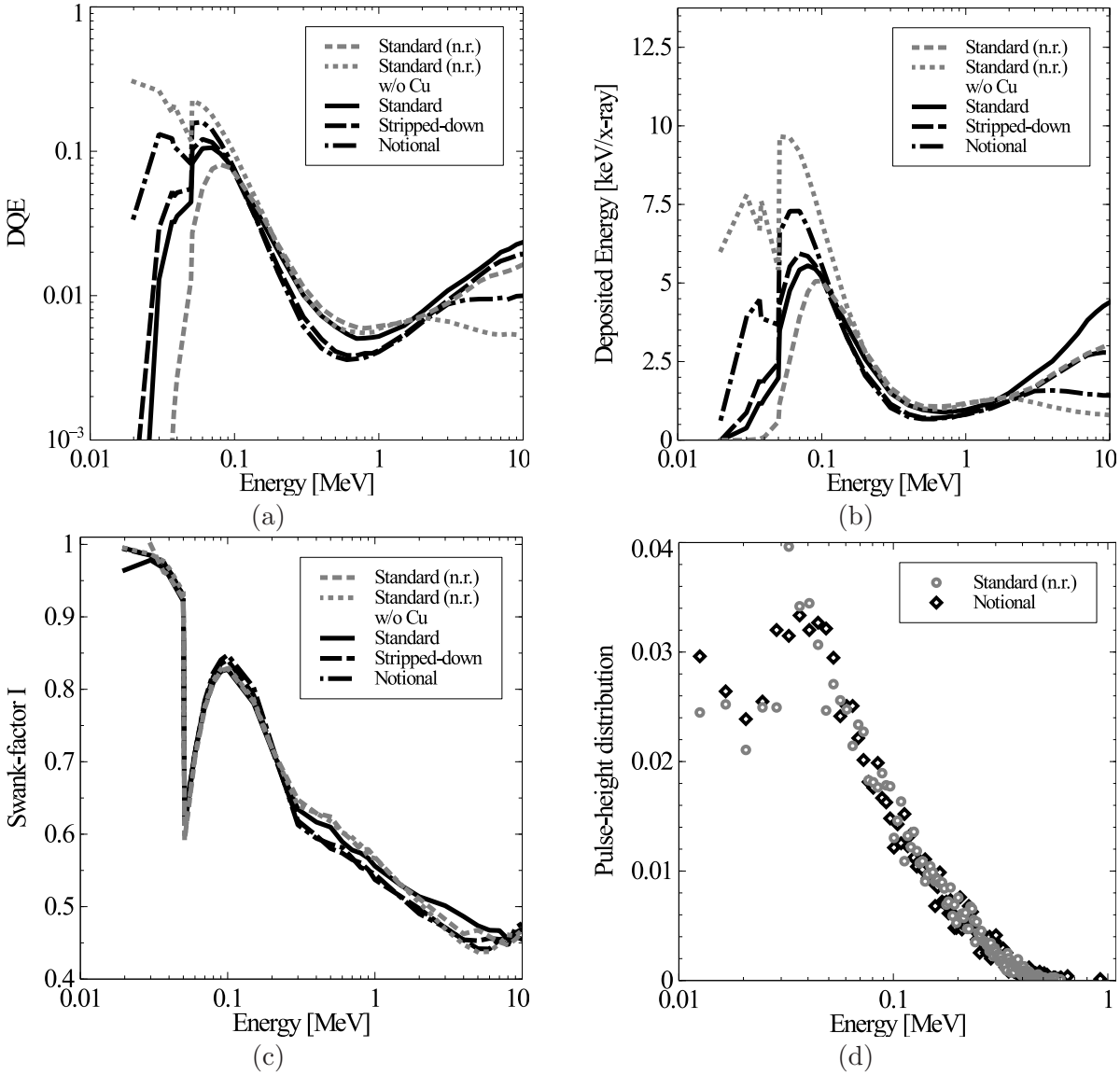

Figure 4.6 (a) Detection quantum efficiency. (b) Deposited energy per incident x-ray. (c) Statistical Swank-factor I. (d) Normalized absorbed energy distributions (AED) for an incident x-ray energy of 1 MeV. The conventional detector geometry is abbreviated as 'not rotated' (n.r.).

x-rays with energies above 2 MeV. For the in-line geometry, in which we try to minimize x-ray absorption and MV-induced detector signal, the higher response of the *standard* detector is of course unwanted.

The statistical factor (figure 4.6 (c)) is well above 0.9 for energies below the K-shell energy of gadolinium (50.2 keV) for all detector configurations, reflecting a narrow confinement of the respective pulse-height distributions. For energies at and above the K-shell energy, a characteristic drop and subsequent recovery of the Swank-factor can be observed. This is due to the emission, propagation and escape of K-fluorescence photons above 50.2 keV (Liaparinos & Kandarakis 2011). Well above 50.2 keV and towards 1 MeV, Compton scattering becomes the main interaction, leading to more widely spread pulse-height distributions (e.g. figure 4.6 (d)), and consequently lower statistical factors for all detectors. For megavoltage energies, the variance of the pulse-height distributions increases further due to the larger electron range. At even higher energies towards 10 MeV and beyond (the latter is not shown), an increase of the statistical factor can be

observed. A detailed explanation of the effects leading to this rise can be found in Jaffray et al. (1995). Interestingly, the relatively low Swank-factor of the *notional* and *stripped-down* detector compared to the *standard* detector, reflects the lower DQE values observed in figure 4.6 (a).

4.4.6 Direct detection

Due to the low read-out frequency of the AL7 detector, a high dose rate setting, as used in therapeutic mode, immediately causes detector saturation for the *standard* and *stripped-down* detector. For the *direct* detector, however, the low direct conversion efficiency allowed us to use both the low (50 MU/min) and the high (300 MU/min) dose rate setting. We observed that independent of field size, the decrease in signal measured by the *direct* detector, when going from the high to the low dose rate setting, equates to a factor of 6 within 1% for the primary MV field region.

When comparing the measured signal of the *direct* detector to the *stripped-down* detector for a central ROI of 41x41 pixels at the low dose rate setting, we observed a decrease in signal by a factor of 5.2±0.1 (10x10 cm^2 MV field, figure 4.7 (a)) and 5.8±0.1 (5x5 cm^2), respectively. Deviations between the measured signals at different field sizes arise from output-scatter factors of the linac and possibly non-linear responses of the *direct* detector at very low signal levels. In order to compare this experimental result with our Monte Carlo simulation, we have assumed that the average energy necessary for creating an electron-hole-pair (EHP) in the semiconductor must be three times higher than the a-Si gap energy (Rowlands 2002) of 1.9 eV. We then divided the number of EHPs by 2 to calculate an equivalent number of optical photons, which we could compare to the number of optical photons originating from the phosphor layer and detected by the a-Si matrix. With our Monte Carlo simulation, we calculated a factor of 6.0±0.2 in signal difference between the two panel configurations when assuming a light yield of 60000 photons/MeV (Eijk 2002). Given the uncertainty in light yield and our simplistic model of the a-Si matrix layer, experimental results and Monte Carlo simulation are in reasonable agreement.

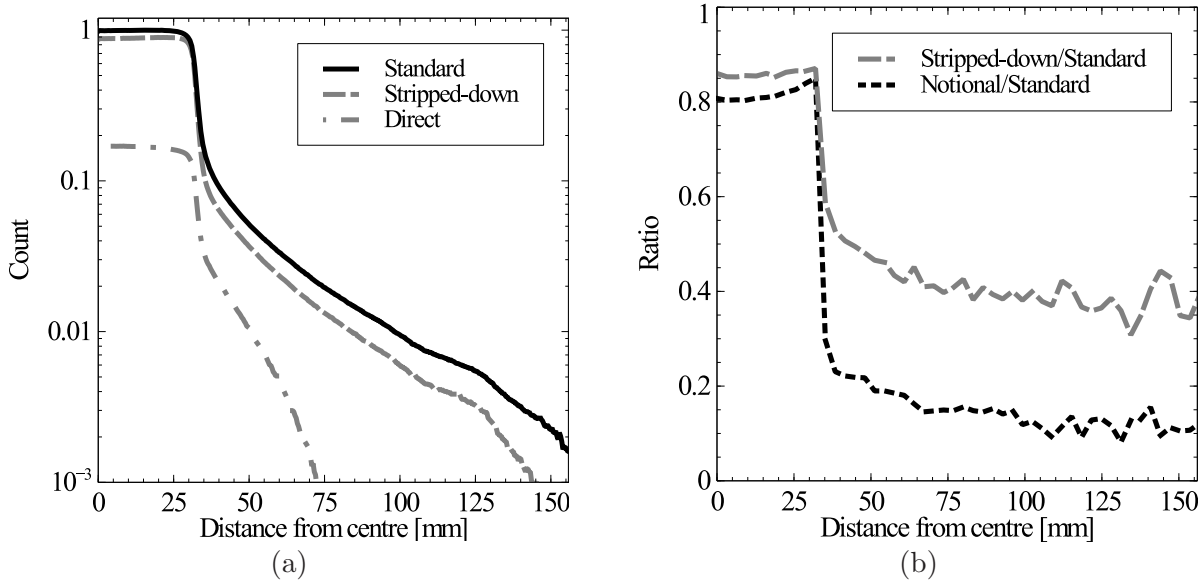

Figure 4.7 (a) Experimentally determined horizontal profiles. Offset, dead pixel and stripe corrections were applied before creating an average image. (b) Ratios of horizontal profiles from Monte Carlo simulation. All data is derived with 10x10 cm^2 MV fields.

4.4.7 Dose deposition profiles

The differences in dose deposition when comparing the different detectors are best visualized by looking at profiles through the experimentally acquired images (figure 4.7 (a)). For the primary field region, the *stripped-down* detector measures a signal reduced by a factor of 0.88±0.01 compared to the *standard* detector. Our Monte Carlo simulation yields a factor of 0.85±0.02 for the same configurations. It can also be observed that the ratio of signals is not constant along the horizontal axis (figure 4.7 (b)). While the *notional* detector sees a reduction of signal by a factor of 0.80±0.01 for the primary field region, the signal is dramatically reduced by more than 80% at distances larger than 1 cm from the primary field edge. Interestingly, the reduction of up-stream areal density of the *notional* detector is also noticeable in a stronger 'cupping' of the beam profile originating from the flattening-filter. This effect is less pronounced for the *standard* detector, because the beam profile is smeared out by lateral scatter in the up-stream detector layers.

4.5 Discussion

Our proposed *notional* detector design is based on existing detector technology (a conventional a-Si matrix array, glass substrate and phosphor screen are used), however it features a slimmed-down support structure. The up-stream areal density at the 'back' of the detector is decreased by 70% compared to the *standard* detector, reducing the filtration of keV photons from the treatment beam (an objective contrary to current detector designs) and also decreasing the number of MeV photons in Compton or pair production interactions. At the 'front' of the flat-panel, the copper build-up plate traditionally used for MV imaging is omitted to avoid scatter from the Cu plate back into the phosphor screen and onto the patient. Omitting the Cu plate also improves the sensitivity of the detector for keV photons used in the diagnostic kV beam. The front plate is made from carbon fibre instead of aluminium to reduce absorption and scatter within the front plate of both the MV and kV beam.

When comparing our *notional* detector with our previously used AL9 detector (Fast et al. 2012), the fraction of non-interacting primary x-rays increases sharply from 80% to 92%. At the same time, the fraction of scattered x-rays arriving at the patient surface is reduced from 7.5% to 3%. Yang et al. (2004) have reported on the contamination of the Primus' treatment beam with electrons arising from several beam path components such as the flattening filter. They observed a relative contribution of approximately 0.07% for electrons from the treatment head, with an average electron energy of 1.3 MeV for the 6 MV beam. For our notional detector, the electron contamination originating from x-ray interactions in the detector is 0.78% with an average electron energy of 1.4 MeV at a 20 cm distance from the flat-panel. While the contaminating electrons (and low-energy scattered x-rays) coming from the treatment head should be mostly filtered by the flat-panel detector, the electron and x-ray contamination originating in the flat-panel may cause additional surface dose. This effect, however, might be partly compensated by the filtration of low-keV x-rays in the flat-panel detector. Further studies are necessary to determine how treatment plan quality is influenced by the changes in treatment beam spectrum introduced through the flat-panel detector.

Our analysis of the zero-frequency DQE and average deposited energy per incident x-ray has revealed that the *notional* detector is a lot less sensitive for MeV photons compared to the *standard* detector. At the same time, the reduced up-stream areal density means that secondary electrons with energies below 100 keV are less likely to be reabsorbed before reaching the phosphor screen. This results in a higher DQE for keV photons from the treatment beam. For the kV imaging beam, we have observed only small differences in DQE between the two detectors in the diagnostic energy window (30-140 keV).

The issue of scatter from the MV ROI into the neighbouring kV ROI is also mitigated by reducing the up-stream areal density. For the radial dose deposition profile of a pencil beam, we have observed that 99.9% of the dose is deposited within a radius of 4 mm and 9 mm for the *notional* and *standard* detectors respectively. Optical spreading introduces a further blur of the order of 0.5 mm for both detectors. This improvement in radial dose confinement for the *notional* detector is also reflected in the spatial resolution: the 50% MTF_{sys}, for example, more than doubles. For a simple 10x10 cm^2 MV field, we could show that the signal of the *notional* detector is reduced by 20% compared to the *standard* detector for the primary field region and by more than 80% when looking at distances greater than 1 cm from the field edge.

We also explored the possibility of using a direct detection configuration for the MV ROI of the detector. Experimentally, we achieved this by removing the phosphor screen and graphite layer. An ideal solution would be one which temporarily disables photon propagation from the phosphor screen to the a-Si matrix. Such a solution would allow the use of the same flat-panel for conventional applications such as kV CBCT. Gustafsson et al. (2011) have suggested a mechanical shutter or an electrically switchable optical layer between the a-Si matrix and the phosphor screen, which would block optical photons from being detected when desired. In our experiments, we have observed a direct to indirect signal ratio of one to six. This means that the direct signal is higher for the in-line geometry than for the conventional imaging geometry, due to the higher up-stream areal density. It also means that the direct signal is still sufficiently high to monitor the treatment beam during therapy while at the same time avoiding detector saturation.

4.6 Conclusion and outlook

In this study, we proposed a *notional* flat-panel x-ray detector that is well-suited for use with our in-line geometry. This *notional* detector is relatively insensitive to the MV treatment beam radiation, while at the same time maintaining a similar sensitivity for the kV imaging beam. Scatter of secondary particles within the detector and scatter of secondary x-rays onto the patient, as well as filtration of the treatment beam is sharply reduced compared to the *standard* detector. Future studies should investigate how the post-FPD treatment beam spectrum influences the treatment beam quality.

4.A Validation of Monte Carlo simulation

We validated our Monte Carlo detector model by reproducing experimental and simulation results that have previously been published in the literature. Importantly, we validated both key physical processes: (i) x-ray and secondary particle transport and absorption by looking at the absorbed energy per incident x-ray and detection quantum efficiency (DQE), and (ii) optical photon propagation by evaluating the modulation transfer function (MTF).

For the average deposited energy per incident photon and DQE (equation 4.8), we remodelled a detector layout presented by Schach von Wittenau et al. (2002). Their detector is similar to ours, except that they assumed a slightly smaller thickness of the phosphor layer (84 μm instead of 90 μm) and a slightly larger density (4.25 $g \cdot cm^{-3}$ instead of 3.72 $g \cdot cm^{-3}$). Although used for MV radiation, no Cu build-up plate was present in their study. Small differences are also to be found in the support structure. Crucially, their 2002 Monte Carlo simulation is based on MCNP4C (Briesmeister 2000) and not Geant4 v9.5. Figure 4.8 shows that there is excellent agreement between our result and their study for a wide energy range. A small discrepancy of below 5% can be observed for the deposited energy below 50 keV. An explanation for this small difference is either a possible difference in the composition of the glass substrate, or more likely

general differences between the different Monte Carlo tools in terms of cross section data, energy tallying, multiple-scatter model etc. These differences are comprehensively discussed by Yoriyaz et al. (2009).

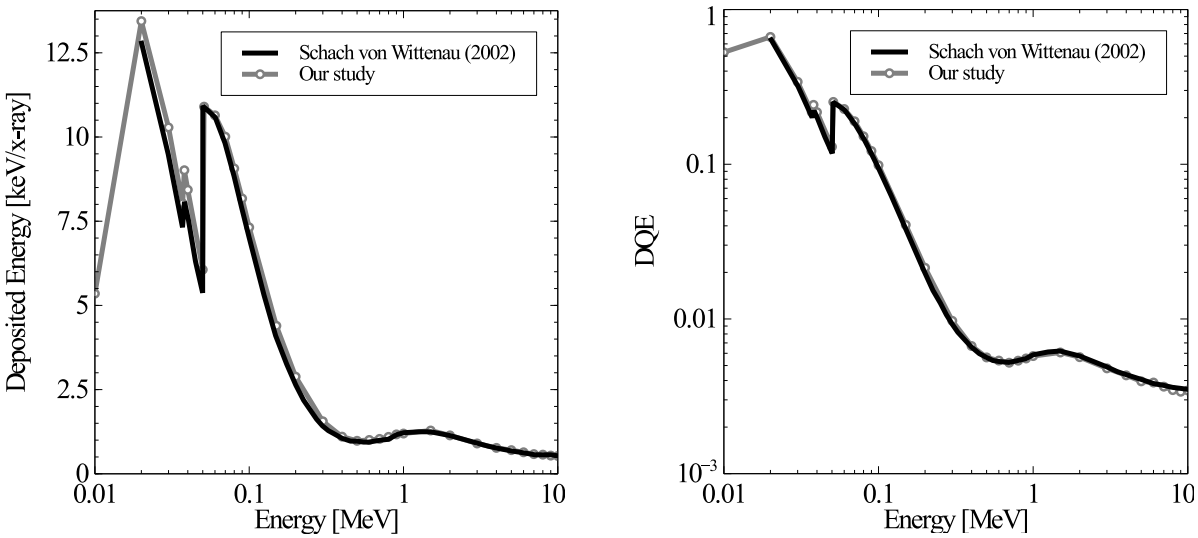

(a) (b)

Figure 4.8 (a) Deposited energy per incident x-ray and (b) detection quantum efficiency for the notional detector presented by Schach von Wittenau et al. (2002). Note the K-shell edges of barium (37.4 keV) and gadolinium (50.2 keV).

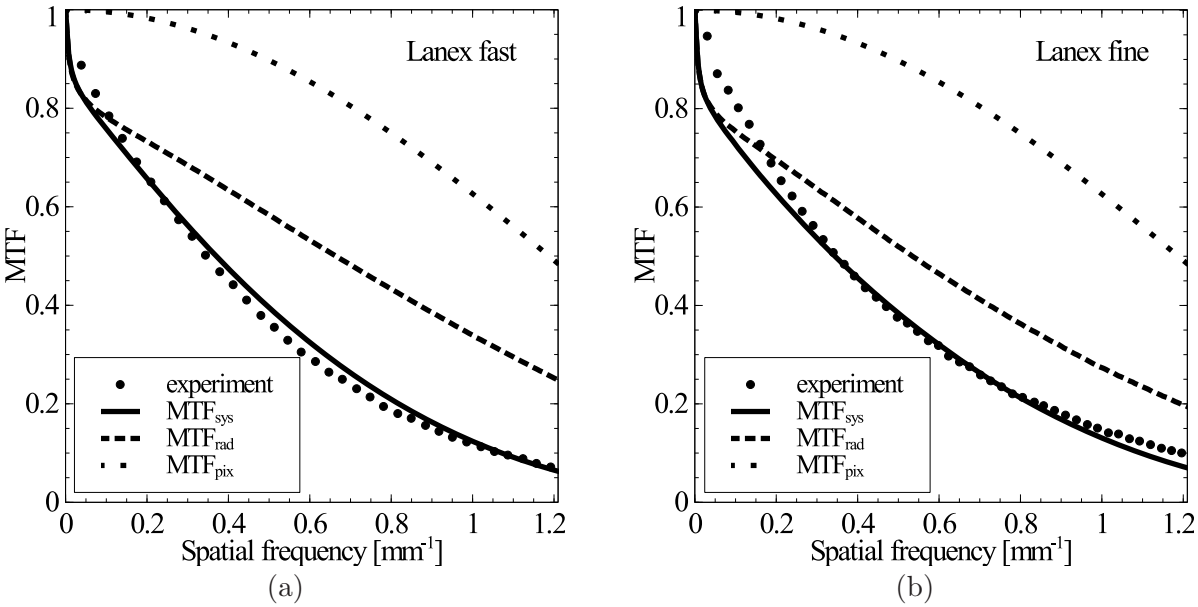

(a) (b)

Figure 4.9 Modulation transfer function for the (a) Lanex Fast-B screen and (b) Lanex Fine screen. The results from our Monte Carlo simulation are compared with measurements by El-Mohri et al. (2001).

In terms of spatial resolution, we compared our results to MTF values previously published by El-Mohri et al. (2001). We adapted our model detector to their set-up to produce comparable results: 26x26 cm^2 detector size, 508 μm pixel pitch, 1 mm Cu build-up flush to the phosphor screen, Lanex Fine or Lanex Fast-B screen, and no front plates. A comparison of MTFs is shown in figure 4.9. The MTF$_{sys}$, which includes the effects of secondary radiation transport, optical photon transport, and the pixel aperture, agrees reasonably well with the experimentally measured

data. Notably, the experimental MTF measured by El-Mohri et al. (2001) does show a weaker characteristic low-frequency drop. The low-frequency drop is an often observed phenomena which originates from long-range scatter as well as back-scatter from behind the phosphor layer. Due to the lack of data on the prototype detector that was used for their experiment, we decided to use our own detector's support structure and back plate (table 4.1). Further differences arise from the different linac that was used in our Monte Carlo simulation. As previously observed by El-Mohri et al. (2001), the MTF curves show only a weak dependence on the screen type for MV radiation, because secondary particles of a MV beam are of much higher energy than for a kV beam and consequently travel further before depositing their energy.

Chapter 5

Actively Triggered 4d Cone-Beam CT Acquisition

5.1 Overview

4d cone-beam computed tomography (CBCT) is rapidly developing into a much-utilized clinical imaging modality (Sweeney et al. 2012). By increasing the number of 2d projections from 200-750 for a 3D reconstruction, to >1000 projections for a 4d CBCT, and binning the acquired projections into 8-10 respiratory phases, a video-like 4d sequences of the patient's respiratory movement is acquired (Sonke et al. 2005, Dietrich et al. 2006, Lu et al. 2007). This binning process happens 'after-the-fact', i.e. after the projections are acquired and the imaging dose is administered. Depending on the imaging frequency and the gantry rotation time (both are usually fixed), as well as the breathing period of the patient (which can vary during image acquisition), the projections are unevenly distributed over the respiratory phases. Especially the slow-moving peak-exhale and peak-inhale phases tend to accumulate more projections than the other phases. The individual projections for each respiratory phase are also bunched into narrow angular segments with large projection-free angular segments in between. All these effects can severely compromise the image quality (Hugo & Rosu 2012, O'Brien et al. 2013).

In order to compensate for losses in image quality caused by the fixed imaging frequency and the patient's breathing period, we developed a novel 4d CBCT acquisition framework based on actively triggered projections employing the forward-predicted position of the tumour at the time of image acquisition. The forward-prediction of the tumour position was independently established using two different input signals: (i) an electromagnetic tracking system based on implanted EM-transponders which act as a surrogate for the tumour position, and (ii) an external motion sensor measuring the chest-wall displacement and correlating this external motion to the phase-shifted internal motion derived from the acquired images.

Publication

This chapter is currently being prepared for a journal submission (Fast et al. 2013 c). Parts of the results have been presented at international conferences (Fast et al. 2012 c, Fast et al. 2013 b).

Acknowledgement

The author would like to acknowledge the support of Gernot Echner (DKFZ) in modifying the lung phantom for use on the 4d motion platform. Thanks to Dr. Gerhard Lechsel and Anup

John (Siemens Healthcare) for supporting the use of the Siemens reconstruction tool. Dose measurements cited in this chapter were performed by Eric Wisotzky (DKFZ).

5.2 Introduction

The acquisition of 4d cone-beam computed tomography (CBCT) data sets prior to treatment has become feasible for most radiotherapy vendors in recent years. 4d CBCT has been demonstrated on Elekta (Sonke et al. 2005), Varian (Lu et al. 2007), and Siemens (Dietrich et al. 2006) linear accelerator platforms. 4d CBCT images provide valuable additional information for the clinician compared to the conventional 3d CBCT reconstruction (Sweeney et al. 2012): not only the average tumour position, but also the extent of the motion amplitude is provided. Especially in combination with 4d treatment planning CTs, this potentially allows one to estimate the validity of the treatment plan under consideration of the motion 'trajectory-of-the-day'. In terms of image quality, 4d reconstructions effectively mitigate motion-related image artefacts (Sonke et al. 2005). This is achieved by sorting individual projections into 8-10 respiratory phases, either according to the position in the breathing cycle (phase-binning) or the amplitude (displacement-binning) at the time of image acquisition (Abdelnour et al. 2007). Importantly, it is necessary to obtain information about the respiratory trajectory over the course of image acquisition. The information can be extracted from independent additional systems, e.g. belt-mounted pressure sensors, optical or infra-red surface sensors, spirometers etc. (Moorrees & Bezak 2012), or it can be extracted from the images themselves. The latter approach is commonly known as 'Amsterdam shroud' (Zijp et al. 2004, van Herk et al. 2007) but other ways of deriving the motion information from the projections have also been presented (Yan et al. 2013).

There are, however, also a few downsides to consider when employing 4d CBCT images: (i) typical image acquisition times (∼4-6 mins) are sharply increased compared to standard 3d acquisitions (∼1-2 mins); (ii) imaging dose is also much higher, mainly due to an increase in the number of projections (from 200-750 to >1000); (iii) the number of projections are unevenly distributed over the respiratory phases, possibly leading to variations in image quality for the different phases; and (iv) the projections of each individual respiratory phase are not evenly distributed over the gantry rotation, resulting in view-aliasing/streaking in the reconstructed 3d images (Leng et al. 2008, Hugo & Rosu 2012, O'Brien et al. 2013).

Using the conventional 'passive' 4d CBCT acquisition technology, improving one of the above mentioned parameters (i-iv) usually comes at the cost of degrading one of the other parameters. Improving the view-aliasing, for example, can be achieved by reducing the gantry rotation speed (Ahmad et al. 2009, Hugo & Rosu 2012). Similarly it has been shown that post-processing steps like the McKinnon-Bates (MKB) algorithm (Zheng et al. 2011) reduce streaking. A limited number of studies have also reported on 'semi-active' 4d CBCT systems, such as gated-CBCT (Chang et al. 2006, Kincaid et al. 2013), where acquisition is only triggered if the motion falls within a predefined amplitude window. A common drawback of any gating approach is the increase in image acquisition times. Chang et al. (2006) have reported increases in gantry rotation times from the original 5 min for a continuous acquisition to 6-7 mins for the gated acquisition on an MV CBCT device. Kincaid et al. (2013) have discussed the trade-off between width of the gating window and gantry rotation time on their gated kV CBCT system. Recently, O'Brien et al. (2013) have suggested a mathematical model based on a 'representative' breathing trajectory which optimizes imaging frequency and gantry rotation speed to achieve an equidistant angular sampling between projections. They also suggest updating the model 'on-the-fly' based on the actual respiratory signal of the day. In case of breathing which becomes irregular, they suggest pausing the gantry rotation and image acquisition.

To overcome the uneven spreading of projections over respiratory phases seen in today's 4d CBCT systems, we are proposing a prospective binning technique in which kV projections are actively triggered based on the forward-predicted position of the tumour at the time of image acquisition. We will also demonstrate that our approach can regularize the angular sampling between projections to some extent. Importantly, this approach does not require any a-priori motion models, but instead relies on the respiratory motion of the day. Because on-the-fly adaptation of the gantry velocity was not available on our linac platform at the time of the experiments, we were limited to the imaging frequency as optimization parameter.

In order to forward-predict the position of the tumour at the time of image acquisition, we have heavily borrowed from approaches developed to compensate for the multi-leaf collimator latency during tumour tracking applications (Vedam et al. 2004, Krauss et al. 2011).

In this study, the forward-prediction of the tumour position was independently established using two different input signals: (i) the Calypso® (Varian Medical Systems, Inc.) electromagnetic (EM) tracking system based on implanted EM-transponders which act as a surrogate for the tumour position, and (ii) an external motion sensor measuring the chest-wall displacement correlated to the phase-shifted internal motion derived from the acquired images using the 'Amsterdam shroud' method (Zijp et al. 2004, van Herk et al. 2007). Throughout this chapter, we will use the following nomenclature for the two types of actively-triggered 4d CBCT:

- *EM-4d-CBCT*: the electromagnetic (*EM*) 4d CBCT mode,
- *COR-4d-CBCT*: the internal-external correlation (*COR*) 4d CBCT mode.

For the first approach, *EM-4d-CBCT*, it was necessary to minimize the EM-induced interference in the read-out of the flat-panel detector (FPD). Our research group has previously demonstrated a system for synchronized tumour tracking with electromagnetic transponders and kV x-ray imaging (Rau et al. 2008). In this system, image acquisition was only triggered during periods of EM 'silence' to obtain 2d projections free of the characteristic stripe artefacts. To ensure that the periods of EM silence were long enough to acquire artefact-free images, the EM update rate was reduced to ∼6 Hz resulting in a frame rate of ∼2.2 fps. Rau et al. (2008) already showed that the motion information gathered by the EM tracking system could be used to retrospectively bin the acquired kV projections into breathing phases for 4d CBCT reconstruction. For the current study, a much higher frame rate was desired and we therefore deployed a passive EM-shielding for the FPD.

The presence of the EM-array during kV acquisition also results in a characteristic absorption pattern superimposed on the anatomical image for certain gantry angles. Without further modifications to the projection images this yields heavily artefact-prone 3D images. To our knowledge, two approaches to correct for this artefact have been proposed: (i) Poludniowski et al. (2012) have suggested a three-step post-processing technique on the reconstructed images, and (ii) Maurer et al. (2011) have presented a filtering method which replaces 'bad' pixels belonging to the EM array structure with neighbouring 'good' pixels based on empirical gray-value thresholds. In this study, we are suggesting a new correction strategy which uses a-priori knowledge about the position of the EM array in the treatment room to identify affected pixels which need to be replaced by neighbouring pixels.

We also demonstrated the acquisition of single respiratory phases and a new dose-saving 4d CBCT mode, consisting of peak-exhale and peak-inhale images only:

- *Quasi 4d-CBCT*: only the extremal respiratory phases are acquired.

In principle, any subset of respiratory phases can be acquired. Looking at the peak-exhale as well as the peak-inhale phase seemed clinically most sensible to us, because it allows to describe the motion baseline as well as the motion amplitude.

5.3 Materials and methods

5.3.1 Experimental set-up

All experiments were performed on our Siemens research linear accelerator (linac) equipped with an additional x-ray tube and flat-panel detector (FPD) in the 'in-line' imaging geometry (Oelfke et al. 2006). The XRD 1640 AN1-ETS (PerkinElmer) detector uses a CsI phosphor screen and an anti-scatter grid for high image quality. A simplified schematic side view of the experiment is given in figure 5.1. Importantly, the set-up does not depend on the unique features (Nill et al. 2005) of the 'in-line' geometry, and is thus transferable to other geometries like the orthogonal imaging geometry.

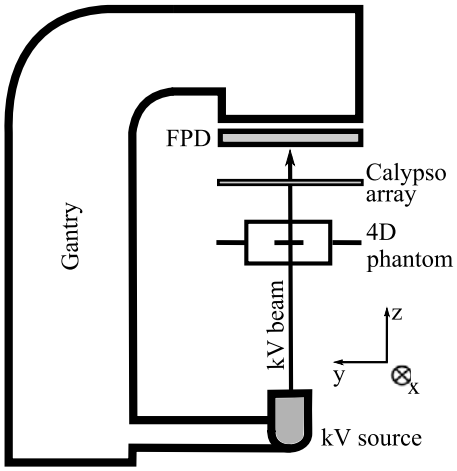

Figure 5.1 Side view of the experimental set-up. Note that the Calypso array was only present for the *EM-4d-CBCT* mode and was later removed for the *COR-4d-CBCT* mode.

5.3.2 Image acquisition

We developed a new control software (figure 5.2), partly based on a previously presented imaging framework (Fast et al. 2012) and a tracking framework (Krauss et al. 2011 b). The new *4d CBCT tool* handles the continuous stream of tumour or surrogate positions from the different position devices (section 5.3.3), continuously monitors the linac gantry angle, and organizes the forward-prediction of future tumour positions and thus respiratory phases. The tool also sends trigger requests to the external *X-ray controller* and post-processes subsequently acquired images.

The *X-ray controller* (Fast et al. 2012) was modified in such a way that it was possible to continuously trigger frames every 80 ms (based on a high-precision hardware counter). The 80 ms were chosen to accommodate for the 66.6 ms read-out time, approximately 10 ms x-ray exposure time and some contingency. At the beginning of the training phase, a start-up signal is sent from the *4d CBCT tool* to the *X-ray controller* via an ethernet connection which initiates the continuous triggering of offset frames. Similarly, a stop signal is sent at the end of the 4d CBCT acquisition. Importantly, requests for a new x-ray projection, which may arrive from the *4d CBCT tool* at any time, are only processed for the image following the next image. By introducing this artificial delay of 80 ms, we ensure that at least one offset image is acquired between two x-ray projections. This in turn ensures a better image quality due to the reduction of ghosting with every frame read-out (Siewerdsen & Jaffray 1999, Mail et al. 2008). The minimum time between two x-ray projections is thus limited to 160 ms. Assuming that the requests for new kV projections arrive

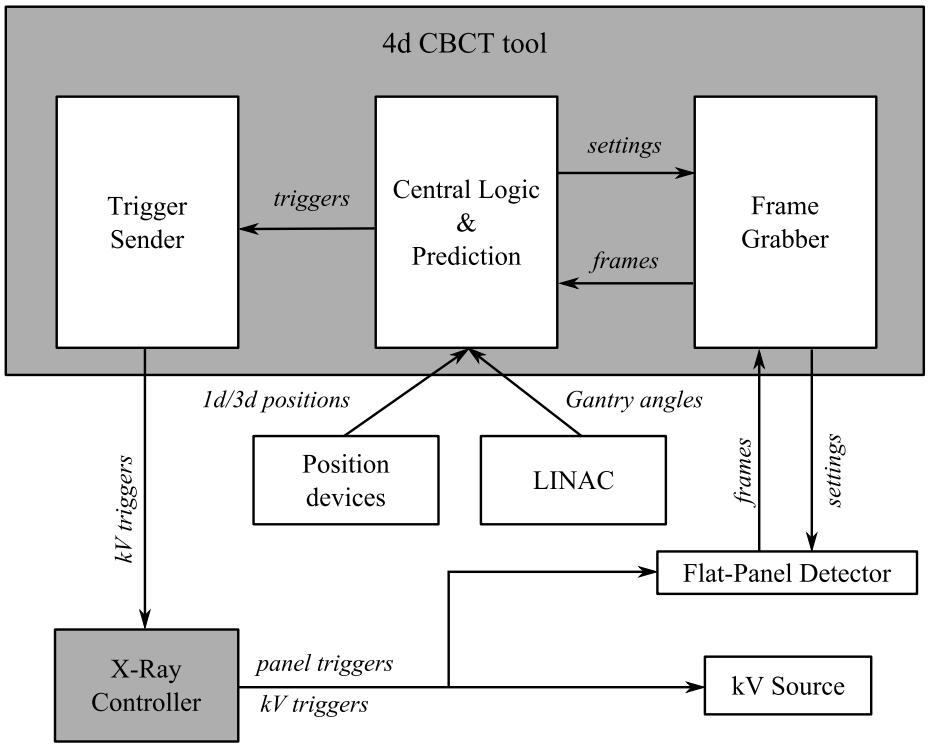

Figure 5.2 Schematic representation of the *4d CBCT tool* and the *X-ray controller*. The *X-ray controller* is an additional in-house developed software and hardware solution (Fast et al. 2012), which manages the acquisition of x-ray images.

at random times, an average latency of 40 ms is therefore introduced through the asynchronous operation of the *4d CBCT tool* and *X-ray controller*. Together with the 80 ms from the offset image, this adds up to an effective latency of the x-ray imaging chain of 120 ms.

All projections were acquired at 121 kVp using the lowest available exposure setting of 0.5 mAs and the 1.0 pF detector gain setting.

EM-shielding of the flat-panel detector

Due to the radio emissions of the EM-array, it is impossible to simultaneously operate EM tracking and acquire artefact-free images with the FPD (Rau et al. 2008, Poludniowski et al. 2012). Figure 5.3 demonstrates how the electromagnetic interference from the Calypso antenna array disturbs the flat-panel read-out electronics. The characteristic EM-induced stripes along the gate-lines of the detector occur in seemingly random clusters along the read-out lines (cf. figure 1 from Rau et al. (2008)). Considering the dynamic range of the detector (16 bit) and typical count values of ∼1000, it becomes clear that the unshielded FPD is rendered useless.

For the *EM-4d-CBCT* mode, we have therefore used a very thin Aluminium Faraday 'cage' for the detector that removes most EM-induced artefacts. The cage design was inspired by a previously reported shielding of an ion chamber array (Keall et al. 2011). Crucially, the shielding was designed to have little to no impact on the diagnostic image quality. Given an Aluminium thickness of ∼13 μm, four layers of Aluminium foil amount to ∼0.14 mm of water-equivalent thickness. Additional openings of the detector housing (outside of the detection area) were closed off with Copper shielding tape.

Users of the EM-tracking system are usually advised to keep electronic or metallic objects away from the antenna array as well as the EM-transponders to avoid interference with the radio waves.

Xiong et al. (2012) have discussed how EM-induced eddy currents on neighbouring conducting surfaces influence the accuracy of EM-tracking. In order to differentiate random position fluctuations from deviations in the mean detected 3d position, we first measured the transponder positions for a static phantom, with and without deploying the FPD at gantry angle 0° (worst case scenario in terms of FPD to EM-array distance for our experimental set-up). We then quantified the random position fluctuations with a moving phantom under rotating gantry, by comparing the recorded trajectory with an ideal fit according to equation 5.5.

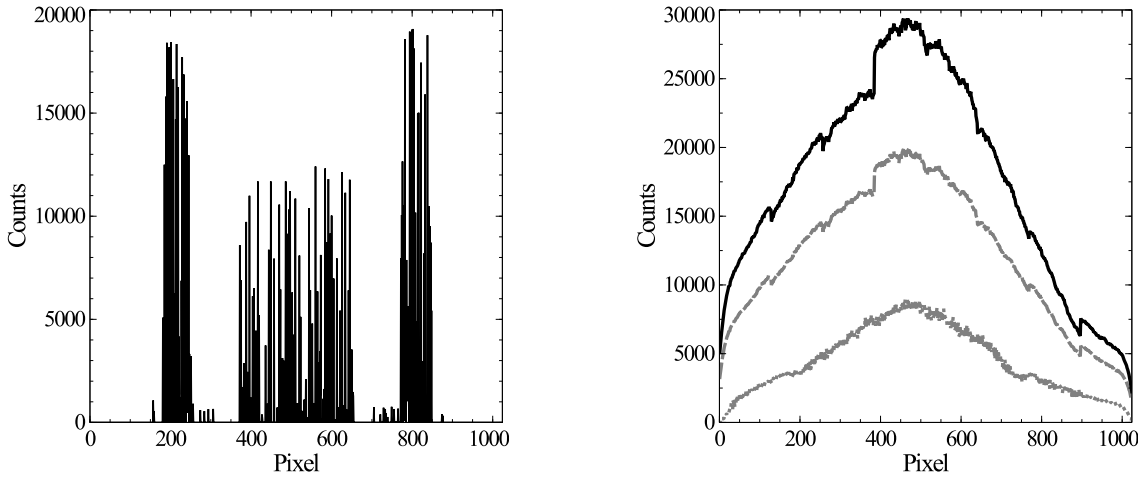

(a) Read-out direction. (b) Gate-line direction.

Figure 5.3 Sample of EM-induced stripes in the unshielded FPD. The detector gain was set to 0.5 pF and the FPD to EM-array distance was 18.5 cm at gantry angle 0°. (a) Median in gate-line direction, (b) three typical sample stripes in more detail.

Estimation of future respiratory phase

Based on the predicted internal tumour positions, the future respiratory phase was estimated according to the SI amplitude of the last complete inhale or exhale half-cycle. The maximum inhale and exhale positions of the respiratory waveforms were identified according to a technique suggested by Lu et al. (2006). Abdelnour et al. (2007) have reported for 4d CT acquisitions that the displacement-binning approach leads to better reconstruction than the phase-binning approach. For simplicity, the respiratory cycles was split into only five different breathing phases as opposed to the 8-10 (Keall et al. 2005, Sonke et al. 2005) usually used: peak-exhale, early-inhale, mid-ventilation, late-inhale, and peak-inhale. The five respiratory phases were chosen to represent 15%, 20%, 30%, 20% and 15% of the total amplitude respectively. Phases representing the fastest respiratory velocity were thus effectively given a larger amplitude window. Importantly, these definitions can be easily altered without compromising our acquisition scheme.

Cone-beam CT reconstruction

3d images were reconstructed from phase-binned 2d projections using an implementation of the FDK algorithm (Feldkamp et al. 1984) provided by Siemens. The necessary projection matrices were acquired by scanning a geometry calibration phantom as described by Pouliot et al. (2005). The individual 2d projections (1024x1024 pixels) were down-sampled to 512x512 pixels. A 3x3 median filter was applied to the images, and a Gaussian filter was selected for back-projection. Additionally, an iterative scatter correction (Maltz et al. 2008) was performed with the aid of pre-calculated scatter kernels. The reconstruction matrix size was set to 512^3 voxels and the cube volume to $(27.8\ \text{cm})^3$.

5.3.3 Tumour position devices

For the *EM-4d-CBCT* mode, a research version of the Calypso tumour tracking system was used to directly access the internal tumour position. This is a valid approach as long as the shift of the centre-of-gravity of the three EM transponders with respect to the tumour is rigid and known. Crucially, for our study the Calypso system offers a relatively high sampling rate of 25 Hz and features a well-defined[1] effective latency of approximately ∼120 ms (Krauss et al. 2011 b).

For the *COR-4d-CBCT* mode, a simple linear potentiometer used in a previous study (Krauss et al. 2012) was attached to the 4d motion platform to monitor the AP direction. The linear potentiometer was used as surrogate for more elaborate systems such as pressure-belts or surface-monitoring cameras which essentially convey the same information. The linear potentiometer was sampled at 30 Hz using an AD converter. The effective latency of this set-up was estimated at ∼40 ms (Krauss et al. 2012). The internal position was extracted from the images itself using a technique similar to the commonly known 'Amsterdam shroud (AS)' (Zijp et al. 2004, van Herk et al. 2007). An excellent description of the necessary image post-processing steps is given by Yan et al. (2013). We omitted the last step of calculating a horizontal derivative on the AS image since the artificial diaphragm edge of our phantom presented itself as a strong feature. Importantly, the AS techniques assumes that the diaphragm motion (which is most prominent in the SI derivative image) can be used as surrogate for the tumour motion. To convert the diaphragm positions (in pixel coordinates) derived from the AS image into absolute room coordinate positions, we geometrically back-projected them onto the SI axis in the isocenter plane.

5.3.4 Forward-prediction method

The forward-prediction of the tumour position is based on a linear regression (LR) algorithm, described in detail by Krauss et al. (2011). The prediction is necessary to bridge not only the position device latencies (40 ms and 120 ms), but also the average time before a new projection can be triggered (120 ms) as explained in section 5.3.2. Due to the relatively short cumulative prediction lengths of only 160 ms and 240 ms, a more complex prediction algorithm such as a neural network (NN), kernel density estimation (KDE) or a support vector regression (SVR) would yield very similar prediction results even for non-regular real patient trajectories. We also employed an adaptive-expansive training scheme (Krauss et al. 2011), in which the sliding training window is gradually expanded from an initial 23 s to 60 s. The preprocessing length of 7 s is added to the training window, resulting in a first predicted position 30 s into the data acquisition. For the *EM-4d-CBCT* mode, the continuous stream of 3d positions from the Calypso device was used as input for the prediction. For the *COR-4d-CBCT* mode, the 1d external signal from the linear potentiometer was used to establish the prediction.

5.3.5 Internal-external correlation model

An internal-to-external motion model is established from the first 40 x-ray projections for the *COR-4d-CBCT* mode, by correlating the external chest-wall displacement (AP direction) with the internal motion (SI direction) derived from the images. The creation of the correlation model has been previously described by Krauss et al. (2012). These initial projections were acquired under a rotating gantry at a relatively high frequency of 6.25 Hz to cover 1-2 breathing cycles with a good sampling. During post-processing, these images were binned and used alongside the actively triggered frames. Once established, the correlation model maps predicted external positions onto equivalent internal positions which are subsequently used to forecast the respiratory

[1] The latency is automatically reported along with each position.

phase. Using the existing control software, it is already possible to update the correlation model after subsequent frames exceeding the 40th frame. Due to the regular nature of the respiratory trajectories used, we did however decide to use the once established correlation model for the entire image acquisition.

5.3.6 Adaptive gantry speed and projection clustering

The breathing pattern during the training phase (first 30 s of data acquisition with either the Calypso device or the linear potentiometer) is used to identify the breathing period T_{resp} by means of a Fourier transformation. Based on this information, the gantry rotation speed was selected depending on the total number of frames desired. Ideally, the gantry speed would constitute an additional degree of freedom, meaning that the gantry rotation speed would track the respiratory velocity or at least the breathing period of the patient. This would result in a more evenly distributed angular sampling and mitigate sampling artefacts arising from a breathing period which varies during CBCT acquisition. Due to hardware constraints, however, we were only able to set the gantry speed once before the beginning of the gantry rotation in this study.

For the full 4d CBCT acquisition, the gantry rotation time should not exceed a couple of minutes to avoid patient discomfort and drifting effects which tend to intensify with increasing procedure time. We have therefore set the maximum total acquisition time to 5 mins resulting in a minimum gantry speed of 72 °/min for a full scan and 40 °/min for a short scan.

The amplitude information from the last $2{\cdot}T_{resp}$ seconds of the training period is also used to dynamically calculated the average time t_i the tumour remains in a certain respiratory phase i. This information is then used to calculate the minimum time Δt_i between two projections based on the number n_i of desired projections per respiratory phase and breathing period:

$$\Delta t_i = t_i / n_i. \tag{5.1}$$

In practise, of course, n_i cannot be arbitrarily increased. The minimum time Δt_i between two projections is limited to 160 ms as explained in section 5.3.2. In this study, n_i was usually set to 2 or 3. O'Brien et al. (2013) previously noted that the clustering of many projections into narrow angular increments with wide projection-free angular segments in-between compromises the quality of the reconstructed image. Assuming a constant gantry speed, one projection per respiratory phase, and that each respiratory phase occurs only once per breathing period, the gantry spacing between two projections can be calculated from the breathing period T_{resp}:

$$\Delta\phi(t_{rot}, T) = \frac{(\phi_{end} - \phi_{start}) \cdot T_{resp}}{t_{rot}}, \tag{5.2}$$

where t_{rot} is the user selected gantry rotation time, ϕ_{start} is the gantry start angle, and ϕ_{end} is the gantry end angle. When clustering occurs, the inter-cluster angular spacing must be smaller than $\Delta\phi$ to account for the intra-cluster sampling.

5.3.7 Image post-processing

All acquired projections were corrected 'online' by subtracting an offset image and applying a gain correction map. Additionally, the dead pixels were corrected using a quad-directional linear interpolation (Nelms et al. 2009) from neighbouring good pixels.

Projections acquired with the *EM-4d-CBCT* mode were loaded into Matlab® (The MathWorks, Inc.) in an offline post-processing step to correct for artefacts originating from the EM-array or the EM-transponders.

The image quality was quantified in terms of the signal-to-noise ratio (SNR):

$$SNR = \frac{CT^m}{\sigma_{ROI}}, \tag{5.3}$$

and the contrast-to-noise ratio (CNR):

$$CNR = \frac{|CT^m_{lung} - CT^m_{tumour}|}{\sqrt{\sigma^2_{lung} + \sigma^2_{tumour}}}. \tag{5.4}$$

Here, CT^m abbreviates the mean CT-number of a region-of-interest (ROI) . The standard deviation within a ROI is referred to as σ_{ROI}. The CNR is calculated by defining a tumour tissue ROI and an adjacent lung tissue ROI.

Removal of EM-transponder artefacts

We noticed that the metallic EM-transponders cause radial streak artefacts in the transversal plane of the reconstructed 3d images. These metal artefact are a well known phenomena in kV CBCT and various correction strategies have been suggested in the literature (c.f. Wang et al. (2013)). Localizing the exact position of the EM-transponders in the 2d/3d images is key to their identification. Fortunately, the 3d position of the EM-transponders is independently known through the Calypso device for the time of image acquisition. Using the unique projection matrix for each gantry angle, we have geometrically forward-projected the 3d position of the individual EM-transponders onto their 2d position on the detector.

The following steps were then taken to identify pixels belonging to the EM-transponders:

1. cropping of a 39x39 region around the projected transponder position,
2. applying a 3x3 median filter to reduce noise,
3. applying the logarithm (to ensure that the pixel values are proportional to the radiological thickness) and enhancing contrast,
4. equalizing the histogram,
5. iteratively performing a region-growing algorithm with different thresholds to identify the best connected transponder region.

Once the pixels belonging to the EM-transponders were identified, their pixel values were replaced by neighbouring 'good' pixel values. To mimic the neighbouring noise characteristics, random noise of the same variance was added to each replaced pixel value.

Removal of EM-array artefacts

Due to the geometry of the experimental set-up (cf. figure 5.1), most of the 2d images are completely or partially superimposed by projections of the EM antenna array located just above the phantom at a distance of ∼18 cm from the isocenter (lower bound). Figure 5.4 exemplifies the gantry angle intervals that are effected. Assuming a full 360° gantry sweep, ∼80% of all projections are affected. For a 200° short scan, this could be reduced to ∼65% in a best case scenario.

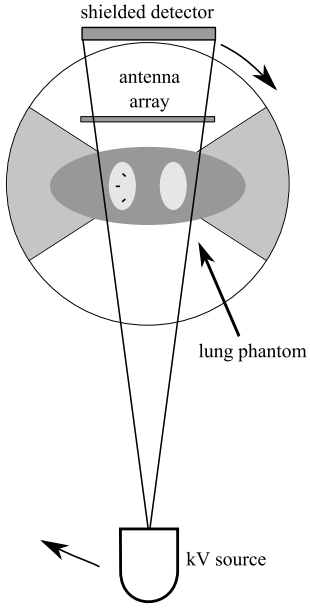

Figure 5.4 Simplified front view of the experimental set-up for the *EM-4d-CBCT* mode. The grey shaded areas mark the angular intervals for which the EM-array is not present in the 2d projection images.

The EM-array consists of 32 small receiver coils and 4 large sender coils (Balter et al. 2005). Whereas the receiver coils are almost invisible on the projections, the metallic wires of the sender coils are clearly visible. In the reconstructed images they cause -if not corrected for- prominent streak artefacts (Zhu et al. 2009). Poludniowski et al. (2012) have demonstrated a post-processing method working on the 3d data sets, which is able to mitigate the EM-induced artefacts. For this study, we propose a new correction method, which identifies pixels depicting the antenna wires on the 2d projections and replaces them by neighbouring unaffected pixels. This is the same correction approach used in dead pixel corrections. The following steps were taken for the correction algorithm:

1. subtracting a low-pass filtered version of the image from the original image,
2. converting the resulting image into a binary image,
3. matching the binary image with a forward-projected model of the antenna structure.

Steps 1-2 are necessary to separate low-frequency image components from the artificial high-frequency wire structure. These steps alone, however, are not able to separate the wires from other high-frequency objects such as noise and tissue borders. The third processing step is therefore crucial: we created a 2d model of the internal wire structure of the EM-array by scanning the array using a conventional CT scanner. Using this 2d model and an approximate 3d position of the antenna in the treatment room, the projection of the antenna onto the flat-panel detector was calculated using a forward-projection technique based on the projection matrix described above. The forward-projected binary image was then compared with the binary image from step 2 using the sum of squared differences. Because the exact position of the EM-array in room coordinates was not available to us (it should in principle be possible to retrieve it from the Calypso log files), we decided to optimize over array positions shifted in increments between ± 2 mm along the x and y axes, ± 4 mm along the z axis, and rotated in increments between $\pm 0.5°$ about the three main axes to find the best match. Overall, the optimization loop iterated over $\sim$5600 different

array positions to find the best possible match. The forward-projected antenna model was then used as correction map, similarly to a dead-pixel correction map.

5.3.8 Phantom study

All experiments were performed using an in-house developed thorax phantom (Dietrich et al. 2005). The phantom is based on a real patient CT scan and the main components are made from water-equivalent RW3 and lung-equivalent obomodulan type 300 (right and left lobe). The main axis dimensions are 13 cm (SI), ∼30 cm (LR), and ∼25 cm (AP). The tumour (4 cm SI, ∼3.1 cm LR, and ∼5.1 cm AP) is also made from RW3 and implanted in the right lobe together with the three EM transponders. The thorax phantom was then mounted onto a 4d programmable motion stage (Krauss et al. 2012). To simulate respiratory breathing, we have created two sets of 1d and 2d artificial sinusoidal trajectories with a breathing period of either 3.5 s or 5.0 s. For the 2d curves, the chest-wall movement (AP) was phase-shifted by 13°. The breathing patterns are summarized in table 5.1.

Table 5.1 Amplitudes and periods for the artificial breathing trajectories used in this study. The AP motion (5 mm) was phase-shifted by 13°.

Trajectory	Amplitude			Period
	SI [mm]	AP [mm]	LR [mm]	τ [s]
A (1d)	15.0	0.0	-	3.5
B (2d)	15.0	5.0	-	3.5
C (1d)	15.0	0.0	-	5.0
D (2d)	15.0	5.0	-	5.0

The sinusoidal trajectories were parametrized in SI direction according to Lujan et al. (1999) as:

$$y(t) = y_o - b\,cos^4\left(\pi t/\tau - \phi\right), \tag{5.5}$$

where y_o is the peak-exhale position, b is the SI-amplitude, τ is the breathing period, and ϕ is the starting phase. In AP-direction, the parametrization was as follows:

$$z(t) = z_o - c\,cos^4\left(\pi t/\tau - (\phi + \delta\phi)\right), \tag{5.6}$$

where c is the AP-amplitude and $\delta\phi$ the phase difference causing the characteristic hysteresis ellipsoid (Seppenwoolde et al. 2002). No motion was assumed for the LR-direction, i.e. $x(t) = 0$.

5.3.9 Dose measurements

We estimated the imaging dose of our acquisition technique, by measuring the $CTDI_w$ (Fast et al. 2012 b) using the circular PTW CTDI body (32 cm diameter) phantom in combination with a PTW Semiflex 0.125 cm^2 ionization chamber (PTW Freiburg GmbH).

5.4 Results

5.4.1 Motion-induced artefacts

Figure 5.5 exemplifies how motion-induced artefacts are effectively mitigated for all respiratory phases in the *EM-4d-CBCT* mode. Clearly, the SI motion is completely eliminated for the extremal respiratory phases (peak-exhale and peak-inhale) where the tumour velocity is the lowest. For the mid-ventilation phase, which corresponds to the highest tumour velocity, a minimal smearing of the tumour-to-lung boundary can be detected.

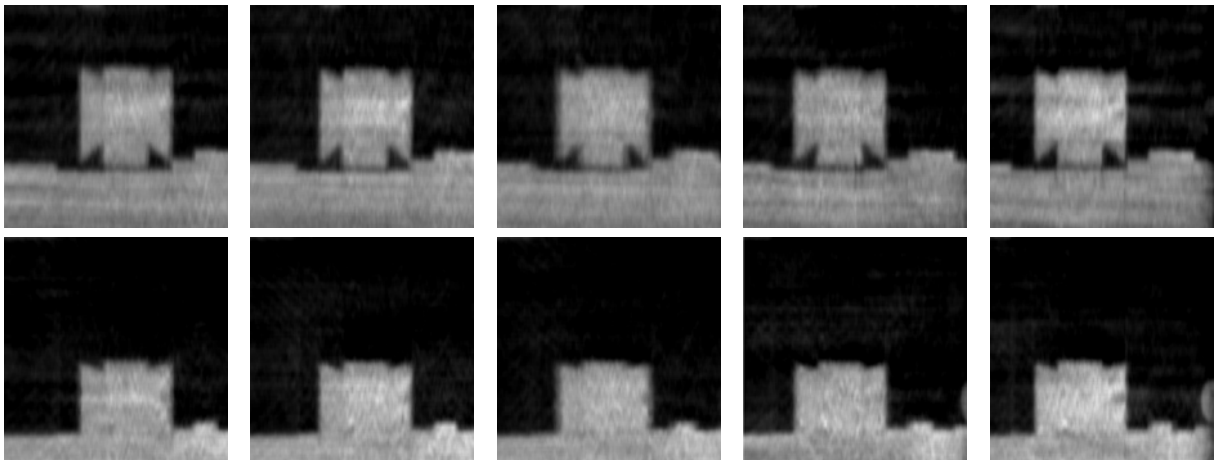

Figure 5.5 *EM-4d-CBCT* acquisition with trajectory A and 4 min gantry rotation: reconstructed sagittal slices (top row) and coronal slices (bottom row) of the tumour.

To investigate the motion-induced 'washing-out' of the tumour further, we cropped a 40x190 pixel ROI from the sagittal plane, calculated the row-median, and finally compared the resulting line profiles along the SI direction. Figure 5.6 demonstrates how the motion-induced loss of reconstructed tumour volume is sharply reduced for all respiratory phases when compared to a 3d reconstruction. The full width at half-maximum (FWHM) of the tumour measures as follows: 40.0 mm (peak-exhale), 38.3 mm (mid-ventilation), and 39.5 mm (peak-inhale). These values are broadly in line with the 40 mm measured at the physical phantom. The small reduction in SI FWHM for the mid-ventilation phase was to be expected from the visual impression of the reconstructed slice. The shift between peak-exhale and peak-inhale positions calculated from figure 5.6 is 13.6 mm. Considering the reconstructed pixel size of 0.54 mm and the effective respiratory displacement windows, the shift agrees reasonably well with the pre-defined amplitude of 15 mm.

Figure 5.7 shows a typical *Quasi COR-4d-CBCT* acquisition. As with the full 4d CBCT acquisitions, motion-related smearing of the tumour volume in SI direction is effectively mitigated. The transversal peak-inhale slice shows an increased level of view-aliasing/streaking compared to the peak-exhale slice. Although the number of frames, 127, was identical for both respiratory phases, the inter-cluster angular spacing is larger for the peak-inhale phase resulting in increased view-aliasing. This phenomena will be discussed in more detail in section 5.4.5.

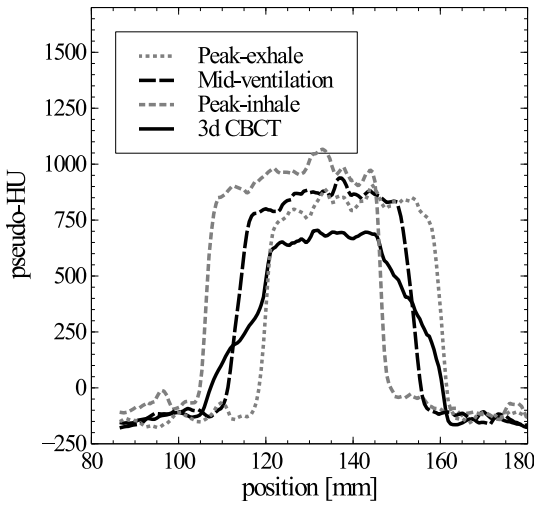

Figure 5.6 Line profile across the sagittal slices shown in figure 5.5. The line profiles were smoothed by a running average filter (span: 3). A 3d CBCT reconstruction is shown as reference.

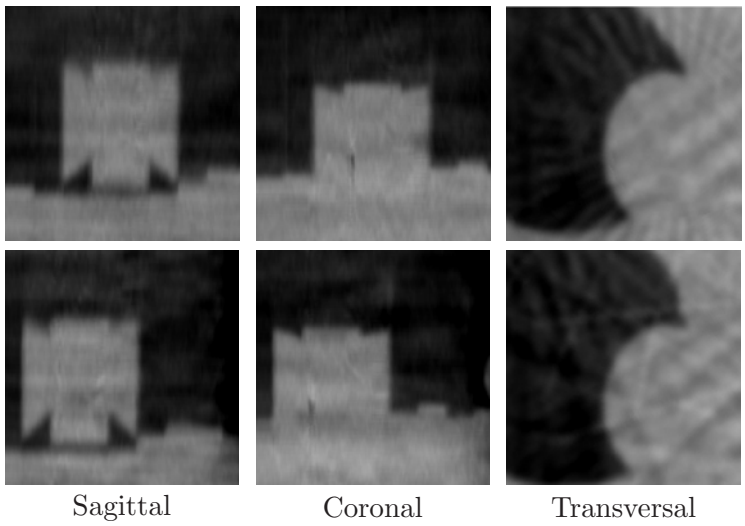

Figure 5.7 *Quasi COR-4d-CBCT* acquisition with trajectory D and 3.5 min gantry rotation: reconstructed peak-exhale (top row) and peak-inhale phase (bottom row). The dark spots in the coronal planes are caused by air cavities (which can host markers) in the tumour.

5.4.2 *EM-4d-CBCT* mode

Efficacy of the FPD shielding

As detailed in section 5.3.2, FPD and EM tracking system cannot simply operate in parallel due to EM-induced characteristic stripe artefacts along the gate-line direction of the FPD. Figure 5.8 demonstrates the strong influence of the detector gain setting on the stripe amplitude. For the lowest possible gain setting of 0.5 pF, the detector is more sensitive than for the highest possible gain setting of 8 pF and the EM-induced stripes are therefore much stronger. Employing the shielding reduces the stripe intensity by factors of ∼100 (8 pF) and ∼25 (0.5 pF) respectively. We also observed that the stripe intensity tends to fall with an increasing distance between the EM-array and the FPD for the unshielded detector. For the shielded detector, no clear dependence

on the distance was detectable.

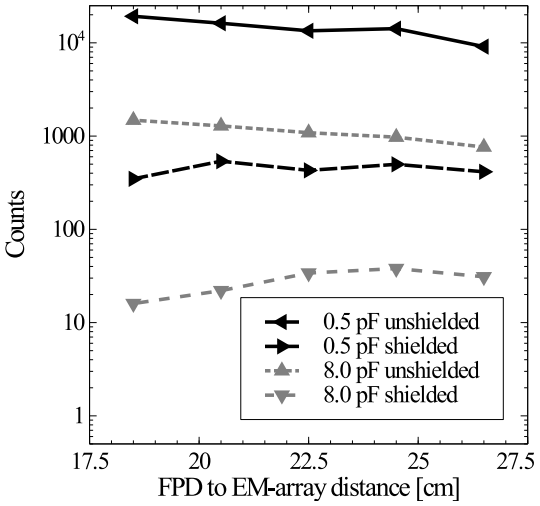

Figure 5.8 Reduction of EM-induced stripes with shielding as a function of the distance between the FPD and the EM-array (gantry angle 0°). Median stripe counts are shown.

Influence of the shielded FPD on the Calypso system

Due to the close proximity of the shielded FPD to the EM-array (~23 cm at gantry angle 0°), we observed an increased fluctuation of the 3d positions reported by the Calypso system. The fluctuations appeared to affect position measurements at all gantry angles. For a y-only phantom motion, we observed RMS (maximum) position errors of 0.32 (1.13) mm and 0.56 (1.99) mm respectively for the non-moving x and z axes.

Figure 5.9 shows reported y positions for trajectory A. To quantify the position error for the moving axis, we fitted the ideal sinusoidal trajectory according to equation (5.5). Here, the RMS (maximum) position error is 0.43 (1.24) mm. Clearly, the errors are most apparent for the peak-exhale breathing phase where the tumour slows down considerably. Based on these initial observations we decided to use a running median (span: 3) on the position data to smooth out these fluctuations.

Comparing the mean detected 3d position as a function of FPD to EM-array distance (table 5.2), revealed that the strongest (incorrect) shift in position is attributed to the z-axis which also showed the strongest random fluctuations and was orientated perpendicular to the EM-array and the FPD for these measurements. The systematic difference in x and y was smaller than 0.2 mm in all cases. Increasing the distance between the EM-array and the FPD to 22.5 cm or higher greatly reduced the influence on the detected mean z position.

Table 5.2 Difference in time-averaged centroid position (EM-transponders) with and without FPD deployed as function of the FPD to EM-array distance.

Distance [cm]	Δx [mm]	Δy [mm]	Δz [mm]
18.5	<0.1		<1.0
20.5	<0.2		<0.6
22.5	<0.2		
24.5	≤0.1		
26.5	<0.1		

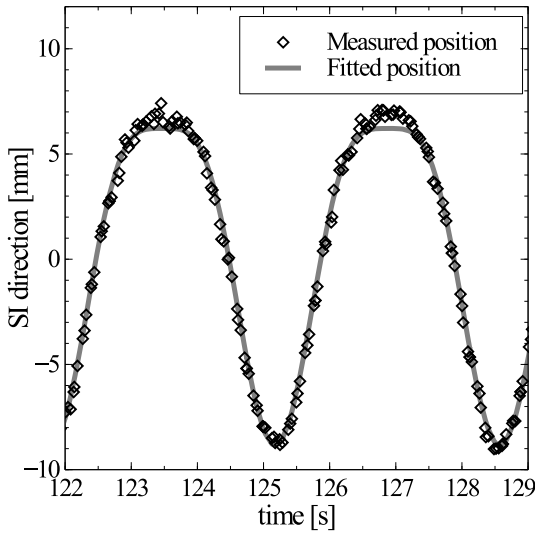

Figure 5.9 Trajectory A measured with the EM tracking system compared to a sinusoidal curve fitted according to equation (5.5). For the fit, only the phase shift $\delta\phi$ and the peak-exhale position y_o were free parameters.

Reduction of EM-transponder artefacts

The successful identification and removal of the metallic EM-transponders in the 2d projection images is exemplified in figure 5.10. For the transversal slice, the algorithm clearly reduces the radial streaks originating in the EM-transponder positions. Currently, the correction algorithm takes ∼0.8 s per image (three EM-transponders) using a non-optimized Matlab implementation. The fluctuations (especially) in z-positions from the Calypso system reported in the previous section, required us to use a relatively large ROI of 39x39 pixels around the projected centre of the EM-transponder to guarantee that the transponder (largest extent: ∼20 pixels) lay well within the ROI.

Reduction of EM-array artefacts

The superposition of the EM-array onto the 2d projections of the anatomy (cf. figure 5.4) leads to characteristic regular stripe artefacts in the reconstructed image (figure 5.11 (a)). By identifying pixels belonging to the EM-array and replacing them with neighbouring good pixels as outlined before, a clear reduction of the characteristic stripes is achieved (figure 5.11 (b)). This becomes even more apparent when looking at the difference image between original and corrected image (figure 5.11 (c)). In terms of the CNR (equation 5.4), we saw modest increases of about 3-7% between uncorrected and corrected images. This was mostly driven by a reduced variance of signal and hence an increased SNR in the lung as well as tumour tissue.

The run-time of the array correction algorithm currently stands at ∼2 min per projection using a non-optimized Matlab implementation. Looping over ∼5600 different array positions in the treatment room and forward-projecting each of these positions onto the flat-panel takes the largest part of that time. We also noticed certain inaccuracies in our array model, which are due to the limited spatial resolution of 1 mm of the CT scanner we used to build the model.

In order to gauge the best-case performance of our correction algorithm against a gold standard reconstruction, we took a 3d reconstruction (peak-exhale phase) from a *COR-4d-CBCT* acquisition. The reconstruction of this series, acquired without the EM-array in the beam path, was

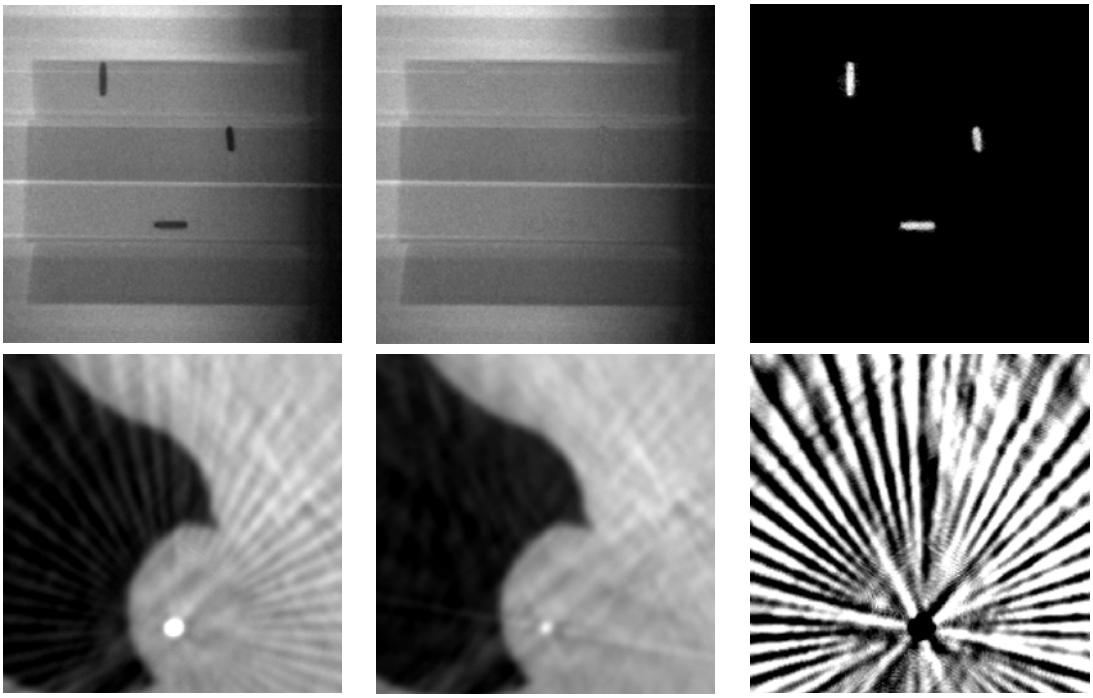

(a) Original. (b) Corrected. (c) Difference image.

Figure 5.10 Projection image (top row) and reconstructed transversal slice (bottom row) of the tumour with three implanted EM-transponders prior to and after EM-transponder correction.

assumed to be the gold standard. A second *EM-4d-CBCT* series that had a similar number of projections was used to create a correction map for each 2d projection. The correction map was then applied to the gold standard acquisition, effectively 'correcting' good pixels by the median of good pixel values (plus a random noise contribution) from a 9x9 neighbourhood. While the corrected wire regions were identifiable in the 2d projections, no difference could be seen by the human observer in the reconstructed images. An analysis of difference images from reconstructed slices of the gold standard and the corrected 3d images revealed that the mean difference was 0 HU and that the standard deviation was ±4 HU for the central region of the phantom.

5.4.3 *COR-4d-CBCT* mode

As for the *EM-4d-CBCT* mode, we first evaluated the position accuracy of the linear potentiometer by comparing the detected positions with an ideal sinusoidal fit. Figure 5.12 demonstrates the high degree of accuracy of the 4d motion platform and shows that the RMS position error (0.09 mm) of the linear potentiometer is negligible as expected.

Figure 5.13 (a) shows the high degree of prediction accuracy (RMS prediction error: 0.06 mm) for the external motion signal. For the internal SI motion axis (figure 5.13 (b)), there is a reasonable agreement between the positions calculated from the 'Amsterdam shroud' and the predicted positions derived with the internal-external correlation model. Clearly, the 13° phase shift between internal and external motion is successfully compensated for. Due to the coarse sampling of the internal positions (the initial imaging frequency is set to 6.25 Hz, whereas the external position is sampled with 30 Hz) some slightly larger deviations occur (RMS prediction error: 0.24 mm).

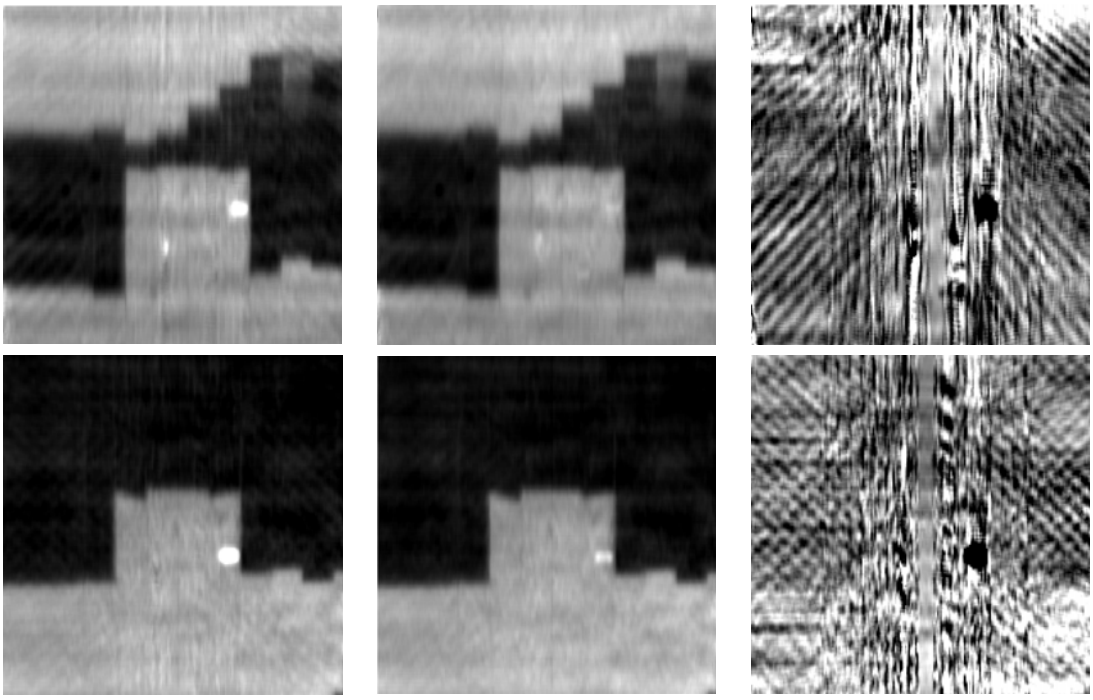

(a) Original. (b) Corrected. (c) Difference image.

Figure 5.11 Reconstructed sagittal (top row) and coronal (bottom row) before and after EM-array and EM-transponder correction.

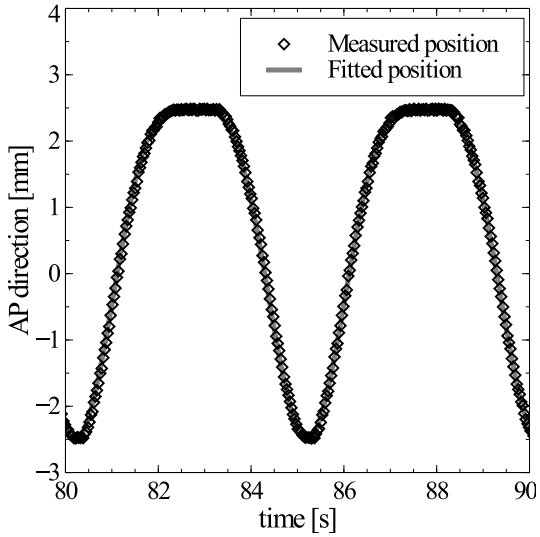

Figure 5.12 Trajectory D measured with the linear potentiometer (for details of the fit see figure 5.9).

5.4.4 Number of projections and imaging dose

We were able to demonstrate that it is feasible to distribute the number of projections more evenly over all respiratory phases for our actively triggered 4d CBCT modes. Table 5.3 lists the number of projections and the imaging dose administered per respiratory phase. For a traditional 4d CBCT acquisition, the phase with the most projections (peak-exhale) has almost four times as many projections as the phase with the least projections (late-inhale in our case). The latter phase, however, dictates the gantry rotation time and therefore the total number of projections.

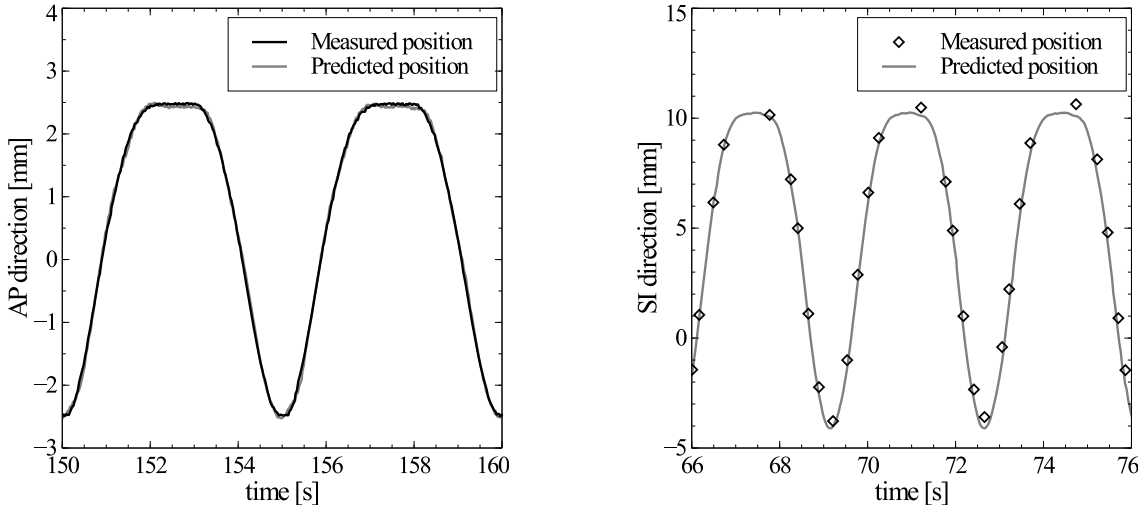

(a) External motion. (b) Internal motion.

Figure 5.13 *COR-4d-CBCT* mode: measured vs. predicted AP (external) and SI (internal) trajectories. Note the different y-axis scaling.

Reaching the necessary number of projections (say 90-100) for the least-likely respiratory phase, clearly comes at the cost of excess projections for other phases.

For the *EM-4d-CBCT* mode, the projections are much more evenly distributed compared to the traditional acquisition scheme. Now, the dose ratio between most-likely and least-likely respiratory phase is 1.3 (3.5 s breathing period) and 1.1 (5.0 s) respectively. The same holds true for the *COR-4d-CBCT* mode. Here, the dose ratio is 1.1 (3.5 s breathing period) and 1.1 (5.0 s; data not shown) respectively. Generally, the dose per respiratory phase varied between 1.7-2.6 mGy (90-140 frames) which can be extrapolated to a total dose of 17-26 mGy for a full 4d CBCT acquisition assuming 10 respiratory phases.

For the *COR-4d-CBCT* mode, a number of projections from the first 40-50 frames were disregarded for the CT reconstruction. These frames are necessary to establish the internal-external correlation model, but they either fall into undesired respiratory phases or their angular spacing is too small (we chose $<0.5°$ as a limit). The number of discarded projections is clearly highest for the *Quasi COR-4d-CBCT* acquisition (table 5.3). Here, the early-inhale, mid-ventilation, and late-inhale respiratory phases from the first 40-50 projections are not used during reconstruction.

We also demonstrated the feasibility (data not shown), of the acquisition of single respiratory phases for the *EM-4d-CBCT* mode. It was possible to reduce the total gantry rotation time to 2 min (peak-exhale-only or peak-inhale-only acquisitions) and 3 min (mid-ventilation-only acquisition) without compromising the number of projections compared to the full 4d acquisition (table 5.3).

5.4.5 Angular clustering of projections

By calculating the incremental changes in the gantry angle between subsequent projections of the same respiratory phase, we were able to quantify the angular clustering of projections. Depending on the gantry rotation speed, the imaging frequency and also the respiratory trajectory (especially its period), projections of a single phase are clustered around certain gantry angles. Figure 5.14 demonstrates that the intra-cluster angular separation of projections ($\leq 1°$) is much smaller than the inter-cluster separation ($\sim$3-5°) for a 4 min gantry rotation and a 3.5 s breathing period. Increasing the gantry velocity increases the angular separation between frames (which is beneficial

Table 5.3 Number of projections and imaging dose for the different 4d CBCT techniques. The trajectories are described in table 5.1. The number of unused projections in brackets refers to projections necessary to establish the internal-external correlation model that are discarded prior to reconstruction.

Arc rotation [min]	Trajectory	Respiratory phase	Number of projections	$CTDI_w$ [mGy]
Traditional 4d CBCT				
2.8	A (1d)	Peak-exh.	440	7.9
		Early-inh.	148	2.7
		Mid-vent.	162	2.9
		Late-inh.	113	2.0
		Peak-inh.	195	3.5
EM-4d-CBCT				
4.0	A (1d)	Peak-exh.	142	2.6
		Early-inh.	127	2.3
		Mid-vent.	142	2.6
		Late-inh.	110	2.0
		Peak-inh.	134	2.4
4.0	B (1d)	Peak-exh.	99	1.8
		Early-inh.	99	1.8
		Mid-vent.	99	1.8
		Late-inh.	92	1.7
		Peak-inh.	98	1.8
COR-4d-CBCT				
4.0	C (2d)	Peak-exh.	133 (15)	2.4 (0.3)
		Early-inh.	143 (4)	2.6 (0.1)
		Mid-vent.	142 (2)	2.6 (0.0)
		Late-inh.	138 (2)	2.5 (0.0)
		Peak-inh.	129 (10)	2.3 (0.2)
5.0	D (2d)	Peak-exh.	123 (21)	2.2 (0.4)
		Early-inh.	125 (2)	2.2 (0.0)
		Mid-vent.	118 (1)	2.1 (0.0)
		Late-inh.	126 (2)	2.3 (0.0)
		Peak-inh.	114 (3)	2.1 (0.1)
Quasi COR-4d-CBCT				
3.5	D (2d)	Peak-exh.	127	2.3
		other	(41)	(0.7)
		Peak-inh.	127	2.3

for the intra-cluster spacing), but it also increases the inter-cluster spacing which will result in more view-aliasing/streaking in the reconstructed images.

For a traditional (i.e. continuously acquired and retrospectively binned) 4d CBCT acquisition (figure 5.14 (a)), the probability distribution of angular increments has a very distinct maximum at $\sim 0.3^\circ$ for the peak-exhale respiratory phase. Clearly, dose is wasted here since neighbouring projections convey much the same information into the reconstruction process. For the actively triggered mode, the number of projections per cluster is reduced by six resulting in a coarser intra-cluster sampling and a shift of the relative weight of the distribution towards larger angular increments. If only one projection per respiratory cycle and breathing period was desired, the clustering would vanish altogether and a single distinct peak would dominate the angular dis-

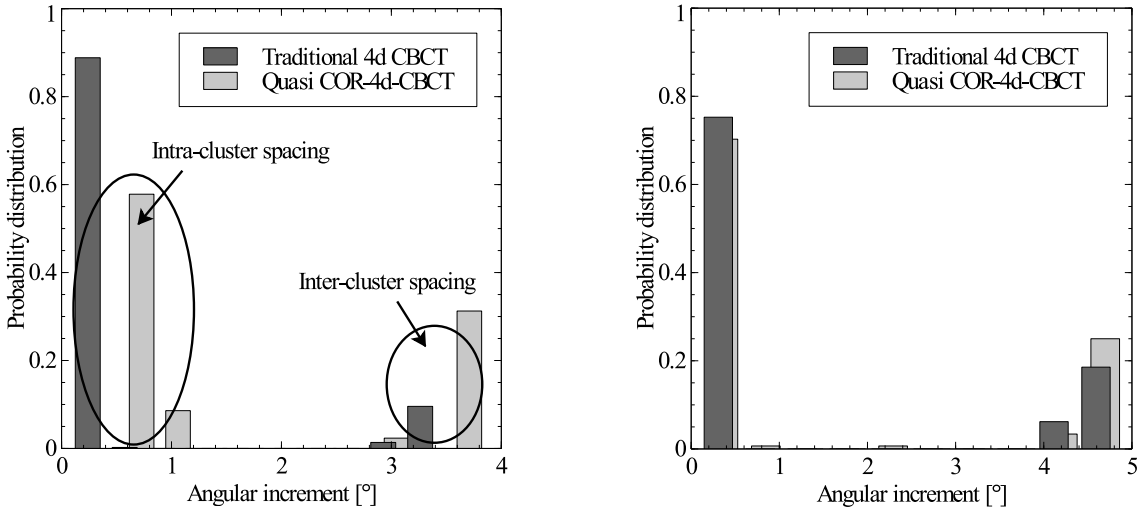

(a) Peak-exhale. (b) Peak-inhale.

Figure 5.14 Angular clustering for a traditional 4d CBCT and an actively triggered *Quasi COR-4d-CBCT* acquisition of trajectory C. The probability is normalized to 1 and the angular increment to a 4 min rotation.

tribution. Figure 5.14 (b) shows that the redistribution between intra-cluster and inter-cluster angular sampling is a lot less dramatic for the peak-inhale respiratory phase, because the tumour is about twice as likely to be in the peak-exhale phase than in the peak-inhale phase. This reduces the number of frames acquired in the latter phase accordingly. Consequently, the intra-cluster sampling changes little and the reduction in the number of projections for the actively triggered acquisitions compared to traditional 4d CBCT acquisitions is weaker for the peak-inhale respiratory phase (table 5.3).

Comparing the actively triggered peak-exhale and peak-inhale phases (figure 5.14) also shows how the intra-cluster angular sampling diverges once the imaging frequency is optimized individually for each respiratory phase. While the sampling is acceptable for the peak-exhale projections ($\sim$1°), it is still rather fine for the peak-inhale projections ($\sim$0.3°). The inter-cluster gap is also smaller by about 1° for the peak-exhale phase because of the increased likelihood of being in peak-exhale (compared to peak-inhale). Simply not acquiring some of the finely spaced peak-inhale projections would lead to a significant drop in the total number of projections for that breathing phase which might also not be desirable.

5.5 Discussion

We were able to demonstrate the feasibility of our new actively triggered acquisition technique for a variety of scanning protocols ranging from full 4d CBCT scans to single-phase acquisitions. As in traditional 4d CBCT acquisitions, a significant reduction in motion-related artefacts at the tumour surface was achieved. More importantly, we showed that by optimizing the imaging frequency for each individual respiratory phase, projections and thus imaging dose can be evenly spread over all respiratory phases. The remaining small imbalance in the number of projections between the respiratory phases can be explained based on two factors: first, for the 3.5 s breathing period, the time spent in the early-inhale and late-inhale respiratory phases was of the same order as the minimum time between two projections (160 ms). In those cases it frequently happened that only one projection was triggered even though two were desired to achieve the same number of projections in all phases. Secondly, projections acquired at the very end of the previous respiratory

phase prevented the acquisition of a new frame at the beginning of the following respiratory phase for the same reason given before.

For the *EM-4d-CBCT* mode, the characteristic EM-induced stripe artefacts in the FPD were reduced to an acceptable level by our shielding design. Reconstruction artefacts stemming from the presence of the EM-array and the EM-transponders were greatly reduced. Due to the limited resolution of the CT scanner that was used to construct the EM antenna model, we could not realize the full potential of our EM-array correction strategy. In future, a higher resolution scan of the antenna array should greatly improve the accuracy of the model. A better model together with more accurate information about the room position of the EM-array will greatly speed up the correction algorithm by reducing the number of array positions that need to be channelled through the optimization loop.

For cases where the insertion of EM-transponders is not desired or feasible, we demonstrated that the novel *COR-4d-CBCT* acquisition mode is a suitable alternative. Assuming a total imaging dose of 17-26 mGy for a full 4d CBCT acquisition with 10 respiratory phases, we think that the additional $\leq$1 mGy necessary to establish the internal-external correlation model is acceptable. We also showed the substantial dose saving potential of the *Quasi 4d-CBCT* mode, in which only peak-exhale and peak-inhale projections are actively triggered. The total (utilized) dose of a typical *Quasi COR-4d-CBCT* acquisition was only 4.6 mGy, with an additional 0.7 mGy that was necessary to establish the correlation model. Compared to the full 4d CBCT acquisition, the acquisition time for the *Quasi 4d-CBCT* mode can be reduced to 2-3 min, depending on the breathing period, without falling below 100 projections per respiratory phase. This is due to the fact that the extremal respiratory phases are much more likely than the other phases, and that 'waiting' for these other phases is not necessary.

Clearly, the image acquisition time should be kept to a minimum to increase patient comfort and reduce baseline drifts which might affect the quality of CBCT reconstruction. We showed that a constant gantry velocity together with the patient-specific breathing period, limits the achievable angular sampling when the imaging frequency is the only optimization parameter. A limited number of studies have previously suggested that the gantry rotation velocity should also be varied along with the imaging frequency to achieve an even angular sampling (O'Brien et al. 2013, Cooper et al. 2013). In principle there are three ways to adapt the gantry velocity during image acquisition: (i) relatively slow changes in breathing period could be matched by reciprocal changes in the gantry velocity. This would regularize irregular breathing trajectories, but it would not lead to perfect equidistant angular sampling. (ii) For gated CBCT acquisitions, the gantry could be programmed to move only during the pre-defined gating window (Kincaid et al. 2013). (iii) A more complex approach would see the gantry velocity track the respiratory velocity to achieve constant angular sampling as suggested by O'Brien et al. (2013). A motion regime could be imagined where the gantry velocity is increased for the slow-moving respiratory phases (peak-exhale, peak-inhale) and decreased for the other phases. If a respiratory phase is missed such a system could even pause the gantry rotation and wait for the next acquisition opportunity (which should occur after one complete breathing period). Clearly, mechanical stress on the gantry components and vendor-specific acceleration limits reduce the size of the solution space (O'Brien et al. 2013).

For us, the ideal active 4d CBCT system would not require any a-priori model of the tumour motion. Motion models derived during treatment planning, for example, must not reflect the motion-of-the-day. Instead, the future tumour position should be predicted as shown in this study. Previous work by Krauss et al. (2011) has demonstrated that predictions as far as 0.6 s into the future are feasible (using the kind of predictors used in this study) without great losses of prediction accuracy, even for irregular real-patient breathing trajectories. We expect that gantry velocity changes would have a slightly higher latency than the x-ray imaging chain (120 ms in this

study), but that they would be well within the 0.6 s mentioned before. It should be possible then to run two predictors in parallel, one with a relatively short lookahead length to trigger frame acquisition, and one with a larger lookahead length that adapts the gantry speed when necessary.

5.5.1 Limitations

Currently, the 4d CBCT acquisition framework as it stands has a number of principle limitations.

Firstly, it was not possible to change the gantry velocity on-the-fly, which limits the improvements in angular sampling as previously discussed. Secondly, the minimum time between two x-ray projections was 160 ms for our system since we chose to acquire at least one offset frame in-between two x-ray projections to minimize detector ghosting. This has lead to projections not being acquired when the previous projection belonged to another respiratory phase or when the time per respiratory phase was simply too short. Using a modern 30 Hz FPD with a 33.3 ms read-out time, the minimum time interval between two x-ray projections could safely be reduced to 90 ms.

For the *EM-4d-CBCT* mode, we observed that the presence of the shielded FPD influences the accuracy of the 3d positions reported by the Calypso system. Increasing the source-to-imager distance, improving the shielding design, or even optimizing the EM sensor array (Xiong et al. 2012) should hopefully mitigate this effect. We also observed a few remaining stripe artefacts (despite shielding). Reducing the EM tracking sampling rate as suggested by Rau et al. (2008) to, say, 15 Hz, would create longer periods of EM silence and consequently reduce the remaining stripe artefacts without much hampering the abilities of the motion predictor.

For the *COR-4d-CBCT* mode, the creation of the internal-external correlation model was limited to the first 40-50 internal positions which is sufficient for the kind of regular motion used in this study. In principle, the correlation model can and should be updated after each new projection to account for changes in breathing.

5.6 Conclusion and outlook

This study is the first experimental demonstration of a new 4d CBCT acquisition paradigm in which the user is enabled to select the respiratory phases desired for reconstruction prior to image acquisition. Projections are then actively triggered based on the forward-predicted position of the tumour at the time of image acquisition. By tailoring the imaging frequency to each individual respiratory phase, it is possible to evenly spread projections over all respiratory phases. Compared to the traditional approach of retrospective 'after-the-fact' respiratory sorting, imaging dose will either be saved or at least better utilized (i.e. shifted away from phases like peak-exhale). The next logical step in improving 4d CBCT is to adapt the gantry velocity on-the-fly to further regularize angular sampling.

Chapter 6

Conclusion

In this thesis, the use of linac-mounted x-ray imaging for intra-fractional motion management was explored. Reliably detecting the motion of the patient during a radiation treatment session is the first important link in the motion management chain as explained in chapter 2. It is a prerequisite for the advanced *adaptive radiation therapy* (ART) treatment schemes that are believed to improve treatment outcome (i.e. patient survival) with minimal radiation-induced side-effects.

At first, we investigated the properties of the unique in-line geometry for tracking applications (chapter 3). Our study indicates that our imaging system achieves a sub-mm position accuracy in detecting target motion when relying on implanted metallic markers. Importantly the latency of the imaging chain (including image acquisition, post-processing and marker detection) is well below 100 ms. Together with the maximum update frequency of $\sim$7 Hz, this should facilitate real-time tracking applications. Evolving further towards markerless tumour detection, which does not need the invasive procedure of implanting metallic markers, would be the next desirable step. For the conventional flat-panel detector (FPD) used in our initial study, however, we noticed a few MV-induced image artefacts which severely compromised the diagnostic image quality. These artefacts were: increased noise, MV scatter, and characteristic read-out sync stripes.

To address some of the shortcomings of the conventional FPD in the in-line geometry, we performed a full Monte Carlo simulation of the treatment beam interactions in the FPD and suggested possible changes to the detector design that would improve the detector's performance (chapter 4). The main change were a thinning of the support structure of the FPD, which minimizes the total absorption of the MV treatment beam within the detector by 60% while having little impact on the (stand-alone) kV imaging performance. The simulations and accompanying experiments with modified detector configurations suggest that significant performance improvements are achievable with today's detector technology.

Lastly, we improved 4d cone-beam CT acquisitions by actively triggering individual projections according to the predicted tumour position and respiratory phase. While CBCT imaging is not strictly speaking intra-fractional, since the projections are acquired just prior to irradiation, it is commonly assumed that it reflects the anatomy of the day better than for example the planning CT. Traditional 4d CBCT systems passively acquire projections at a fixed imaging frequency and sort projections into respiratory phases after the imaging dose is administered. This procedure frequently results in poor image quality for certain respiratory phases, and in excess imaging dose in others. We demonstrated that for our actively triggered system, projections (and thus dose) can be evenly distributed over respiratory phases which increases dose utilization and can improve the image quality.

6.1 Impact

The work presented in this thesis is based on conventional x-ray imaging technology of the kind that is already available on today's treatment devices. We first showed that quick and reliable motion detection is feasible using the 'in-line' imaging geometry. Then, we introduced and demonstrated a new paradigm for 4d CBCT: actively triggered image acquisition based on the forward-predicted tumour position. This leads to the conclusion that x-ray imaging is still underutilized in motion management and that its role will gradually increase and intensify over the coming years.

6.2 Outlook

Two principle limitations of x-ray imaging in intra-fractional motion management remain: first, imaging dose increases the secondary cancer risk of patients, and second, 3d image acquisition is not possible in the sub-second time frame needed for real-time interventions. The first issue is negligible if increases in the treatment accuracy, which are facilitated by the x-ray images, outweigh the additional imaging dose. Continuous improvements in detector technology may result in further reductions in imaging dose in future. The second limitation is more severe: the current (gantry-mounted) and also the next (robotic) generation of treatment devices will not allow for fast 3d image acquisitions. Having 3d information about the anatomy continuously available during irradiation is however crucial for guiding the treatment and correctly accounting for the actually delivered dose. Today's motion detection devices, like the ones presented in this thesis, very much focus on the tumour motion. In future, the positions and trajectories of neighbouring organs, especially organs-at-risk, will also need to be monitored for safe adaptation of the treatment beam. A promising new concept to achieve all this is the technologically challenging integration of the MR imaging device and the linear accelerator (Lagendijk et al. 2008, Fallone et al. 2009).

Bibliography

Abdelnour, A., Nehmeh, S., Pan, T., Humm, J., Vernon, P., Schöder, H., Rosenzweig, K., Mageras, G., Yorke, E., Larson, S. et al. (2007). Phase and amplitude binning for 4D-CT imaging, *Phys. Med. Biol.* **52**(12): 3515–3529.

Agostinelli, S., Allison, J., Amako, K., Apostolakis, J., Araujo, H., Arce, P., Asai, M., Axen, D., Banerjee, S., Barrand, G. et al. (2003). GEANT4-a simulation toolkit, *Nucl. Instrum. Meth. A* **506**: 250–303.

Ahmad, M., Balter, P., Munro, P., Lu, J. & Pan, T. (2009). Optimization of 4d cone-beam CT: evaluation of streaking artifacts and noise with various simulated gantry rotation speeds, *SPIE Conference Series*, Vol. 7258, p. 7.

Antonuk, L. E., Boudry, J., Huang, W., McShan, D. L., Morton, E. J., Yorkston, J., Longo, M. J. & Street, R. A. (1992). Demonstration of megavoltage and diagnostic x-ray imaging with hydrogenated amorphous silicon arrays, *Med. Phys.* **19**: 1455.

Antonuk, L., Yorkston, J., Boudry, J., Longo, M., Jimenez, J. & Street, R. (1990). Development of hydrogenated amorphous silicon sensors for high energy photon radiotherapy imaging, *IEEE T. Nucl. Sci.* **37**: 165–170.

Balter, J., Wright, J., Newell, L., Friemel, B., Dimmer, S., Cheng, Y., Wong, J., Vertatschitsch, E. & Mate, T. (2005). Accuracy of a wireless localization system for radiotherapy, *Int. J. Radiat. Oncol. Biol. Phys.* **61**(3): 933–937.

Berbeco, R. I., Hacker, F., Ionascu, D. & Mamon, H. J. (2007). Clinical feasibility of using an EPID in cine mode for image-guided verification of stereotactic body radiotherapy, *Int. J. Radiat. Oncol. Biol. Phys.* **69**(1): 258–266.

Berbeco, R., Jiang, S., Sharp, G., Chen, G., Mostafavi, H. & Shirato, H. (2004). Integrated radiotherapy imaging system (IRIS): design considerations of tumour tracking with linac gantry-mounted diagnostic x-ray systems with flat-panel detectors, *Phys. Med. Biol.* **49**: 243–255.

Bert, C., Metheany, K. G., Doppke, K. & Chen, G. T. (2005). A phantom evaluation of a stereo-vision surface imaging system for radiotherapy patient setup, *Med. Phys.* **32**: 2753–2762.

Boellaard, R., van Herk, M., Uiterwaal, H. & Mijnheer, B. (1998). First clinical tests using a liquid-filled electronic portal imaging device and a convolution model for the verification of the midplane dose, *Radiother. Oncol.* **47**(3): 303–312.

Boone, J. & Seibert, J. (1997). An accurate method for computer-generating tungsten anode x-ray spectra from 30 to 140 kV, *Med. Phys.* **24**: 1661–1670.

Brateman, L. (1999). The AAPM/RSNA physics tutorial for residents radiation safety considerations for diagnostic radiology personnel, *Radiographics* **19**(4): 1037–1055.

Briesmeister, J. (2000). MCNP^{TM}-a general monte carlo n-particle transport code, *Los Alamos National Laboratory Los Alamos, New Mexico* .

Brixner, L. (1987). New x-ray phosphors, *Mater. Chem. Phys.* **16**: 253–281.

Brock, J., Ashley, S., Bedford, J., Nioutsikou, E., Partridge, M. & Brada, M. (2008). Review of hypofractionated small volume radiotherapy for early-stage non-small cell lung cancer, *Clin. Oncol.* **20**(9): 666–676.

Brun, R. & Rademakers, F. (1997). ROOT-an object oriented data analysis framework, *Nucl. Instrum. Meth. A* **389**: 81–86.

Buzurovic, I., Huang, K., Yu, Y. & Podder, T. (2011). A robotic approach to 4d real-time tumor tracking for radiotherapy, *Phys. Med. Biol.* **56**(5): 1299–1318.

Chang, J., Sillanpaa, J., Ling, C. C., Seppi, E., Yorke, E., Mageras, G. & Amols, H. (2006). Integrating respiratory gating into a megavoltage cone-beam CT system, *Med. Phys.* **33**(7): 2354–2361.

Cho, B., Poulsen, P. R. & Keall, P. J. (2010). Real-time tumor tracking using sequential kV imaging combined with respiratory monitoring: a general framework applicable to commonly used IGRT systems, *Phys. Med. Biol.* **55**(12): 3299–3316.

Cho, B., Poulsen, P. R., Sawant, A., Ruan, D. & Keall, P. J. (2011). Real-time target position estimation using stereoscopic kilovoltage/megavoltage imaging and external respiratory monitoring for dynamic multileaf collimator tracking, *Int. J. Radiat. Oncol. Biol. Phys.* **79**(1): 269–278.

Cho, B., Poulsen, P. R., Sloutsky, A., Sawant, A. & Keall, P. J. (2009). First demonstration of combined kV/MV image-guided real-time DMLC target tracking, *Int. J. Radiat. Oncol. Biol. Phys.* **74**(3): 859–867.

Cho, M., Kim, H., Graeve, T., Yun, S., Lim, C., Cho, H. & Kim, J. (2008). Measurements of x-ray imaging performance of granular phosphors with direct-coupled CMOS sensors, *IEEE T. Nucl. Sci.* **55**: 1338–1343.

Cooper, B. J., O'Brien, R. T., Balik, S., Hugo, G. D. & Keall, P. J. (2013). Respiratory triggered 4d cone-beam computed tomography: A novel method to reduce imaging dose, *Med. Phys.* **40**(4): 041901.

Depuydt, T., Verellen, D., Haas, O., Gevaert, T., Linthout, N., Duchateau, M., Tournel, K., Reynders, T., Leysen, K., Hoogeman, M., Storme, G. & Ridder, M. D. (2011). Geometric accuracy of a novel gimbals based radiation therapy tumor tracking system, *Radiother. Oncol.* **98**(3): 365–372.

Deutschmann, H., Kametriser, G., Steininger, P., Scherer, P., Schöller, H., Gaisberger, C., Mooslechner, M., Mitterlechner, B., Weichenberger, H., Fastner, G., Wurstbauer, K., Jeschke, S., Forstner, R. & Sedlmayer, F. (2012). First clinical release of an online, adaptive, aperture-based image-guided radiotherapy strategy in intensity-modulated radiotherapy to correct for inter- and intrafractional rotations of the prostate, *Int. J. Radiat. Oncol. Biol. Phys.* **83**(5): 1624–1632.

Dick, C. & Motz, J. (1981). Image information transfer properties of x-ray fluorescent screens, *Med. Phys.* **8**: 337–46.

Dietrich, L., Jetter, S., Tücking, T., Nill, S. & Oelfke, U. (2006). Linac-integrated 4d cone beam CT: first experimental results, *Phys. Med. Biol.* **51**(11): 2939–2952.

Dietrich, L., Tücking, T., Nill, S. & Oelfke, U. (2005). Compensation for respiratory motion by gated radiotherapy: an experimental study, *Phys. Med. Biol.* **50**(10): 2405–2414.

D'Souza, W. D. & McAvoy, T. J. (2006). An analysis of the treatment couch and control system dynamics for respiration-induced motion compensation, *Med. Phys.* **33**: 4701–4709.

Eijk, C. (2002). Inorganic scintillators in medical imaging, *Phys. Med. Biol.* **47**: R85–R106.

El-Mohri, Y., Antonuk, L. E., Zhao, Q., Choroszucha, R. B., Jiang, H. & Liu, L. (2011). Low-dose megavoltage cone-beam CT imaging using thick, segmented scintillators, *Phys. Med. Biol.* **56**(6): 1509–1527.

El-Mohri, Y., Jee, K., Antonuk, L., Maolinbay, M. & Zhao, Q. (2001). Determination of the detective quantum efficiency of a prototype, megavoltage indirect detection, active matrix flat-panel imager, *Med. Phys.* **28**: 2538–2550.

Faddegon, B. A., Aubin, M., Bani-Hashemi, A., Gangadharan, B., Gottschalk, A. R., Morin, O., Sawkey, D., Wu, V. & Yom, S. S. (2010). Comparison of patient megavoltage cone beam CT images acquired with an unflattened beam from a carbon target and a flattened treatment beam, *Med. Phys.* **37**(4): 1737–1741.

Faddegon, B. A., Wu, V., Pouliot, J., Gangadharan, B. & Bani-Hashemi, A. (2008). Low dose megavoltage cone beam computed tomography with an unflattened 4 MV beam from a carbon target, *Med. Phys.* **35**: 5777–5786.

Fallone, B. G., Murray, B., Rathee, S., Stanescu, T., Steciw, S., Vidakovic, S., Blosser, E. & Tymofichuk, D. (2009). First MR images obtained during megavoltage photon irradiation from a prototype integrated linac-MR system, *Med. Phys.* **36**(6): 2084–2088.

Fast, M., Koenig, T., Oelfke, U. & Nill, S. (2012 b). Performance characteristics of a novel megavoltage cone-beam-computed tomography device, *Phys. Med. Biol.* **57**(3): N15–N24.

Fast, M., Krauss, A., Nill, S. & Oelfke, U. (2011 b). Tu-c-214-08: Position detection accuracy of a novel linac-mounted intra-fractional x-ray imaging system, *Med. Phys.* **38**: 3757.

Fast, M., Krauss, A., Oelfke, U. & Nill, S. (2012). Position detection accuracy of a novel linac-mounted intrafractional x-ray imaging system, *Med. Phys.* **39**: 109–118.

Fast, M., Oelfke, U. & Nill, S. (2011). 241 oral: A novel approach to linac-mounted intra-fractional x-ray imaging for motion management, *Radiother. Oncol.* **99**: S93–S94.

Fast, M., Oelfke, U. & Nill, S. (2013 b). Oc-0334: Actively triggered cone-beam CT acquisition based on electromagnetic respiratory motion tracking, *Radiother. Oncol.* **In Press**.

Fast, M., Teymurazyan, A., Pang, G., Oelfke, U. & Rowlands, J. (2013). Finding an improved amorphous-silicon x-ray flat-panel detector configuration for the in-line geometry, *Phys. Med. Biol.* **58**: 2305–2324.

Fast, M., Wisotzky, E., Oelfke, U. & Nill, S. (2012 c). Po-0856: Simultaneous use of an electromagnetic tracking device and a conventional flat-panel x-ray imager, *Radiother. Oncol.* **103**: S334–S335.

Fast, M., Wisotzky, E., Oelfke, U. & Nill, S. (2013 c). Actively triggered 4d cone-beam CT acquisition, *Med. Phys.* **Submitted**.

Feldkamp, L., Davis, L. & Kress, J. (1984). Practical cone-beam algorithm, *JOSA A* **1**(6): 612–619.

Ford, J. C., Zheng, D. & Williamson, J. F. (2011). Estimation of CT cone-beam geometry using a novel method insensitive to phantom fabrication inaccuracy: Implications for isocenter localization accuracy, *Med. Phys.* **38**(6): 2829–2840.

Fu, D. & Kuduvalli, G. (2008). A fast, accurate, and automatic 2d–3d image registration for image-guided cranial radiosurgery, *Med. Phys.* **35**: 2180–2194.

Fujita, H., Tsai, D., Itoh, T., Morishita, J., Ueda, K., Ohtsuka, A. et al. (1992). A simple method for determining the modulation transfer function in digital radiography, *IEEE T. Med. Imaging* **11**: 34–39.

Gayou, O. & Miften, M. (2007). Commissioning and clinical implementation of a mega-voltage cone beam CT system for treatment localization, *Med. Phys.* **34**: 3183–3192.

Godfrey, D. J., Yin, F.-F., Oldham, M., Yoo, S. & Willett, C. (2006). Digital tomosynthesis with an on-board kilovoltage imaging device, *Int. J. Radiat. Oncol. Biol. Phys.* **65**(1): 8–15.

Grant, D. G. (1972). Tomosynthesis: a three-dimensional radiographic imaging technique, *IEEE Trans. Biomed. Eng.* **19**(1): 20–28.

Greer, P. B. & Popescu, C. C. (2003). Dosimetric properties of an amorphous silicon electronic portal imaging device for verification of dynamic intensity modulated radiation therapy, *Med. Phys.* **30**: 1618–1627.

Groh, B., Siewerdsen, J., Drake, D., Wong, J. & Jaffray, D. (2002). A performance comparison of flat-panel imager-based MV and kV cone-beam CT, *Med. Phys.* **29**: 967–975.

Gustafsson, H., Vial, P., Kuncic, Z., Baldock, C., Denham, J. & Greer, P. (2011). Direct dose to water dosimetry for pretreatment IMRT verification using a modified EPID, *Med. Phys.* **38**: 6257–64.

Hanley, J., Debois, M. M., Mah, D., Mageras, G. S., Raben, A., Rosenzweig, K., Mychalczak, B., Schwartz, L. H., Gloeggler, P. J., Lutz, W. et al. (1999). Deep inspiration breath-hold technique for lung tumors: the potential value of target immobilization and reduced lung density in dose escalation, *Int. J. Radiat. Oncol. Biol. Phys.* **45**(3): 603–611.

Hiraoka, M., Matsuo, Y., Sawada, A., Ueki, N., Miyaba, Y., Nakamura, M., Yano, S., Kaneko, S., Mizowaki, T. & Kokubo, M. (2012). Realization of dynamic tumor tracking irradiation with real-time monitoring in lung tumor patients using a gimbaled x-ray head radiation therapy equipment, *Int. J. Radiat. Oncol. Biol. Phys.* **84**(3): 5.

Hsu, A., Miller, N., Evans, P., Bamber, J. & Webb, S. (2005). Feasibility of using ultrasound for real-time tracking during radiotherapy, *Med. Phys.* **32**: 1500–1512.

Hugo, G. D. & Rosu, M. (2012). Advances in 4d radiation therapy for managing respiration: Part i–4d imaging, *Z. Med. Phys.* **22**: 258–271.

ICRU (1993). *Prescribing, recording and reporting photon beam therapy*, International Commission on Radiation Units and Measurements. Report 50.

IEC (1996). Radiotherapy equipment-coordinates, movements and scales, *Technical Report IEC 1217*, The International Electrotechnical Commission.

Jaffray, D. A. & Siewerdsen, J. (2000). Cone-beam computed tomography with a flat-panel imager: initial performance characterization, *Med. Phys.* **27**: 1311–1323.

Jaffray, D., Battista, J., Fenster, A. & Munro, P. (1995). Monte carlo studies of x-ray energy absorption and quantum noise in megavoltage transmission radiography, *Med. Phys.* **22**: 1077–88.

Jin, J.-Y., Yin, F.-F., Tenn, S. E., Medin, P. M. & Solberg, T. D. (2008). Use of the BrainLAB ExacTrac x-ray 6d system in image-guided radiotherapy, *Med. Dosim.* **33**(2): 124–134.

Johns, H. & Cunningham, J. (1983). *The Physics of Radiology*, fourth edn, Thomas.

Kak, A. & Slaney, M. (1988). *Principles of Computerized Tomographic Imaging*, IEEE Press.

Kamino, Y., Takayama, K., Kokubo, M., Narita, Y., Hirai, E., Kawawda, N., Mizowaki, T., Nagata, Y., Nishidai, T. & Hiraoka, M. (2006). Development of a four-dimensional image-guided radiotherapy system with a gimbaled x-ray head, *Int. J. Radiat. Oncol. Biol. Phys.* **66**(1): 271–278.

Karzmark, C. & Morton, R. J. (1989). *A primer on theory and operation of linear accelerators in radiation therapy*, Medical Physics Publishing Corporation.

Kasap, S. O. & Rowlands, J. A. (2002). Direct-conversion flat-panel x-ray image sensors for digital radiography, *Proc. IEEE* **90**(4): 591–604.

Keall, P. J., Mageras, G. S., Balter, J. M., Emery, R. S., Forster, K. M., Jiang, S. B., Kapatoes, J. M., Low, D. A., Murphy, M. J., Murray, B. R. et al. (2006). The management of respiratory motion in radiation oncology report of AAPM task group 76, *Med. Phys.* **33**: 3874–3900.

Keall, P., Joshi, S., Vedam, S., Siebers, J., Kini, V. & Mohan, R. (2005). Four-dimensional radiotherapy planning for DMLC-based respiratory motion tracking, *Med. Phys.* **32**: 942–951.

Keall, P., Kini, V., Vedam, S. & Mohan, R. (2001). Motion adaptive x-ray therapy: a feasibility study, *Phys. Med. Biol.* **46**(1): 1–10.

Keall, P., Sawant, A., Cho, B., Ruan, D., Wu, J., Poulsen, P., Petersen, J., Newell, L., Cattell, H. & Korreman, S. (2011). Electromagnetic-guided dynamic multileaf collimator tracking enables motion management for intensity-modulated arc therapy, *Int. J. Radiat. Oncol. Biol. Phys.* **79**(1): 312–320.

Kilby, W., Dooley, J., Kuduvalli, G., Sayeh, S. & Maurer Jr, C. (2010). The CyberKnife robotic radiosurgery system in 2010, *Technol. Cancer Res. Treat.* **9**(5): 433–452.

Kincaid, Jr., R. E., Yorke, E. D., Goodman, K. A., Rimner, A., Wu, A. J. & Mageras, G. S. (2013). Investigation of gated cone-beam CT to reduce respiratory motion blurring, *Med. Phys.* **40**(4): 041717.

Kirkby, C. & Sloboda, R. (2005). Comprehensive monte carlo calculation of the point spread function for a commercial a-Si EPID, *Med. Phys.* **32**: 1115–1127.

Kirvan, P. F., Monajemi, T. T., Fallone, B. G. & Rathee, S. (2010). Performance characterization of a MVCT scanner using multislice thick, segmented cadmium tungstate-photodiode detectors, *Med. Phys.* **37**(1): 249–257.

Korreman, S., Juhler-Nøttrup, T. & Boyer, A. (2008). Respiratory gated beam delivery cannot facilitate margin reduction, unless combined with respiratory correlated image guidance, *Radiother. Oncol.* **86**: 61–68.

Kotte, A. N., Hofman, P., Lagendijk, J. J., van Vulpen, M. & van der Heide, U. A. (2007). Intrafraction motion of the prostate during external-beam radiation therapy: Analysis of 427 patients with implanted fiducial markers, *Int. J. Radiat. Oncol. Biol. Phys.* **69**(2): 419–425.

Krauss, A., Fast, M., Nill, S. & Oelfke, U. (2012). Multileaf collimator tracking integrated with a novel x-ray imaging system and external surrogate monitoring, *Phys. Med. Biol.* **57**(8): 2425–2439.

Krauss, A., Nill, S. & Oelfke, U. (2011). The comparative performance of four respiratory motion predictors for real-time tumour tracking, *Phys. Med. Biol.* **56**(16): 5303–5317.

Krauss, A., Nill, S., Tacke, M. & Oelfke, U. (2011 b). Electromagnetic real-time tumor position monitoring and dynamic multileaf collimator tracking using a Siemens 160 MLC: Geometric and dosimetric accuracy of an integrated system, *Int. J. Radiat. Oncol. Biol. Phys.* **79**(2): 579–587.

Kubo, H. D. & Hill, B. C. (1996). Respiration gated radiotherapy treatment: a technical study, *Phys. Med. Biol.* **41**(1): 83–91.

Kubo, H. D., Len, P. M., Minohara, S.-i. & Mostafavi, H. (2000). Breathing-synchronized radiotherapy program at the University of California Davis Cancer Center, *Med. Phys.* **27**: 346–353.

Lagendijk, J. J., Raaymakers, B. W., Raaijmakers, A. J., Overweg, J., Brown, K. J., Kerkhof, E. M., Put, R. W., Hardemark, B., Vulpen, M. v. & Heide, U. A. (2008). Mri/linac integration, *Radiother. Oncol.* **86**(1): 25–29.

Leng, S., Zambelli, J., Tolakanahalli, R., Nett, B., Munro, P., Star-Lack, J., Paliwal, B. & Chen, G.-H. (2008). Streaking artifacts reduction in four-dimensional cone-beam computed tomography, *Med. Phys.* **35**(10): 4649–4659.

Li, R., Fahimian, B. P. & Xing, L. (2011). A bayesian approach to real-time 3d tumor localization via monoscopic x-ray imaging during treatment delivery, *Med. Phys.* **38**(7): 4205–4214.

Li, X. A., Stepaniak, C. & Gore, E. (2006). Technical and dosimetric aspects of respiratory gating using a pressure-sensor motion monitoring system, *Med. Phys.* **33**: 145–154.

Liaparinos, P. & Kandarakis, I. (2011). Overestimations in zero frequency DQE of x-ray imaging converters assessed by monte carlo techniques based on the study of energy impartation events, *Med. Phys.* **38**: 4440–50.

Liaparinos, P., Kandarakis, I., Cavouras, D., Delis, H. & Panayiotakis, G. (2006). Modeling granular phosphor screens by monte carlo methods, *Med. Phys.* **33**: 4502–4514.

Liaparinos, P., Kandarakis, I., Cavouras, D., Nikolopoulos, D., Valais, I. & Panayiotakis, G. (2004). Simulating the emission efficiency and resolution properties of fluorescent screens by monte carlo methods, *IEEE Nucl. Sci. Conf. R.*, Vol. 2, IEEE, pp. 874–78.

Lu, J., Guerrero, T., Munro, P., Jeung, A., Chi, P., Balter, P., Zhu, X., Mohan, R. & Pan, T. (2007). Four-dimensional cone beam CT with adaptive gantry rotation and adaptive data sampling, *Med. Phys.* **34**: 3520–3529.

Lu, W., Nystrom, M., Parikh, P., Fooshee, D., Hubenschmidt, J., Bradley, J. & Low, D. (2006). A semi-automatic method for peak and valley detection in free-breathing respiratory waveforms, *Med. Phys.* **33**: 3634–3636.

Lujan, A., Larsen, E., Balter, J. & Ten Haken, R. (1999). A method for incorporating organ motion due to breathing into 3d dose calculations, *Med. Phys.* **26**: 715–720.

Mail, N., Moseley, D. J., Siewerdsen, J. H. & Jaffray, D. A. (2008). An empirical method for lag correction in cone-beam CT, *Med. Phys.* **35**(11): 5187–5196.

Maltz, J., Gangadharan, B., Bose, S., Hristov, D., Faddegon, B., Paidi, A. & Bani-Hashemi, A. (2008). Algorithm for x-ray scatter, beam-hardening, and beam profile correction in diagnostic (kilovoltage) and treatment (megavoltage) cone beam CT, *IEEE Trans. Med. Imaging* **27**(12): 1791–1810.

Maltz, J., Hartmann, J., Dubouloz, A., Paidi, A., Gangadharan, B., Hoerauf, G. & Bani-Hashemi, A. (2009 b). Th-d-210a-03: Thick monolithic pixelated scintillator array for megavoltage imaging, *Med. Phys.* **36**(6): 2818–2819.

Maltz, J. S., Sprenger, F., Fuerst, J., Paidi, A., Fadler, F. & Bani-Hashemi, A. R. (2009). Fixed gantry tomosynthesis system for radiation therapy image guidance based on a multiple source x-ray tube with carbon nanotube cathodes, *Med. Phys.* **36**(5): 1624–1636.

Maurer, J., Godfrey, D. & Wu, Q. (2011). Mo-d-brc-07: Reducing artifacts in cone-beam CT images caused by the presence of an array used for tracking transponders during radiotherapy, *Med. Phys.* **38**: 3713.

McQuaid, D. & Webb, S. (2006). IMRT delivery to a moving target by dynamic MLC tracking: delivery for targets moving in two dimensions in the beam's eye view, *Phys. Med. Biol.* **51**(19): 4819–4839.

Menten, M. J., Guckenberger, M., Herrmann, C., Krauß, A., Nill, S., Oelfke, U., Wilbert, J. r. et al. (2012). Comparison of a multileaf collimator tracking system and a robotic treatment couch tracking system for organ motion compensation during radiotherapy, *Med. Phys.* **39**(11): 7032–7041.

Mijnheer, B. (2008). State of the art of in vivo dosimetry, *Radiat. Prot. Dosim.* **131**(1): 117–122.

Moorrees, J. & Bezak, E. (2012). Four dimensional CT imaging: a review of current technologies and modalities, *Australas. Phys. Eng. Sci. Med.* **35**: 1–15.

Mooslechner, M., Mitterlechner, B., Weichenberger, H., Huber, S., Sedlmayer, F. & Deutschmann, H. (2013). Analysis of a free-running synchronization artifact correction for MV-imaging with aSi:H flat panels, *Med. Phys.* **40**: 031906.

Murphy, M. J., Balter, J., Balter, S., BenComo Jr, J. A., Das, I. J., Jiang, S. B., Ma, C.-M., Olivera, G. H., Rodebaugh, R. F., Ruchala, K. J. et al. (2007). The management of imaging dose during image-guided radiotherapy: Report of the AAPM task group 75, *Med. Phys.* **34**: 4041–4063.

Navab, N., Bani-Hashemi, A. R., Mitschke, M. M., Holdsworth, D. W., Fahrig, R., Fox, A. J. & Graumann, R. (1996). Dynamic geometrical calibration for 3d cerebral angiography, *Medical Imaging 1996*, International Society for Optics and Photonics, pp. 361–370.

Nelms, D. W., Shukla, H. I., Nixon, E., Bayouth, J. E. & Flynn, R. T. (2009). Assessment of three dead detector correction methods for cone-beam computed tomography, *Med. Phys.* **36**: 4569–4576.

Nijsten, S., Minken, A., Lambin, P. & Bruinvis, I. (2004). Verification of treatment parameter transfer by means of electronic portal dosimetry, *Med. Phys.* **31**: 341–347.

Nill, S., Unkelbach, J., Dietrich, L. & Oelfke, U. (2005). Online correction for respiratory motion: evaluation of two different imaging geometries, *Phys. Med. Biol.* **50**: 4087–4096.

O'Brien, R. T., Cooper, B. J. & Keall, P. J. (2013). Optimizing 4d cone beam computed tomography acquisition by varying the gantry velocity and projection time interval, *Phys. Med. Biol.* **58**(6): 1705–1723.

Oelfke, U., Tücking, T., Nill, S., Seeber, A., Hesse, B., Huber, P. & Thilmann, C. (2006). Linac-integrated kV-cone beam CT: technical features and first applications, *Med. Dosim.* **31**(1): 62–70.

Overdick, M., Baumer, C., Engel, K., Fink, J., Herrmann, C., Kruger, H., Simon, M., Steadman, R. & Zeitler, G. (2009). Status of direct conversion detectors for medical imaging with x-rays, *IEEE Trans. Nucl. Sci.* **56**(4): 1800–1809.

Pang, G., Bani-Hashemi, A., Au, P., O'Brien, P., Rowlands, J., Morton, G., Lim, T., Cheung, P. & Loblaw, A. (2008). Megavoltage cone beam digital tomosynthesis (MV-CBDT) for image-guided radiotherapy: a clinical investigational system, *Phys. Med. Biol.* **53**(4): 999–1013.

Parent, L., Seco, J., Evans, P., Fielding, A. & Dance, D. (2006). Monte carlo modelling of a-Si EPID response: The effect of spectral variations with field size and position, *Med. Phys.* **33**: 4527–4450.

Park, S.-J., Ionascu, D., Hacker, F., Mamon, H. & Berbeco, R. (2009). Automatic marker detection and 3d position reconstruction using cine EPID images for SBRT verification, *Med. Phys.* **36**(10): 4536–4546.

Partridge, M., Ebert, M. & Hesse, B. (2002). IMRT verification by three-dimensional dose reconstruction from portal beam measurements, *Med. Phys.* **29**: 1847–1858.

Pasma, K., Kroonwijk, M., De Boer, J., Visser, A. & Heijmen, B. (1998). Accurate portal dose measurement with a fluoroscopic electronic portal imaging device (EPID) for open and wedged beams and dynamic multileaf collimation, *Phys. Med. Biol.* **43**(8): 2047–2060.

Peeters, A., Grutters, J. P., Pijls-Johannesma, M., Reimoser, S., De Ruysscher, D., Severens, J. L., Joore, M. A. & Lambin, P. (2010). How costly is particle therapy? cost analysis of external beam radiotherapy with carbon-ions, protons and photons, *Radiother. Oncol.* **95**(1): 45–53.

Pistrui-Maximean, S., Freud, N., Létang, J., Koch, A., Munier, B., Walenta, A., Montarou, G. & Babot, D. (2006). Geant4 simulation of the response of phosphor screens for x-ray imaging, *Nucl. Instrum. Meth. A* **563**: 196–199.

Podgorsak, E. B. et al. (2005). *Radiation oncology physics*, Citeseer.

Poludniowski, G., Webb, S. & Evans, P. (2012). Technical note: Suppression of artifacts arising from simultaneous cone-beam imaging and RF transponder tracking in prostate radiotherapy, *Med. Phys.* **39**: 1646–1649.

Poppe, B., Thieke, C., Beyer, D., Kollhoff, R., Djouguela, A., Rühmann, A., Willborn, K. & Harder, D. (2006). DAVID–a translucent multi-wire transmission ionization chamber for in vivo verification of IMRT and conformal irradiation techniques, *Phys. Med. Biol.* **51**: 1237–1248.

Poruba, A., Springer, J., Mullerova, L., Beitlerova, A., Vaněček, M., Wyrsch, N. & Shah, A. (2004). Temperature dependence of the optical absorption coefficient of microcrystalline silicon, *J. Non-Cryst. Solids* **338**: 222–227.

Pouliot, J., Bani-Hashemi, A., Chen, J., Svatos, M., Ghelmansarai, F., Mitschke, M., Aubin, M., Xia, P., Morin, O., Bucci, K. et al. (2005). Low-dose megavoltage cone-beam CT for radiation therapy, *Int. J. Radiat. Oncol. Biol. Phys.* **61**(2): 552–560.

Poulsen, P., Carl, J., Nielsen, J., Nielsen, M., Thomsen, J., Jensen, H., Kjærgaard, B., Zepernick, P., Worm, E., Fledelius, W. et al. (2012). Megavoltage image-based dynamic multileaf collimator tracking of a NiTi stent in porcine lungs on a linear accelerator, *Int. J. Radiat. Oncol. Biol. Phys.* **82**: 321–327.

Poulsen, P., Cho, B., Sawant, A. & Keall, P. (2010 b). Implementation of a new method for dynamic multileaf collimator tracking of prostate motion in arc radiotherapy using a single kV imager, *Int. J. Radiat. Oncol. Biol. Phys.* **76**: 914–923.

Poulsen, P. R., Cho, B., Langen, K., Kupelian, P. & Keall, P. J. (2008). Three-dimensional prostate position estimation with a single x-ray imager utilizing the spatial probability density, *Phys. Med. Biol.* **53**(16): 4331–4353.

Poulsen, P. R., Cho, B., Ruan, D., Sawant, A. & Keall, P. J. (2010). Dynamic multileaf collimator tracking of respiratory target motion based on a single kilovoltage imager during arc radiotherapy, *Int. J. Radiat. Oncol. Biol. Phys.* **77**(2): 600–607.

Poulsen, P. R., Cho, B., Sawant, A., Ruan, D. & Keall, P. J. (2010 c). Detailed analysis of latencies in image-based dynamic MLC tracking, *Med. Phys.* **37**(9): 4998–5005.

Poulsen, P. R., Cho, B., Sawant, A., Ruan, D. & Keall, P. J. (2010 d). Dynamic MLC tracking of moving targets with a single kV imager for 3d conformal and IMRT treatments, *Acta Oncol.* **49**(7): 1092–1100.

Radcliffe, T., Barnea, G., Wowk, B., Rajapakshe, R. & Shalev, S. (1993). Monte carlo optimization of metal/phosphor screens at megavoltage energies, *Med. Phys.* **20**: 1161–1169.

Rau, A., Nill, S., Eidens, R. & Oelfke, U. (2008). Synchronized tumour tracking with electromagnetic transponders and kV x-ray imaging: evaluation based on a thorax phantom, *Phys. Med. Biol.* **53**(14): 3789–3805.

Robar, J. L., Connell, T., Huang, W. & Kelly, R. G. (2009). Megavoltage planar and cone-beam imaging with low-Z targets: Dependence of image quality improvement on beam energy and patient separation, *Med. Phys.* **36**(9): 3955–3963.

Roberts, D., Hansen, V., Thompson, M., Poludniowski, G., Niven, A., Seco, J. & Evans, P. (2012). Kilovoltage energy imaging with a radiotherapy linac with a continuously variable energy range, *Med. Phys.* **39**: 1218–1226.

Rottmann, J., Aristophanous, M., Chen, A., Berbeco, R. et al. (2010). A multi-region algorithm for markerless beam's-eye view lung tumor tracking, *Phys. Med. Biol.* **55**: 5585–5598.

Rowlands, J. (2002). The physics of computed radiography, *Phys. Med. Biol.* **47**: R123–R166.

Sawant, A., Venkat, R., Srivastava, V., Carlson, D., Povzner, S., Cattell, H. & Keall, P. (2008). Management of three-dimensional intrafraction motion through real-time DMLC tracking, *Med. Phys.* **35**: 2050–2061.

Sawkey, D., Lu, M., Morin, O., Aubin, M., Yom, S., Gottschalk, A., Bani-Hashemi, A. & Faddegon, B. (2010). A diamond target for megavoltage cone-beam CT, *Med. Phys.* **37**: 1246–1253.

Schach von Wittenau, A., Logan, C., Aufderheide III, M. & Slone, D. (2002). Blurring artifacts in megavoltage radiography with a flat-panel imaging system: Comparison of monte carlo simulations with measurements, *Med. Phys.* **29**: 2559–2570.

Schweikard, A., Shiomi, H. & Adler, J. (2004). Respiration tracking in radiosurgery, *Med. Phys.* **31**: 2738–2741.

Seppenwoolde, Y., Shirato, H., Kitamura, K., Shimizu, S., van Herk, M., Lebesque, J. & Miyasaka, K. (2002). Precise and real-time measurement of 3d tumor motion in lung due to breathing and heartbeat, measured during radiotherapy, *Int. J. Radiat. Oncol. Biol. Phys.* **53**(4): 822–834.

Shah, A. P., Kupelian, P. A., Willoughby, T. R. & Meeks, S. L. (2011). Expanding the use of real-time electromagnetic tracking in radiation oncology, *J. Appl. Clin. Med. Phys.* **12**(4): 34–49.

Shikhaliev, P. M. (2008). Computed tomography with energy-resolved detection: a feasibility study, *Phys. Med. Biol.* **53**(5): 1475–1495.

Shirato, H., Oita, M., Fujita, K., Watanabe, Y. & Miyasaka, K. (2004). Feasibility of synchronization of real-time tumor-tracking radiotherapy and intensity-modulated radiotherapy from viewpoint of excessive dose from fluoroscopy, *Int. J. Radiat. Oncol. Biol. Phys.* **60**(1): 335–341.

Shirato, H., Shimizu, S., Kitamura, K., Nishioka, T., Kagei, K., Hashimoto, S., Aoyama, H., Kunieda, T., Shinohara, N., Dosaka-Akita, H. et al. (2000). Four-dimensional treatment planning and fluoroscopic real-time tumor tracking radiotherapy for moving tumor, *Int. J. Radiat. Oncol. Biol. Phys.* **48**(2): 435–442.

Siewerdsen, J. & Jaffray, D. (1999). A ghost story: spatio-temporal response characteristics of an indirect-detection flat-panel imager, *Med. Phys.* **26**: 1624–1641.

Smith, R. L., Sawant, A., Santanam, L., Venkat, R. B., Newell, L. J., Cho, B.-c., Poulsen, P., Catell, H., Keall, P. J. & Parikh, P. J. (2009). Integration of real-time internal electromagnetic position monitoring coupled with dynamic multileaf collimator tracking: An intensity-modulated radiation therapy feasibility study, *Int. J. Radiat. Oncol. Biol. Phys.* **74**(3): 868–875.

Sonke, J., Zijp, L., Remeijer, P. & van Herk, M. (2005). Respiratory correlated cone beam CT, *Med. Phys.* **32**: 1176–1186.

Steinke, M. F. (2010). *Performance characteristics of a novel megavoltage cone beam computed tomography device*, Master's thesis, University of Heidelberg, Germany.

Suh, Y., Dieterich, S. & Keall, P. J. (2007). Geometric uncertainty of 2d projection imaging in monitoring 3d tumor motion, *Phys. Med. Biol.* **52**(12): 3439–3454.

Swank, R. (1973). Absorption and noise in x-ray phosphors, *J. Appl. Phys.* **44**: 4199–4203.

Sweeney, R. A., Seubert, B., Stark, S., Homann, V., Müller, G., Flentje, M. & Guckenberger, M. (2012). Accuracy and inter-observer variability of 3d versus 4d cone-beam CT based image-guidance in SBRT for lung tumors, *Radiat. Oncol.* **7**(1): 81.

Tacke, M. B., Nill, S., Krauss, A. & Oelfke, U. (2010). Real-time tumor tracking: automatic compensation of target motion using the Siemens 160 MLC, *Med. Phys.* **37**: 753–761.

Tacke, M., Nill, S. & Oelfke, U. (2007). Real-time tracking of tumor motions and deformations along the leaf travel direction with the aid of a synchronized dynamic MLC leaf sequencer, *Phys. Med. Biol.* **52**(22): N505–N512.

Tacke, M., Szymanowski, H., Oelfke, U., Schulze, C., Nuss, S., Wehrwein, E. & Leidenberger, S. (2006). Assessment of a new multileaf collimator concept using GEANT4 monte carlo simulations, *Med. Phys.* **33**: 1125–1132.

Takayama, K., Mizowaki, T., Kokubo, M., Kawada, N., Nakayama, H., Narita, Y., Nagano, K., Kamino, Y. & Hiraoka, M. (2009). Initial validations for pursuing irradiation using a gimbals tracking system, *Radiother. Oncol.* **93**(1): 45–49.

Teymurazyan, A. & Pang, G. (2013). An inherent anti-scatter detector for megavoltage x-ray imaging, *Phys. Med. Biol.* **58**(5): 1479–1493.

Tsechanski, A., Bielajew, A. F., Faermann, S. & Krutman, Y. (1998). A thin target approach for portal imaging in medical accelerators, *Phys. Med. Biol.* **43**(8): 2221–2236.

van der Wielen, G. J., Mutanga, T. F., Incrocci, L., Kirkels, W. J., Osorio, E. M. V., Hoogeman, M. S., Heijmen, B. J. & de Boer, H. C. (2008). Deformation of prostate and seminal vesicles relative to intraprostatic fiducial markers, *Int. J. Radiat. Oncol. Biol. Phys.* **72**(5): 1604–1611.

van Herk, M. (2004). Errors and margins in radiotherapy, *Sem. Radiat. Oncol.*, Vol. 14, Elsevier, pp. 52–64.

van Herk, M., Ploeger, L. & Sonke, J.-J. (2011). A novel method for megavoltage scatter correction in cone-beam CT acquired concurrent with rotational irradiation, *Radiother. Oncol.* **100**(3): 365–369.

van Herk, M., Remeijer, P., Rasch, C., Lebesque, J. V. et al. (2000). The probability of correct target dosage: dose-population histograms for deriving treatment margins in radiotherapy., *Int. J. Radiat. Oncol. Biol. Phys.* **47**(4): 1121–1135.

van Herk, M., Zijp, L., Remeijer, P., Wolthaus, J. & Sonke, J. (2007). On-line 4d cone beam CT for daily correction of lung tumour position during hypofractionated radiotherapy, *Int. Conf. on the Use of Computers in Radiation Therapy*, ICCR, pp. 6241–6245.

Vedam, S., Keall, P., Docef, A., Todor, D., Kini, V. & Mohan, R. (2004). Predicting respiratory motion for four-dimensional radiotherapy, *Med. Phys.* **31**: 2274–2283.

Verellen, D., De Ridder, M., Linthout, N., Tournel, K., Soete, G. & Storme, G. (2007). Innovations in image-guided radiotherapy, *Nat. Rev. Cancer* **7**(12): 949–960.

Vinci, J. P., Hogstrom, K. R. & Neck, D. W. (2008). Accuracy of cranial coplanar beam therapy using an oblique, stereoscopic x-ray image guidance system, *Med. Phys.* **35**: 3809–3819.

Wang, Q., Li, L., Zhang, L., Chen, Z. & Kang, K. (2013). A novel metal artifact reducing method for cone-beam CT based on three approximately orthogonal projections, *Phys. Med. Biol.* **58**(1): 1–17.

Wendling, M., Louwe, R. J., McDermott, L. N., Sonke, J.-J., van Herk, M. & Mijnheer, B. J. (2006). Accurate two-dimensional IMRT verification using a back-projection EPID dosimetry method, *Med. Phys.* **33**: 259–273.

Wendling, M., McDermott, L. N., Mans, A., Sonke, J.-J., van Herk, M. & Mijnheer, B. J. (2009). A simple backprojection algorithm for 3d in vivo EPID dosimetry of IMRT treatments, *Med. Phys.* **36**: 3310–3321.

Wiersma, R., Mao, W. & Xing, L. (2008). Combined kV and MV imaging for real-time tracking of implanted fiducial markers, *Med. Phys.* **35**(4): 1191–1198.

Wiesent, K., Barth, K., Navab, N., Durlak, P., Brunner, T., Schuetz, O. & Seissler, W. (2000). Enhanced 3-d-reconstruction algorithm for C-arm systems suitable for interventional procedures, *IEEE Trans. Med. Imag.* **19**(5): 391–403.

Wilbert, J., Meyer, J., Baier, K., Guckenberger, M., Herrmann, C., Heß, R., Janka, C., Ma, L., Mersebach, T., Richter, A. et al. (2008). Tumor tracking and motion compensation with an adaptive tumor tracking system (ATTS): system description and prototype testing, *Med. Phys.* **35**: 3911–3921.

XCOM (2013). `http://physics.nist.gov/PhysRefData/Xcom/html/xcom1.html`. Accessed: 2013-04-03.

Xiong, Z., Feng, S., McGary, J. E. & Chen, J. (2012). Magnetic tracking inside conducting bores for radiotherapy tumor localization systems, *IEEE Trans. Magn.* **48**(2): 395–398.

Yan, D., Vicini, F., Wong, J. & Martinez, A. (1997). Adaptive radiation therapy, *Phys. Med. Biol.* **42**(1): 123–132.

Yan, H., Li, H., Liu, Z., Nath, R. & Liu, W. (2012). Hybrid MV-kV 3d respiratory motion tracking during radiation therapy with low imaging dose, *Phys. Med. Biol.* **57**(24): 8455–8469.

Yan, H., Wang, X., Yin, W., Pan, T., Ahmad, M., Mou, X., Cervino, L., Jia, X. & Jiang, S. B. (2013). Extracting respiratory signals from thoracic cone beam CT projections, *Phys. Med. Biol.* **58**(5): 1447–1464.

Yang, J., Li, J., Qin, L., Xiong, W. & Ma, C. (2004). Modelling of electron contamination in clinical photon beams for monte carlo dose calculation, *Phys. Med. Biol.* **49**: 2657–2673.

Yoriyaz, H., Moralles, M., Siqueira, P., da Costa Guimarães, C., Cintra, F. & Dos Santos, A. (2009). Physical models, cross sections, and numerical approximations used in MCNP and Geant4 monte carlo codes for photon and electron absorbed fraction calculation, *Med. Phys.* **36**: 5198–5213.

Zheng, Z., Sun, M., Pavkovich, J. & Star-Lack, J. (2011). Fast 4d cone-beam reconstruction using the McKinnon-Bates algorithm with truncation correction and nonlinear filtering, *Proc. SPIE*, Vol. 7961, p. 79612U.

Zhu, X., Bourland, J., Yuan, Y., Zhuang, T., O'Daniel, J., Thongphiew, D., Wu, Q., Das, S., Yoo, S. & Yin, F. (2009). Tradeoffs of integrating real-time tracking into IGRT for prostate cancer treatment, *Phys. Med. Biol.* **54**(17): N393–N401.

Zijp, L., Sonke, J. J. & von Herk, M. (2004). Extraction of the respiratory signal from sequential thorax cone-beam x-ray images, *Int. Conf. on the Use of Computers in Radiation Therapy*, ICCR, pp. 507–509.

Acknowledgements

I would like to express my gratitude to the following people:

- Uwe Oelfke: for being a fair and humorous thesis advisor
- Wolfgang Schlegel: for acting as second referee of this thesis
- Simeon Nill: for providing excellent day-to-day supervision and help
- John Rowlands & Geordi Pang: for taking me under their wing during my research stay in Canada
- Aram Teymurazyan: for teaching me about Monte Carlo simulations and being great fun to work with
- Peter Bachert & Burkhard Groh: for faithfully serving on my TAC committee
- Eric Wisotzky: for the great work on our joint projects
- Thomas König: for helpful discussions and providing his LaTeX template
- Ion Stroescu & Arthur Guinness: they know why
- and most importantly my wife Karin